UNIVERSIDADE ESTADUAL DE CAMPINAS

INSTITUTO DE QUÍMICA

LAURA CAETANO ESCOBAR DA SILVA

MORPHOLOGY OF HYBRID NANOCOMPOSITES BASED ON BICOMPONENT MATRICES MADE UP OF POLYCAPROLACTONE AND POLY(ETHYLENE GLYCOL)

MORFOLOGIA DE NANOCOMPÓSITOS HÍBRIDOS COM MATRIZES BICOMPONENTES DE POLICAPROLACTONA E POLI(ETILENO GLICOL)

CAMPINAS
2018

LAURA CAETANO ESCOBAR DA SILVA

MORPHOLOGY OF HYBRID NANOCOMPOSITES BASED ON BICOMPONENT MATRICES MADE UP OF POLYCAPROLACTONE AND POLY(ETHYLENE GLYCOL)

MORFOLOGIA DE NANOCOMPÓSITOS HÍBRIDOS COM MATRIZES BICOMPONENTES DE POLICAPROLACTONA E POLI(ETILENO GLICOL)

Tese de Doutorado apresentada ao Instituto de Química da Universidade Estadual de Campinas como parte dos requisitos exigidos para a obtenção do título de Doutora em Ciências

Doctor´s Thesis presented to the Institute of Chemistry of the University of Campinas as part of the requirements to obtain the title of Doctor in Sciences.

Supervisor: Prof. Dr. Maria do Carmo Gonçalves

-

ESTE EXEMPLAR CORRESPONDE À VERSÃO FINAL DA TESE DEFENDIDA PELA ALUNA LAURA CAETANO ESCOBAR DA SILVA, E ORIENTADA PELA PROFA. DRA. MARIA DO CARMO GONÇALVES

CAMPINAS

2018

Agência(s) de fomento e nº(s) de processo(s): CNPq, 140469/2014-1
ORCID: https://orcid.org/0000-0002-9191-3440

Ficha catalográfica
Universidade Estadual de Campinas
Biblioteca do Instituto de Química
Camila Barleta Fullin - CRB 8462

Si38m

Silva, Laura Caetano Escobar da, 1987-
Morphology of hybrid nanocomposites based on bicomponent matrices made up of polycaprolactone and poly(ethylene glycol) / Laura Caetano Escobar da Silva. – Campinas, SP : [s.n.], 2018.

Orientador: Maria do Carmo Gonçalves.
Tese (doutorado) – Universidade Estadual de Campinas, Instituto de Química.

1. Polissilsesquioxanos. 2. Híbridos orgânicos-inorgânicos. 3. Microscopia eletrônica de transmissão. 4. Raios X - Espalhamento a baixo ângulo. 5. Biomateriais. I. Gonçalves, Maria do Carmo, 1957-. II. Universidade Estadual de Campinas. Instituto de Química. III. Título.

1. Informações para Biblioteca Digital

Título em outro idioma: Morfologia de nanocompósitos híbridos com matrizes bicomponentes de policaprolactona e poli(etileno glicol)
Palavras-chave em inglês:
Polysilsesquioxanes
Organic-inorganic hydrids
Transmission electron microscopy
SAXS (Small angle X-ray scattering)
Biomaterials
Área de concentração: Físico-Química **Titulação:** Doutora em Ciências
Banca examinadora:
Maria do Carmo Gonçalves [Orientador]
Danilo Justino Carastan
Eduardo Radovanovic
Camilla Abbehausen
Edvaldo Sabadini
Data de defesa: 26-04-2018
Programa de Pós-Graduação: Química

BANCA EXAMINADORA

Profa. Dra. Maria do Carmos Gonçalves (Orientadora)

Prof. Dr. Eduardo Radovanovic (DQ-UEM)

Prof. Dr. Danilo Justino Carastan (UFABC-Santo André)

Prof. Dr. Edvaldo Sabadini (IQ-UNICAMP)

Profa. Dra. Camilla Abbehausen (IQ-UNICAMP)

A Ata da defesa com as respectivas assinaturas dos membros encontra-se no processo de vida acadêmica do(a) aluno(a).

Este exemplar corresponde à redação final da Tese de Doutorado defendida pelo(a) aluno(a) **LAURA CAETANO ESCOBAR DA SILVA,** aprovada pela Comissão Julgadora em 26 de abril de 2018.

Aos meus avós, Antônio, Astrogildo, Dejanira e Marina, que não tiveram tempo de ver a conclusão deste trabalho.

"CADA DIA É UMA CHANCE

PRA SER MELHOR QUE ONTEM,

....

CLAREZA NA IDEIA,

PUREZA NO CORAÇÃO,

SENTIMENTOS COMO GUIA

E HONESTIDADE COMO RELIGIÃO"

CADA VENTO - EMICIDA E RAEL DA RIMA

AGRADECIMENTOS

Desde o início da minha carreira enquanto pesquisadora, tenho o enorme privilégio de ser orientada pela Prof. Dra. Maria do Carmo Gonçalves. A ela sou grata por todas as oportunidades que tive até aqui. Carminha, muito obrigada por acreditar no meu potencial, por confiar no meu trabalho, por sempre me incentivar, por todos os conselhos e por todos esses anos de convivência e amizade.

Ao Dr. Tomás S. Plivelic, o melhor "desorientador" que eu poderia pedir, também tenho inúmeros motivos para agradecer. Obrigada por estar sempre presente, animado e disposto a ensinar. Obrigada pelas infinitas horas de discussão pelo Skype e outras tantas horas de discussão antes, durante e depois dos tempos de feixe. Principalmente, muito obrigada pela oportunidade de conhecer e vivenciar o MAX IV e a Suécia.

Aos professores: Celso Aparecido Bertran, Maria Isabel Felisberti, Marcelo Ganzarolli de Oliveira, Edvaldo Sabadini, Heloise Oliveira Pastore e tantos outros, agradeço por estarem sempre dispostos a auxiliar, oferecendo seus laboratórios e equipamentos, participando das minhas bancas ou compartilhando suas experiências.

Aos técnicos: Fabiana Amorim, Hugo Loureiro, Douglas Soares da Silva e tantos outros, agradeço pelas horas dedicadas à caracterização cuidadosa dos meus materiais e à discussão dos meus resultados. Agradeço também por dividir comigo o seu conhecimento.

Aos excelentes profissionais do LNNano: Rodrigo Portugal, Alexandre Cassago, Jefferson Bettini, Carlos Ospina e Marcelo Alexandre de Farias agradeço enormemente por participarem ativamente da minha formação enquanto microscopista.

Aos colegas do laboratório I-114 que, depois de tantos anos, já são muitos para serem citados nominalmente, agradeço por compartilharem das horas boas e ruins. Obrigada pelas risadas, pelas discussões, pelos almoços, cafés, bares e festas. Em especial, agradeço à Liliane Battirola, Lívia Mesquita, Thiago Rufino e Luiz Guilherme que sempre acompanharam de perto (mesmo que não geograficamente) os percalços desse meu doutorado.

Ao professor Cristiano Giacomelli e aos seus alunos Tanize Bortolotto, Augusto Freitas e Suelen Trindade, agradeço por me receberem com tanta atenção e por compartilharem comigo toda a sua experiência. O tempo que passei na UFSM foi muito enriquecedor.

Ao Instituto de Química da UNICAMP, ao Laboratório MAX IV (Lund-Suécia), ao European Synchrotron Radiation Facility (ESRF-França) e aos Laboratórios Nacionais de Nanotecnologia (LNNano-CNPEM) e de Luz Síncrotron (LNLS-CNPEM) agradeço por disponibilizarem toda a infraestrutura necessária para o desenvolvimento deste trabalho.

Ao CNPq (processo: 140469/2014-1) agradeço pela bolsa de doutorado, À FAPESP (processos: 2010/17804-7; 2016/02414-5 e 2017/50274-0) e ao Instituto Nacional de Materiais Complexos e Funcionais (INCT-INOMAT) agradeço pelo apoio financeiro.

São tantos os envolvidos neste trabalho que acaba por me faltar espaço para agradecer a todos os meus amigos e familiares da forma como merecem. Logo, procuro ser breve:

Agradeço aos meus tantos e tão queridos amigos não só pelas presenças, mas, principalmente, por compreenderem as minhas ausências. Desculpem-me por não citar um a um. Em especial, agradeço à Priscilla Marques e à Flávia Estrada pelos encontros, sempre cheios de afeto e escuta.

Agradeço à Késia Anastácio pelos anos de convivência, por toda a paciência e apoio ao longo dessa jornada que trilhamos em paralelo.

Agradeço à toda a minha amada família: tios, tias, primos e primas, de sangue e de vida, por todo o carinho, apoio e incentivo.

Finalmente, agradeço aos meus pais, Lúcia e Aristeu e à minha irmã Luisa por me motivarem a perseguir meus sonhos e a continuar nessa carreira, apesar de todas as adversidades. Obrigada pelo apoio incansável e pelo amor incondicional de vocês, que mesmo quando estive ausente, sempre pude sentir de perto.

RESUMO

Nanocompósitos híbridos orgânico-inorgânicos (O-I) constituídos de policaprolactona (PCL) e poli(etileno glicol) (PEG), reticulados por estruturas de silsesquioxano sintetizadas in situ e na ausência de solventes são o objeto de estudo da presente tese. Esses materiais são inéditos e promissores para o desenvolvimento de dispositivos de regeneração óssea, liberação controlada de drogas e até mesmo enxertos de pele. Além disso, apresentam uma complexa nanoestrutura que é devida à ocorrência simultânea de três processos distintos: formação das estruturas de silsesquioxano, segregação de fases e cristalização do(s) polímero(s) orgânico(s). Neste trabalho, microscopia eletrônica de transmissão (TEM), associada à espectroscopia de perda de energia de elétrons (EELS), foi utilizada para investigar a morfologia dos híbridos O-I, assim como determinar a distribuição de estruturas de silsesquioxano em sua matriz. A correlação avançada de TEM com técnicas de espalhamento de raios X (SAXS/WAXS) permitiu obter informações quantitativas e modelos confiáveis para explicar a morfologia global e a nanoestrutura dos nanocompósitos híbridos O-I amorfos e semicristalinos. Nanocompósitos híbridos O-I amorfos apresentaram morfologia similar à de qualquer polímero amorfo: denso e sem características observáveis. Já em sua nanoestrutura, nanocompósitos híbridos O-I amorfos mostraram nanopartículas esféricas, atribuídas às cadeias randômicas de polissilsesquioxano (maior massa molar), uniformemente dispersas numa matriz do tipo gel, a qual é formada por cadeias de PCL e/ou PEG reticuladas aleatoriamente por estruturas poliédricas de silsesquioxano do tipo gaiola (menor massa molar). Nesse caso PCL/PEG mostraram-se indistinguíveis e potencialmente miscíveis. Por outro lado, nanocompósitos híbridos O-I semicristalinos apresentaram separação macroscópica das fases PCL e PEG, apesar de ambas mostrarem-se efetivamente reticuladas. Em termos de sua morfologia, híbridos O-I semicristalinos apresentaram morfologia esferulítica similar a qualquer homopolímero semicristalino. Já em sua nanoestrutura, híbridos O-I semicristalinos apresentaram nanopartículas de polissilsesquioxano, localizadas nas regiões amorfas interesferulíticas e interfibrilares, e domínios ordenados do tipo gel, reticulados por estruturas de silesesquioxano, localizados na região interlamelar. Em conclusão, neste trabalho foram obtidas informações relevantes sobre a morfologia e nanoestrutura de nanocompósitos híbridos O-I multicomponentes que poderão contribuir para o desenvolvimento de dispositivos biomédicos funcionais.

ABSTRACT

Solvent-free organic-inorganic (O-I) hybrid nanocomposites made up of polycaprolactone (PCL) and poly(ethylene glycol) (PEG) and cross-linked by *in situ* generated silsesquioxane structures are the subject of study of the present thesis. These materials are previously unreported and are promising new skin grafts, bone regeneration devices, or even drug delivery devices. Moreover, these materials show a complex morphology and nanostructure due to the occurrence of three competing processes: silsesquioxane formation, phase segregation and the organic polymer(s) crystallization. In this work, transmission electron microscopy (TEM), associated with the electron energy-loss spectroscopy (EELS), was used to investigate the O-I hybrid morphology as well as to determine the silsesquioxane distribution within the overall nanostructure. The advanced correlation of TEM with synchrotron X-ray scattering techniques (SAXS/WAXS) led to quantitative information and reliable models to explain the overall morphology and nanostructure of both amorphous and semicrystalline O-I hybrid nanocomposites. Amorphous O-I hybrid nanocomposite morphology is similar to any other amorphous polymer: dense and without distinct observable features. Amorphous O-I hybrid nanocomposites, at their nanostructure, showed spherical nanoparticles, related to random polysilsesquioxane chains (high molecular weight), uniformly distributed throughout a homogeneous cross-linked gel-like matrix, made up of PCL and PEG chains randomly cross-linked by polyhedral silsesquioxane cages (low molecular weight). In this case, PCL and PEG were undistinguishable and potentially miscible. Conversely, semicrystalline O-I hybrid nanocomposites showed macroscopic PCL/PEG phase segregation, irrespective of the fact that both phases were effectively cross-linked. In terms of morphology, semicrystalline O-I hybrids showed a spherulitic morphology similar to the one reported for conventional semicrystalline homopolymers. In terms of nanostructure, semicrystalline O-I hybrids also showed polysilsesquioxane nanoparticles, mainly located in the interfibrillar and interspherulitic amorphous regions, and also organized gel-like domains cross-linked by silsesquioxane, mainly distributed in between the interlamellar amorphous regions. Ultimately, these results provided important insights into the morphology and nanostructure of these complex multicomponent O-I hybrids, contributing to the development of functional biomedical devices with enhanced flexibility, transparency and, possibly, cell adhesion properties.

FIGURES

TABLES

EQUATIONS

Acronyms & Symbols

Symbol	Meaning
2θ	Scattering semi-angle (see Figure 13)
^{29}Si NMR	^{29}Si Nuclear Magnetic Resonance (see section 3.3.2)
$\sigma_{atom}\rho$	Mass thickness
$\Delta\rho$	Electronic density difference (see Equation 3)
X_{DSC}	Degree of crystallinity (see Equation 20)
X_{SAXS}	Linear degree of crystallinity (see Equation 18)
χ_{WAXS}	Mass degree of crystallinity (see Equation 17)
λ	Radiation wavelength
λ'	Mean free path (see Equation 2)
ADF	Annular Dark Field
AFM	Atomic Force Microscopy (see section 3.3.14)
ATR-IR	Attenuated Total Reflectance – Infrared spectroscopy (see section 3.3.1)
BF	Bright Field
CD	Degree of condensation (see Equation 26)
d_{Bragg}	Distance between atomic planes
D_{hkl}	Long-range ordering in the (h k l) crystalline orientation (see Equation 7)
D_{HP}	Density calculated by Helium Picnometry (see section 3.3.5)
D_{max}	Maximum dimension of the scattering object
d_s	Correlation distance (see Equation 9)
DF	Dark Field
DP	Diffraction Pattern
DSC	Differential Scanning Calorimetry (see section 3.3.4)
EDS	Energy Dispersive X-ray Spectroscopy
EELS	Electron Energy-Loss Spectroscopy
ESI-TEM	Electron Spectroscopic Imaging
ESRF	*European Synchrotron Radiation Facility*
FWHM	Full Width at Half-Maximum
HAADF	High Angular Annular Dark Field
HNO_3	Nitric Acid
IPTES	(3-isocyanatepropyl) triethoxysilane (see Figure 23)
K_p	Porod's Constant (see Equation 12)
L	Long Period (see Equation 13)
l_a	Thickness of the amorphous spacing in a semicrystalline polymer lamellar arrangement
l_c	Crystalline phase thickness in a semicrystalline polymer lamellar arrangement
L_c	Length of coherence (see Equation 10)
LNNano	*Brazilian Nanotechnology National Laboratory*
LNLS	*Brazilian Synchrotron Light Laboratory*
M_w	Molecular weight
M_n/M_w	Dispersity
MFP	Mean Free Path
O-I hybrid	Organic- Inorganic hybrid

P123	Pluronic, a block copolymer made up of poly(ethylene glycol) and poly(propylene glycol)
PCL	Poly(ε-caprolactone) (see Figure 2)
PEG	Poly(ethylene glycol) (see Figure 2)
PSS	Polysilsesquioxane
POSS	Polyhedral oligomeric silsesquioxane structures
q	Scattering vector (see Equation 8)
Q	Invariant (see Equation 5)
Q_{II}	Peak II invariant – refers to high intensity crystalline peaks
Q_{III}	Peak III invariant – refers to broad peaks related to silsesquioxane cages
Q(Δρ)	Calculated invariant (see Equation 27)
Q^{exp}	Experimental invariant (see Figure 43)
Q_i	Ideal invariant (see Figure 17)
R_s	Scherrer´s radius (see Equation 11)
r_{TH}	Minimum resolvable distance (see Equation 1)
S	Water uptake (see section 3.3.7)
SAXS	Small-angle X-ray Scattering (see section 1.4)
SEM	Scanning Electron Microscopy
SS	Silsesquioxane Structures
STEM	Scanning and Transmission Electron Microscopy
T^1	Silicon atom with a single Si-O-Si bond (see Figure 8)
T^2	Silicon atom with two Si-O-Si bonds (see Figure 8)
T^3	Silicon atom with three Si-O-Si bonds (see Figure 8)
T_c	Crystallization temperature
T_g	Glass transition temperature
T_m	Melting temperature
TEM	Transmission Electron Microscopy (see section 1.3)
TGA	Thermogravimetric Analysis (see section 3.3.6)
THF	Tetrahydrofuran
VLM	Visible Light Microscopy
WAXS	Wide-angle X-ray Scattering (see section 1.4)
W_r	Residue expressed in weight percentage obtained from TGA
W_s	Soluble fraction (see Equation 19)

SUMMARY

1

INTRODUCTION

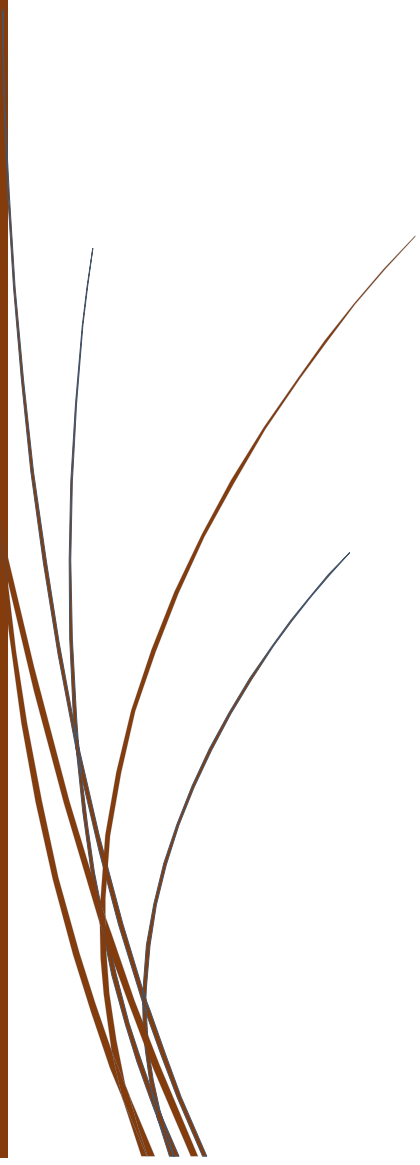

Laura Caetano Escobar da Silva
INSTITUTE OF CHEMISTRY

1. INTRODUCTION

Biomaterials science comprises the development and application of all sorts of natural- and/or synthetic-based materials within a biological context. It is a highly multidisciplinary and application driven field of research which encompasses: the development of new materials; the development of new preparation methods for well-known materials; as well as the comprehension and tailoring of device-tissue interactions [1]. Up to now, the high specificity of each biological tissue or organism drove most of the research in this field to concentrate their efforts on the development of biomedical devices designed specifically towards a tissue and/or lesion. Therefore, research papers that do not propose an application for a fully built device are sparse. On the one hand, most of them include biological testing, either *in vivo* or *in vitro*, aiming to investigate the device cytotoxicity, biocompatibility and bioactivity. On the other hand, the physical-chemical aspects of the material itself, as well as their effect on the device-tissue interactions, are frequently overlooked.

Biomedical devices might be either intended for tissue repair or substitution. Devices designed to substitute a specific tissue or organ are expected to be durable and mechanically compatible with the surroundings. Conversely, devices envisaged for tissue regeneration are expected to be biodegradable, in order to avoid a second surgery to implant removal, after tissue regeneration has occurred [2]. Nevertheless, biodegradation gives rise to a number of new aspects to be considered in the scaffold design, since the material evolution over time must be monitored [3]. In particular, care should be taken to prevent toxic species production and liberation during degradation, as well as the premature loss of mechanical properties.

In both cases, even though the toxicity might be tolerated at different levels from tissue to tissue, it is invariably the limiting factor for the biomedical application of any sort of material [1]. Moreover, device-tissue integration is key, since it prevents inflammatory responses, necrosis and implant rejection. Implant-tissue integration is a science of its own, since the parameters affecting it are particular for each tissue or organ. However, generally speaking, implant-tissue integration is based on cell adhesion and body fluid permeation. Cell adhesion is dependent on surface properties and composition, while body fluid permeation is dependent on bulk physical-chemical properties and device architecture. Surface properties that are relevant to cell adhesion encompass roughness, charge, hydrophilic character and surface energy [4]. In terms of bulk physical-chemical properties

that affect body fluid permeation, the hydrophilic character and permeability are the most significant. Finally, in terms of architecture, porosity and morphology need to be considered [5].

Figure 1 schematically shows the relationship between time-scale and length-scale of the processes involved in implant-tissue integration. As can be verified, these processes are dependent on features present at all length-scales. For example, the topography of the device, which is a macroscopic feature, may impair implant-tissue integration due to geometric difficulties to cell adhesion. In the opposite direction, local compositional changes, which are a submicrometric feature, may also impair cell adhesion due to the lack of binding sites to the signalling proteins. Moreover, the device-tissue integration chain of events starts from processes at the nanometric length-scale and escalates to macroscopic events. Therefore, ultimately it is the device's micro and nanostructure that governs device-tissue integration, since it rules all the molecular phenomena involved.

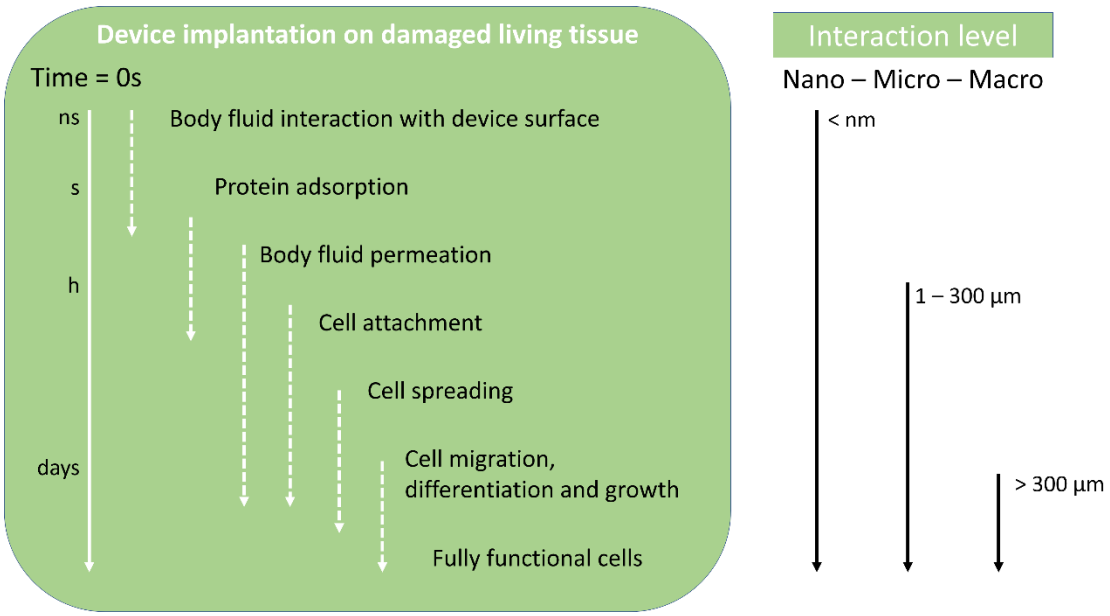

Figure 1 - Time- and length-scales of the biological processes involved in implant-tissue integration. Adapted from Roach et al [6].

At first glance, one might expect that, in order to achieve successful implant-tissue integration, a compositionally uniform device, at all length-scales, would be desired. However, that is not entirely true. Heterogeneities at the micrometric and nanometric length-scales might in fact be beneficial. In particular, devices that present balanced hydrophilic and hydrophobic moieties shows synergistic properties which have the great advantage of promoting implant-tissue integration [7,8]: the hydrophilic moieties allow body fluid permeation while the hydrophobic moieties promote the signalling protein adsorption, increasing cell attachment rate [9,10]. For that reason, an

increasing number of studies concentrates on the production of multicomponent devices [11–14]. To do so, polymeric matrices are the most widely explored, due to ease of processing and to a variety of biocompatible polymers available, most of which are hydrophobic.

In this context, devices that combine poly(ε-caprolactone) (PCL) and poly(ethylene glycol) (PEG) in the form of blends, copolymers or crosslinked materials, are probably the most widely studied in the biomedical field. Nevertheless, the nanostructural details of these combinations are not fully understood yet, due to their complexity as well as to difficulties involved in the detailed characterization of soft materials. Herein, biomedical devices combining PCL and PEG were prepared by cross-linking the organic polymers with *in situ* generated silsesquioxane structures. Silsesquioxanes were chosen as cross-linkers due to the recently demonstrated fact that Si compounds are beneficial to a number of biological processes. Nevertheless, the biological characterization of the novel materials developed herein, in order to access their potential as skin grafts, is outside the scope of this thesis. The present thesis concentrates instead on comprehending the morphology and nanostructure of these biomedically relevant organic-inorganic hybrid nanocomposites at the micron to Angstrom length-scale range.

1.1. POLYCAPROLACTONE AND POLY(ETHYLENE GLYCOL)

Poly(ε-caprolactone) (PCL) and poly(ethylene glycol) (PEG or PEO) are linear, semicrystalline and biocompatible synthetic polymers which are widely explored in the field of biomaterials science. PCL is widely used for the production of bone regeneration and tissue engineering devices due to its biodegradability and mechanical strength. PEG, on the other hand, is widely explored for the production of hydrogels for diverse application. PCL and PEG combinations (blends and copolymers) are broadly studied for the production of drug delivery systems, biodegradable devices and hydrogels[1].

PCL may be synthesised either through the (6-hydroxyhexanoic) acid polycondensation or through the ε-caprolactone ring-opening polymerization. Both monomers are by-products of the cyclohexanol conversion into adipic acid and, therefore, are readily available. On the one hand, polycondensation occurs under enzymatic catalysis and mild heating. On the other hand, ring opening polymerization occurs under metal-based catalysis and higher temperatures. Even though polycondensation has significant limitations in molar mass control, it is still the most widely employed route for industrial PCL synthesis. Conversely, ring opening polymerization is the

preferred route for bench scale synthesis, due to the possibility of achieving higher molecular heights (M_w) with a narrower molar mass distribution (M_w/M_n) [15]. Figure 2 (top) shows the ε-caprolactone and the PCL chemical structures. Tin 2-ethyl hexanoate ($Sn(Oct)_2$) is the most widely employed metal-based catalyst for the synthesis of poly(α-hydroxy acids), such as PCL, via ring opening polymerization. However, $Sn(Oct)_2$ is toxic. Therefore, recently several studies have been focusing on $Sn(Oct)_2$ substitution by using less toxic catalysts, such as zinc-based or calcium-based catalysts [16,17].

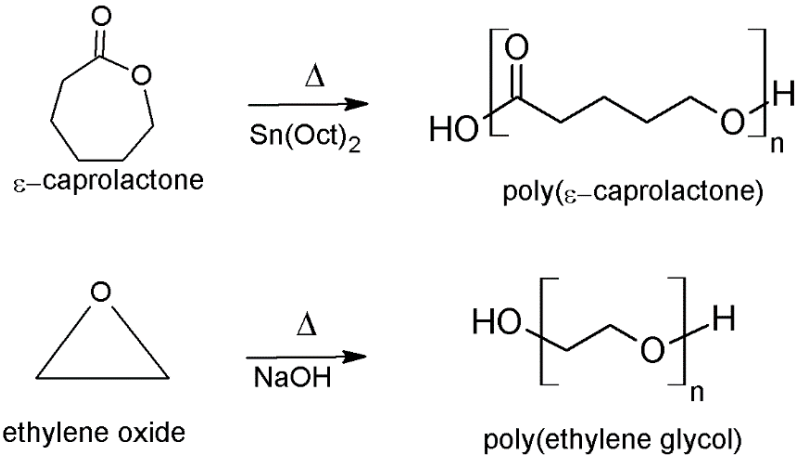

Figure 2 - Representation of poly(ε-caprolactone) (top) and poly(ethylene glycol) (bottom) syntheses by ring-opening polymerization from, respectively, the ε-caprolactone and ethylene oxide monomers.

Figure 2 (bottom) also shows ethylene oxide and PEG chemical structures. Typically, the term poly(ethylene glycol), or PEG, is used when M_w is lower than 20 000 g mol^{-1}, while the term poly(ethylene oxide), or PEO, is used when M_w is higher than 20 000 g mol^{-1}. PEG or PEO industrial synthesis occurs through the alkali-catalysed ring opening polymerization of the ethylene oxide monomer in the presence of ethylene glycol. Reports on the bench-scale syntheses are rare, which is attributed to the infrastructural difficulties involved in manipulating the gaseous monomer and the extreme exothermic reaction. PEG is not only cheap but also commercially available in a wide M_w range. Typically PEG chain ends are hydroxyl groups. Nevertheless, nowadays PEG is also commercially available, though at a much higher price, in distinct architectures and with various other terminal groups, due to its popularity in the biomedical field [18].

While PEG is a polyether with a C_2H_4O minimal formula, PCL is a polyester with a C_3H_5O minimal formula. Their distinct functional groups lead to discrete Hansen solubility parameters: $\delta_{DPH} = 16.1$ for PCL and $\delta_{DPH} = 24.0$ for PEG; which is the reason why they are immiscible. In both PCL and PEG the δ_D value, which accounts for the dispersive contribution (van der Waals), is the

major component of the Hansen parameter. However, in PCL the δ_P value, which accounts for the polar contribution, and the δ_H value, which accounts for the hydrophilic contribution, are minimal. Therefore, while PCL is hydrophobic, PEG is hydrophilic [19]. At first glance, one might argue that ester bonds are more polar than ether bonds and, therefore, PCL is expected to be the most hydrophilic component. However, the inductive effect caused by the five methylenic units in between ester bonds (Figure 2) make PCL highly hydrophobic, while PEG remains hydrophilic [20].

In biomedical applications, synthetic polymers have the advantage of availability and controlled architecture, due to the reproducible synthetic methods that allow M_w and M_w/M_n tailoring and control. Nevertheless, synthetic polymers frequently present biocompatibility issues or even toxicity, due to residuals generated during synthesis. PCL is biodegradable, while PEG is soluble in water [21,22]. PCL biodegrades through surface hydrolysis, since water molecules promote the ester-bond cleavage, generating atoxic carboxylic acids or diacids, which are absorbed and excreted naturally [3]. In contrast, upon implantation, low M_w PEG may be lixiviated and excreted in urine. High M_w PEG is seldom lixiviated due to the elevated degree of crystallinity [1]. As a consequence, PCL and PEG combination is largely attractive [23,24] and has already been reported in the form of hydrogels [25,26], blends [23,27] and/or copolymers [8,28–31], aiming towards both biodegradable and non-degradable devices. Tailoring the polymer architecture, the nanostructure and the macroscopic morphology are key aspects in determining device performance and degradability upon implantation [32,33].

Device performance is greatly affected by the processing method. In particular, melt-processing methods such as extrusion [22,36] are preferred due to the PCL/PEG similar thermal properties, as well as the method's low cost and low toxicity, which in turn is due to the absence of solvent. However, device manufacturing is not the only aspect to be considered when tailored morphology and nanostructure are intended. In fact, the type of polymer mixture (i.e. blends or copolymers) as well as the competition between crystallization and phase separation are key. The type of polymer mixture exerts significant influence over the extent of phase separation as well as domain sizes [23]. As a rule, in both blends and copolymers, the higher the components M_w, the higher the thermodynamic driving force for phase separation. However, it is mostly the type of mixture, rather than the driving force for phase separation, that dictates domain sizes. Usually blends show disordered and micrometre-sized domains with irregular shape and size distribution [23,27], while

block copolymers frequently show ordered nanometre-sized domains with a definite morphology and narrow size distribution [28,29].

In terms of mechanical performance, the PCL and PEG combination offers the advantage of the components having similar Young´s modulus, which avoid device failure due to uneven load distribution upon mechanical solicitation, even at an advanced degradation state [34]. Another advantage of the PCL/PEG combination is their similar thermal properties, since it allows easy processing and device manufacturing. PCL and PEG show similar glass transition (T_g), melting (T_m) and crystallization (T_c) temperatures [29]: $T_g \approx -60$ °C, $T_m \approx 60$ °C and $T_c \approx 35$ °C for PCL, and $T_g \approx -50$ °C, $T_m \approx 50$ °C and $T_c \approx 45$ °C for PEG [35]. In addition, at comparable M_w, PCL and PEG show similar degree of crystallinity, though PCL is flexible and PEG is fragile [10].

In polymer blends, the common approach to tackle the domain size issue is the use of homopolymers with distinct M_w, associated with advanced preparation methods such as rapid prototyping [27,37,38]. In PCL/PEG blends, usually PCL is used in a higher M_w than PEG. This is due to the fact that PCL is flexible and impact resistant, while PEG is rigid, however hydrophilic. From this strategy, Dong et al. [27] and Mirhosseini et al. [37] have successfully increased PCL hydrophilicity through the electrostatic spinning of a PCL and PEG [27] or Pluronic P123 [37] blend. P123 is a triblock copolymer made up of PEG and poly(propylene glycol)). Due to the fact that P123 is amorphous, Mirhosseini et al. [37] (PCL 80 000 g mol^{-1}; PEG 5 800 g mol^{-1}) studied only the phase separation phenomena and showed that above 20 wt% P123 concentration, the fibre surface saturated and the excess P123 would be entrapped within the fibre bulk. Conversely, Dong et al. [27] investigated only the crystallization phenomena and verified that PCL (52 000 g mol^{-1}) and PEG (2 000 g mol^{-1}) crystallized separately. The authors showed that PCL and PEG crystal structure and crystallization mechanisms were unaltered in relation to the respective homopolymers, however, their coexistence allowed thicker crystals and more perfect crystallites to be formed on both phases, indicating a templating effect. It is important to point out that no morphological or quantitative information on phase separation was provided in Mirhosseini's work [37].

The strategy of using a very low M_w component is based on the assumption of increased miscibility. Nevertheless, up to now, no one has succeeded in suppressing the microscopic phase separation in crystalline PCL/PEG blends. As an alternative, several studies have concentrated on the competition between crystallization and phase separation, in order to produce microscopically uniform devices. In a series of studies, Chuang et al. [21,23] have investigated the effect of annealing

from the melt, as well as blend composition, in the morphology of PCL/PEG blends (PCL 10 000 g mol^{-1}; PEG 400 g mol^{-1}) and built up a phase separation diagram for this system. From that information, the authors chose the 70/30 PCL/PEG blend to perform an isothermal crystallization at 48 °C, in which phase separation and crystallization occurred simultaneously, even though spinodal decomposition of the liquid-liquid mixture started earlier. In this system, PEG is amorphous and segregated into the interspherulitic and interfibrillar regions of the PCL spherulites. PCL crystallization rate was not affected by PEG presence.

Typically, PEG homopolymer crystallizes in monoclinic crystals with 28 monomers per unit cell, in which a = 7.51 Å, b = 13.35 Å and c = 19.90 Å[35], while PCL homopolymer crystallizes in orthorhombic crystals with 4 monomers per unit cell in which: a = 7.45 Å; b = 4.98 Å and c = 17.04 Å [39,40]. Qiu et al. [41] (PCL 14 300 g mol^{-1}; PEO 100 000 g mol^{-1}) showed that PCL and PEG crystallize separately and are immiscible. PCL crystal lattice and crystallization rate or mechanism were not affected by the PEG presence. Conversely, PEG suffers a confinement effect from the PCL crystalline phase which lowers PEG crystallization rate, while crystal lattice and crystallization mechanism are unaltered. To summarize, it is widely accepted that PCL and PEG do not co-crystallize, since they always retain their distinct crystal lattices. However, a templating effect sometimes occur, leading to crystalline phases of the same thickness, in spite of PCL/PEG physical separation into domains. Moreover, PEG crystallization is largely influenced by PCL, while PCL crystallization is fairly unaffected by PEG. In PCL/PEG blends, the crystalline behaviour is well-known, however phase separation behaviour is still unclear.

Conversely, in block copolymers, several studies have shown that PCL/PEG blocks are miscible at the molten state [42]. In block copolymer systems, the segregation strength is due to the product of the Flory-Huggins interaction parameter and the degree of polymerization, both of which are related with M_w [43]. Therefore, the control of M_w may enable tailoring of the extent and stability of phase separation and, therefore, the device nanostructure. This nanostructural versatility is the most advantageous aspect of the PCL/PEG block copolymers, since it allows one to obtain a number of distinct morphologies. Extensive research has been done on that topic, for both diblock [28,30,44] and triblock [17,29,45] PCL/PEG copolymers. In the latter, most often PEG is the central block. As a general rule, PCL crystallizes first, unless the PCL block M_w is smaller than PEG block M_w, in which case the crystallization events are frequently overlapped. The low driving force for PCL and PEG phase separation leads to melt miscibility, which reduces both blocks T_c, in comparison with their

homopolymers [42]. Moreover, the M_w of each block has significant influence over the crystalline behaviour of the blocks. For example, by fixing PEG M_w and increasing PCL M_w, PEG T_c and T_m are reduced, while PCL T_c and T_m are increased [17,44].

When phase separation occurs prior to crystallization in PCL/PEG block copolymers, a soft confinement environment is imposed for both PCL and PEG blocks. Usually, PCL crystallization is insensitive to the soft confinement and disrupts the phase separation morphology by the formation of a spherulitic superstructure, which acts as a hard confinement environment for the PEG subsequent crystallization [42]. He et al. [44] showed that for symmetric PCL/PEG diblock copolymers (PCL 5 900 g mol^{-1}; PEG 5 000 g mol^{-1}), this phenomenon leads to the formation of concentric spherulites upon PEG crystallization, since PEG crystallizes in the interfibrillar region of the PCL spherulite. Conversely, Xue et al. [46] showed that for asymmetric diblock copolymers (PCL 10 000 g mol^{-1}; PEG 5 000 g mol^{-1}) an alternate periodic crystalline structure, as shown in Figure 3, is obtained and leads to a single spherulitic superstructure. In this case, the PCL and PEG crystalline lamellae are separated by a homogeneous amorphous layer in which PCL and PEG are miscible.

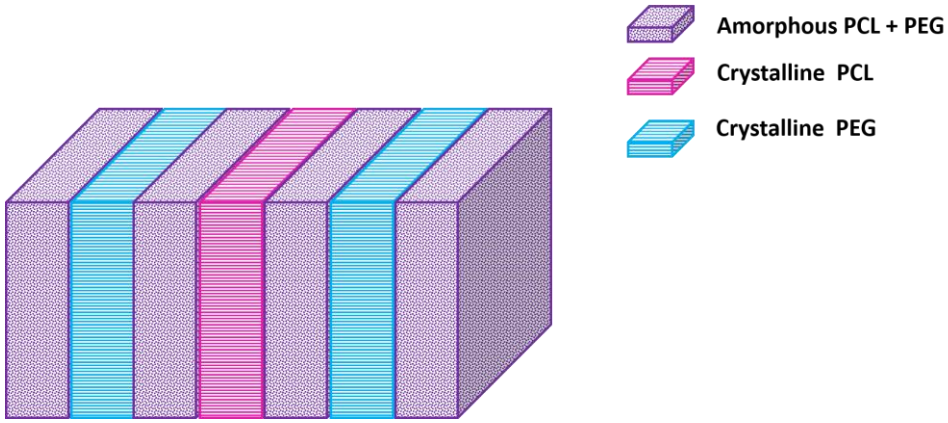

Figure 3 - Morphology of a double crystalline and asymmetric PCL/PEG diblock copolymer. Adapted from Xue et al. [46].

If PCL and PEG blocks are highly asymmetric in a diblock copolymer (PCL 24 000 g mol^{-1}; PEG 5 800 g mol^{-1}), as shown by Li et al. [28], PCL/PEG phase separation and PCL crystallization might occur simultaneously, leading to the formation of a PCL crystalline structure with spherical PEG domains orderly distributed at the PCL amorphous layers, as shown in Figure 4. In this case, subsequent PEG crystallization occurs under hard confinement and, therefore unidirectionally, leading to domain deformation. Hard confinement environments usually significantly modifies PEG crystalline behaviour, resulting in full crystallinity suppression when the PEG block is sufficiently

small [17]. Conversely, PCL crystallinity suppression due to hard confinement is seldom reported, however, it may also occur [45,47].

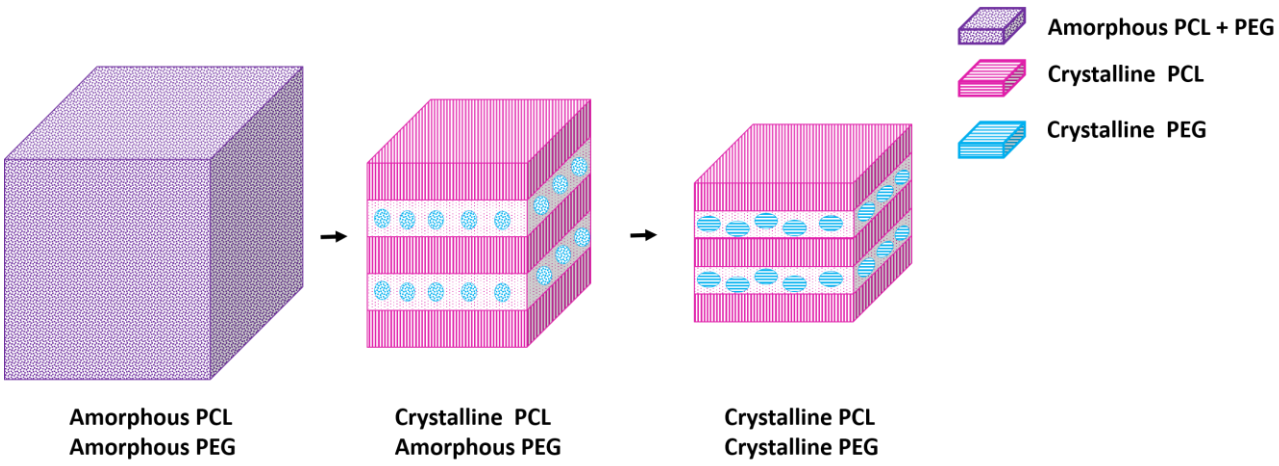

Figure 4 – Morphological evolution of a highly asymmetric PCL-b-PEG copolymer from the melt. PCL and PEG are miscible while melted (left). PCL crystallizes first in a lamellar arrangement (middle) and spherical PEG domains are formed in the interlamellar amorphous region. Finally, PEG crystallizes unidirectionally deforming the domains. Adapted from Li et al. [28].

Finally, another interesting approach to PCL and PEG combination is cross-linking. Cross-links are chemical or physical interactions that bind two or more polymeric chains together [49,50]. The resulting materials are versatile and three-dimensional networks that might be either rigid and stiff or soft and porous. If on the one hand, PCL/PEG blends and copolymers have been intensively investigated in the last few decades, on the other hand, the interest in PCL/PEG cross-linked materials is recent. In general, the same trends and behaviours found for PCL/PEG blends and copolymers also apply to PCL/PEG cross-linked materials. However, due to the reduced synthetic control in cross-linked systems, these are usually complex and heterogeneous. As a consequence, their morphology and nanostructure are frequently overlooked. Taking into consideration the device's nanostructure importance to the material's biomedical performance, in the present thesis, it is of interest to thoroughly investigate the morphology and nanostructure of potential biomedical devices made up of PCL and PEG, cross-linked by silsesquioxane structures.

1.2. CHEMICALLY CROSS-LINKED O-I HYBRID NANOCOMPOSITES

In biomaterials science, cross-linked materials are interesting for cartilage repair and bone substitution, due to their resilience and load support [26,51], as well as to drug delivery and tissue engineering devices due to the facilitated water flow throughout the device that, in turn, allows to retain and deliver small molecules or even cells [12,52]. The mechanical resilience in chemically cross-linked materials is due to interchain bonding and allows the material to endure compression and various other types of mechanical solicitation without changing shape or rupturing. As a result of mechanical resilience, facilitated water flow is also observed[53]. Typically, cross-linked materials are multicomponent and the combination of hydrophilic and hydrophobic polymers, such as PCL and PEG, is widely explored. The multicomponent approach is widespread in this field of research due to the fact that phase compatibility is less of an issue in cross-linked systems and, therefore, synergistic properties are more easily achieved. In addition, the interchain bonding between antagonistic molecules facilitates the tailoring of properties such as elasticity, water uptake, and biodegradation rate [2,54].

Cross-linked materials are extremely versatile and may be obtained in various ways. Synthetic routes based on the sol-gel technique are an interesting approach due to their mild reaction conditions. The increasing use of the sol-gel technique associated with advanced preparation methods [55] has led to the development of injectable *in situ* gel forming systems in which the gelation point is achieved directly onto the lesion site [56,57]. As an example, Ni et al. [26] have developed injectable hydrogels based on a PCL/PEG block copolymer using hexamethylene diisocyanate as a cross-linking agent and the sol-gel technique. These materials were targeted for bone regeneration of cranial defects and have proven to be promising candidates for bone substitution in non-load bearing sites. Moreover, these gels have also shown a thermosensitive behaviour, which was also verified by others [51,58] for similar chemically cross-linked PCL and PEG gels. In terms of PCL/PEG cross-linked devices, it is important to point out that if the chain length in between cross-linking nodes is sufficiently high, they might crystallize [50,59].

The sol-gel technique consists of the transition from a colloidal suspension (sol) to a three-dimensional material containing liquid entrapped (gel) [60]. Sol-gel transition occurs at the gelation point. Initially, a stable and homogeneous colloidal suspension (polymer solution or nanoparticle dispersion) of low viscosity is mixed with the cross-linking agent. As the reaction proceeds, grains of a three-dimensional network start to form and grow, up to a point in which

grains start touching each other, forming a percolated network. This is the gelation point. In spite of the physical constraints and viscosity increase imposed by the gelation, the cross-linking reaction proceeds, though locally and at a much slower rate. This process is called aging and allows intergrain bond formation, providing structural stability to the gel [60–62]. Due to the mechanism of gel coagulation, shown schematically in Figure 5, gels usually exhibit a fractal nanostructure, which provide a hierarchically porous morphology that is advantageous to the biomedical field.

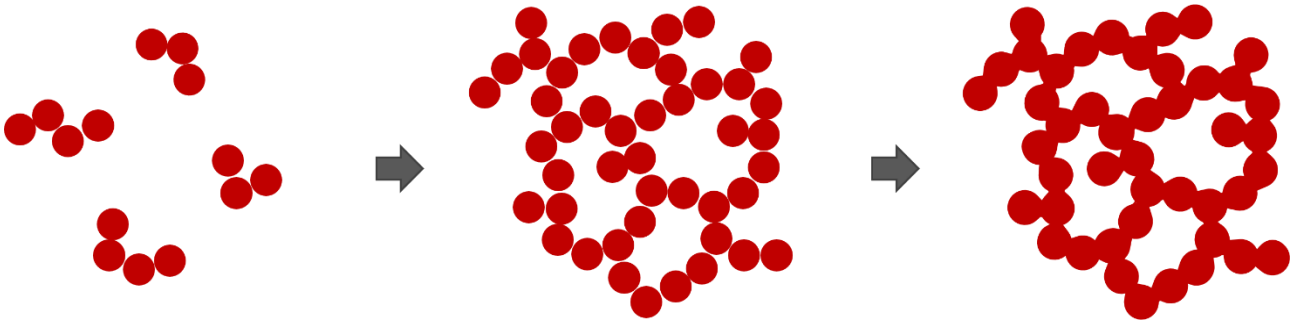

Figure 5 - Demonstration of a sol-gel process: initially a colloidal suspension forms grains of a three-dimensional network. As the grain concentration increases, grains start touching each other at the gelation point (middle), after which ageing promotes intergrain bonding. Adapted from Kumar et al. [62].

The sol-gel process, however, is not restricted to the production of polymeric gels. In fact, the sol-gel technique was developed for the preparation of siloxane-based materials, such as glasses or organic-inorganic (O-I) hybrids [63]. In order to produce siloxane-based materials, alkoxysilanes are used as cross-linking agents [62]. Recently it has been established, despite previous concerns, that Si compounds are actually beneficial to a number of biological processes [64]. Based on this, a new emerging market for the silicon-based materials has arisen and, therefore, nowadays the number of studies concerning their biomedical applications is increasing rapidly.

The main advantage of using silicon-based materials as implantable devices is that silicon-based materials show enhanced ability to adhere and proliferate cells, due to the Si participation in the production of collagen [64]. This is especially interesting for the development of bone regeneration scaffolds [65,66]. Another advantage, recently shown by Talal et al. [12], is the polysilsesquioxanes ability to promote zero-order drug release. In contrast, one of the major concerns in using silicon-based materials in the biomedical field is removing all toxic reagents from the synthesis. The use of solvents and catalysts, in particular, have to be avoided, since they may leave residues behind.

A class of silicon-based polymeric materials are the polysiloxanes. However, siloxane is a broad classification that encompasses all the available hybrid molecules and macromolecules

made up of carbon, oxygen, silicon and hydrogen that contain Si-O-Si bridges [67]. Siloxane structures might be synthesised by the hydrolysis-condensation of organoalkoxysilanes, $RSi(OR')_3$, in which R' is usually $-C_2H_5$, or even $-CH_3$ [68]. Figure 6 shows a generic representation of all the possible organoalkoxysilanes, in which R might be an organic macromolecule, an organic chain, or even a H atom. Tetraalkoxysilanes are used mostly to obtain silica (SiO_2) particles and zeolites, while trialkoxysilanes are used to produce silsesquioxanes. In contrast, dialkoxysilanes are used mostly to obtain silicones, such as poly(dimethylsiloxane). Finally, monoalkoxysilanes are used as termination units for the preparation of silicones and cross-linked silicone-based resins (which are a mixture of distinct alkoxysilanes) [67].

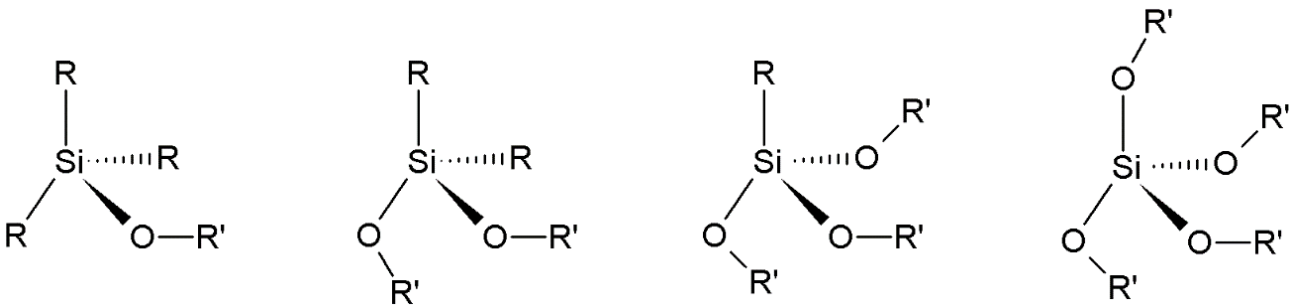

Figure 6 – Generic chemical structures of possible organoalkoxysilane used for siloxane synthesis. R represents any organic chain (polymeric or not) and R' represents -H, $-CH_3$ or $-C_2H_5$ groups.

In order to turn an organoalkoxysilane into a siloxane or polysiloxane, hydrolysis and condensation reactions, shown schematically in Figure 7 for a trialkoxysilane, are carried out. Even though, both the hydrolysis and the condensation rates are highly affected by the organic substituents R' and R, respectively, the limiting step to siloxane formation is hydrolysis. Alkoxy radical hydrolysis produces silanol groups, which condensate to form Si-O-Si bonds. In the case of silsesquioxane formation, Si-O-Si bridges further condense into $(SiO)_4$ rings that make up the silsesquioxane backbones [69]. Acids [49], bases [70] or organometallic substances, such as dibutyltin dilaurate (DBTDL) [71], may catalyse hydrolysis. However, it is widely accepted that different catalysts provide distinct Si-OH availability throughout the reaction media [72].

Diverse Si-OH availability leads to distinct silicon conformation within the silsesquioxane structure. As it is shown in Figure 8, a single silicon atom might be participating in either one (T^1), two (T^2) or three (T^3) Si-O-Si bridges. As a consequence, random, cage-like or ladder-like silsesquioxanes may be obtained by the condensation of Si atoms into distinct conformations. Random and ladder-like siloxanes are called polysilsesquioxanes (PSS) and usually present high M_w. Random PSS shows elevated T^1 and T^2 contents, while ladder-like PSS shows elevated T^2 and T^3

contents. In contrast, cage-like silsesquioxanes, which show limited M_w, are mostly made up of T^3 Si atoms. Cage-like silsesquioxanes are polyhedral structures, which may be either partially open or closed, but are always limited to an even number of Si atoms ranging from 6 to 12. The most thermodynamically stable and, therefore, most widely investigated silsesquioxane structures are the closed cages, which are formed by 8 Si atoms, $(SiO)_8$, and show a cubic-like structure with a 0.5 nm average inner diameter [73].

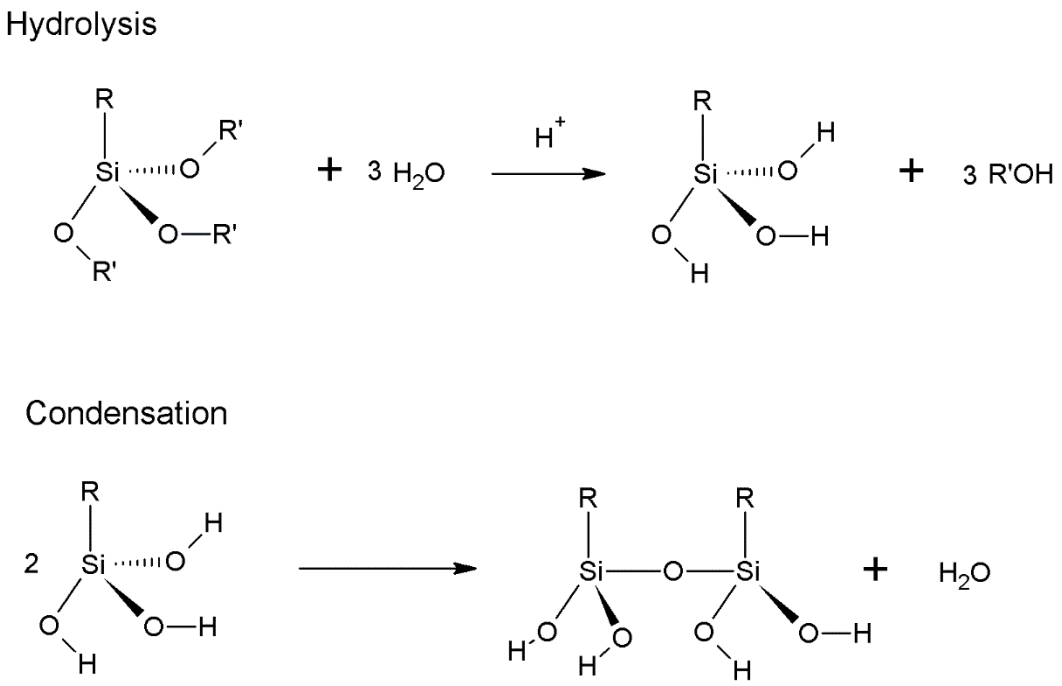

Figure 7 – Schematic demonstration of trialkoxysilane hydrolysis (top) and condensation (bottom) reaction to obtain silsesquioxane structures. R represents any organic chain (polymeric or not) and R' represents -H, -CH_3 or -C_2H_5 groups.

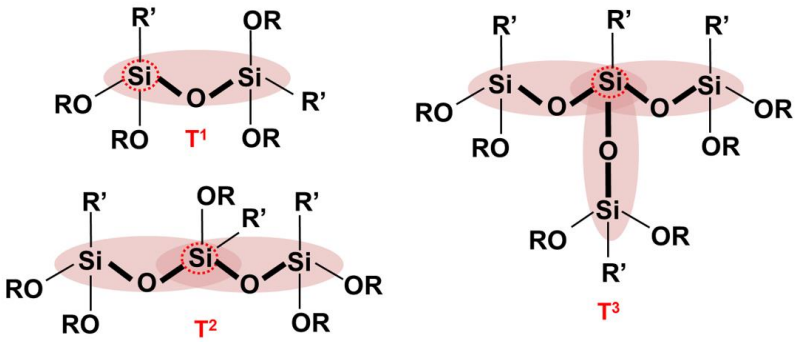

Figure 8 – Possible molecular conformations of a silicon atom within a silsesquioxane structure. T^1 Si atom is involved in a single Si-O-Si bond (top left), T^2 Si atom is involved in two Si-O-Si bonds (bottom left) and T^3 Si atom is involved in three Si-O-Si bonds (right).

Open silsesquioxane cages are mainly made up of T^3 atoms, but a small portion of T^2 atoms is also present. Open cages with sufficiently small R substituents may be further polymerized

into higher molecular weight random polysilsesquioxanes under high temperatures. Conversely, closed cages (only T^3 atoms are present) that also have sufficiently small R substituents, may form transparent soluble crystals upon solvent evaporation. Literature reports that the steric hindrance promoted by the R substituents that are larger than five to ten methylene units favours the formation of $(SiO)_8$ closed cages [74]. However, it also impairs $(SiO)_8$ crystallization, which ends up producing gel-like or glass-like solids [73]. The discovery of these gel-like solids, in the 1950's, opened up a new class of materials, the organic-inorganic (O-I) hybrids, that have been widely explored ever since.

In biomaterials science, O-I hybrids are the most widely investigated silicon-based materials due to their useful mechanical properties. O-I hybrids are flexible materials made up of siloxane structures and organic polymers [75]. Siloxane structures provide mechanical strength and enhance cell adhesion, while the organic polymers might provide several properties such as elasticity and hydrophilicity, which are a characteristic of polymeric materials [76]. The O-I hybrids classification within materials science is still a matter of debate. The most widely accepted classification is the one proposed by Loy and Shea [70], under the assumption that an organic-inorganic phase separation always occurs. The authors suggest that the inorganic domains size dictates whether that singular system is a blend, a composite, a nanocomposite or even a molecular composite. Moreover, the authors conclude that within a specific class (i.e. nanocomposites), distinct O-I hybrids should display similar physical-chemical properties, due to the similar interfacial area. However, sorting out O-I hybrids within this classification has been a challenge due to difficulties in determining their morphology and nanostructure.

The nanostructure of O-I hybrid nanocomposites is typically obtained from the interpretation of synchrotron small-angle X-ray scattering (SAXS) data. However, SAXS alone gives room for diverse interpretations and is limited, in terms of length scale, to a few hundreds of nanometres. Moreover, one has to know beforehand the number of phases present in the sample in order to correctly interpret the data. Even so, when contrast difference between phases is insufficient, they may be undistinguishable and mislead data interpretation. In contrast, it is a widespread knowledge that microscopic techniques also have limitations. In the case of O-I hybrids, the main limitation is the acknowledged difficulties involved in soft materials' sample preparation and beam damage. In addition, the field-of-view reduction, necessary to achieve higher resolutions, is also a matter of concern, since it may lead to wrongful conclusions. Therefore, in order to fully

understand the morphology and nanostructure of O-I hybrid nanocomposites, at all length scales, a combination of X-ray scattering, and electron microscopy techniques is, most probably, the best approach. Unfortunately, up to now few have succeeded in that undertaking.

For this reason, recently Kickelbick [77] proposed a new O-I hybrid classification based solely on the alkoxysilane prepolymer used for the formation of the inorganic moiety. In this new classification, O-I hybrids were divided into class I and class II. Class I hybrids are obtained by mixing organic polymers with siloxanes obtained from tetraalkoxysilanes. Conversely, class II O-I hybrids are obtained from the trialkoxysilanes [75]. In class I, the organic and inorganic O-I hybrid's moieties may or may not be covalently bonded and, therefore, microscopic, or even macroscopic, phase separation is expected. In contrast, in class II, the organic and inorganic O-I hybrid's moieties are always covalently bonded. In this latter case, nanometric phase separation or the even no phase separation at all is expected. In both class I and class II O-I hybrids, if present, the cross-linking nodes might be located either at the organic or at the inorganic moieties. When cross-links are at the organic moiety, O-I hybrids are usually obtained by binding pre-condensed siloxane structures with multi-armed organic polymers [66]. In contrast, the inorganic moiety cross-links are mostly verified in class II O-I hybrids, since they are usually obtained by the *in situ* formation of silsesquioxane structures by means of the sol-gel technique [12].

It is important to point out that PCL-based and PEG-based O-I hybrids have been following the same trends as the organic chemically cross-linked materials: PEG-based O-I hybrids currently under development, are targeting drug delivery devices [12,14,78]; while PCL-based O-I hybrids are revolving mostly around bone repair [65,66,79]. To the best of our knowledge, the present work is the first to report an O-I hybrid made up of both PCL and PEG. However, in a series of studies, Guo et al. [80–82] developed thermoplastic polyurethanes made up of a PCL and PEG terpolymer with an additional poly(L-lactide) block. This terpolymer also contained, at the PCL block, dangling polyhedral oligomeric silsesquioxane structures (POSS), which are the $(SiO)_8$ cages. These materials showed an atypical mechanical strength and indications of PCL/PEG miscibility. Moreover, the addition of a drug, Paclitaxel, promoted an antiplasticizer effect which could be counterbalanced by controlling the PEG content at the original terpolymer. This allowed a fine control of the mechanical properties and drug release profile. The work of Guo et al. [80–82] highlights the potential of combining PCL and PEG in O-I hybrid systems, since it opens up the possibility of achieving mechanically strong biomedical devices for controlled drug delivery in load-bearing sites.

In this context, the O-I hybrid nanocomposites made up of PCL and PEG as the organic moieties, and *in situ* synthesized silsesquioxane structures as the inorganic moiety, were synthesized using a new atoxic two-step pathway inspired by the sol-gel technique. In the first step, the solvent-free chemical modification of PCL and PEG chain ends, using triethoxysilyl radicals, was carried out, though separately, to ensure that both organic polymers were uniformly combined in the hybrid network. In the second step, which is the silsesquioxane structure formation, an aqueous and diluted nitric acid solution was used as a catalyst. Both crystalline and amorphous O-I hybrids were obtained. Advanced morphological characterization studies using electron microscopy and synchrotron X-ray scattering experiments were used to investigate in detail the complex morphology and nanostructure of these ternary hybrid nanocomposites at distinct PCL/PEG ratios.

1.3. TRANSMISSION ELECTRON MICROSCOPY

The electron microscopy development in the early 1930's allowed the nanotechnology field of research to rise and thrive, due to the surpassing of the limit resolution of visible light. In transmission electron microscopy (TEM), resolution is the minimum resolvable distance between two objects and is given by:

$$r_{TH} = \frac{1.22\lambda}{\beta} \qquad \text{Equation 1}$$

where β is the collection semi-angle of the magnifying lens and λ is the radiation wavelength. Even though, both visible light microscopy (VLM) and TEM resolutions are diffraction-limited, the minimum resolvable distance in VLM is in the order of 300 nm, while in TEM is in the order of 0.1 nm. The marked difference between VLM and TEM resolutions is due to the fact that the electron beam wavelength ($1.9\text{x}10^{-3}$ nm < λ < $3.7\text{x}10^{-3}$ nm) is considerably smaller than the visible light wavelength ($4\text{x}10^{2}$ nm < λ < $7\text{x}10^{2}$ nm). [83]

The transmission electron microscope is currently one of the most versatile tools for the materials characterization and there are over 40 distinct documented TEM modes (i.e. techniques), all of which have their specific field of application. TEM versatility is based on two aspects of TEM operation: the fact that an electron beam is an ionizing radiation, which means that it interacts with matter; and the use of thin and electron-transparent specimens, which increases the number of distinct signals available to detect. An electron can interact with matter as both a particle and a wave, which increases even further the number of secondary signals available to work with. The most commonly used signals in TEM are the direct beam, the elastically or inelastically scattered electrons and the X-rays. Moreover, the secondary and backscattered electrons are widely used in the scanning electron microscopy (SEM), in which secondary electrons give topographical information and backscattered electrons show local compositional changes of non-electron transparent specimens.

The direct beam is the most well-known and widely explored TEM signal, since it provides bright field (BF) images. BF images are formed by selecting the direct beam (through the positioning of the objective lens aperture) and removing most of the scattered electrons. In BF micrographs the overall field-of-view is bright (since the sample is electron transparent) and the regions that show increased mass thicknesses are presented in different shades of grey due to the electron beam blockage at distinct extents. Mass thickness is the product of the number of

scattering events per unit distance by the thickness of the sample. Mass thickness is the main event responsible for the contrast in BF images of amorphous materials and is governed by the energy of the electron beam as well as the average atomic radius of the sample. At this point, it is important to point out that all TEM micrographs are two-dimensional projections of three-dimensional volumes, which is yet another reason why the thickness of the sample is one of the most important aspects to consider in TEM sample preparation. [84]

In terms of thickness, another important parameter needs to be considered: the mean free path (MFP). MFP is the average distance an electron travels in between two scattering events. The MFP is dependent on the average atomic weight of the sample and the mass thickness, as shown in Equation 2 below:

$$\lambda' = \frac{A}{N_0 \sigma_{atom} \rho} \qquad \text{Equation 2}$$

where A is the average atomic weight of the scattering atoms, $N_0$is the Avogadro's number and $\sigma_{atom}\rho$ is the mass thickness of the sample. MFP is a measurement of distance and is expressed per unit area. Therefore, this easy calculation allows one to predict the ideal thickness of a sample in order to work at the single scattering regime. This ideal thickness is usually in the order of tens of nanometres. [83]

To fully understand why it is important to work at the single scattering regime, it is necessary to initially define electron scattering. Figure 9 shows a schematic representation of the two distinct types of electron scattering: elastic and inelastic. An incoming electron that interacts with a single atom and deviates its trajectory without losing energy is elastically scattered. Conversely, an incoming electron that interacts with an atom and loses energy is inelastically scattered. The elastically scattered electrons provide information on the crystal structure of the materials, through the dark field (DF) images and the diffraction patterns (DP), as well as on local compositional variations, through the annular dark field (ADF) and high-angle annular dark field (HAADF) images. Conversely, the inelastically scattered electrons provide information on the chemical composition of the sample, through the energy-loss spectroscopy (EELS) and X-ray spectroscopy (EDS). Combining EELS or EDS with scanning transmission electron microscopy (STEM) allows the spatial resolution of each element within the imaged area.

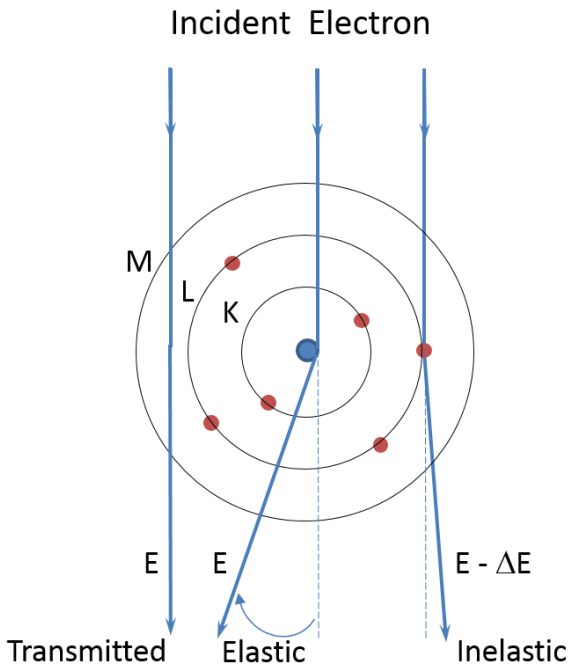

Figure 9 -Schematic representation of the electron interaction with a single atom. The incident electron might be either transmitted, elastically scattered or inelastically scattered.

Even though there are a number of TEM techniques available, only three basic operation modes are enough to collect and manipulate all the secondary signals of interest: TEM, diffraction and STEM modes. Figure 10 shows a schematic representation of the TEM (left) and diffraction (right) modes. TEM mode provides BF and DF images; while diffraction mode provides only the DPs. STEM mode may provide both BF images and DPs, as well as ADF and HAADF images. Finally, EELS and EDS may be performed in either one of the operating modes.

In TEM and diffraction modes (Figure 10), the illumination system, is set up to provide a parallel beam that evenly and constantly illuminates the whole area of interest. Conversely, in STEM mode the specimen illumination occurs by means of a convergent beam, which forms a small probe that is scanned through the area of interest, reducing beam damage and improving mass thickness contrast and spatial resolution. After sample interaction, at the objective lens, the electron beam is divergent in STEM mode, while in TEM and diffraction modes, the incoming beam from the objective lens to the imaging system is parallel. In TEM mode, it is of interest that, at the detectors, the image plane of the projective lens is the image plane of the objective lens (i.e. image of the sample in real space). Conversely, in the diffraction mode, it is of interest that the image plane of the projective lens be the back focal plane (BFP) of the objective lens (i.e. image of the sample in reciprocal space).

In practice, the distinction between TEM and diffraction modes relies solely on the strength of the intermediary lenses, while in STEM mode, due to the diverging beam, distinct

detectors need to be used. In all cases, when the image plane is presented to the detector, the real space is being investigated (BF, DF, HAADF and ADF) and when the BFP is presented to the detector, it is the reciprocal space that is under investigation (DP). Reciprocal space is described in reciprocal units of length (e.g. nm^{-1}) and displays frequency and periodicity, instead of actual length and mass thickness contrast. Periodic atomic planes, given by a definite crystal structure, are converted into a spot or a halo, whose distance from the direct beam is the reciprocal length of the distance in between crystalline planes. Therefore, electron diffraction is a very useful tool for the crystallographic characterization of materials, since it allows a two-dimensional visualization of the atomic arrangement inside the crystal lattices (in real space).

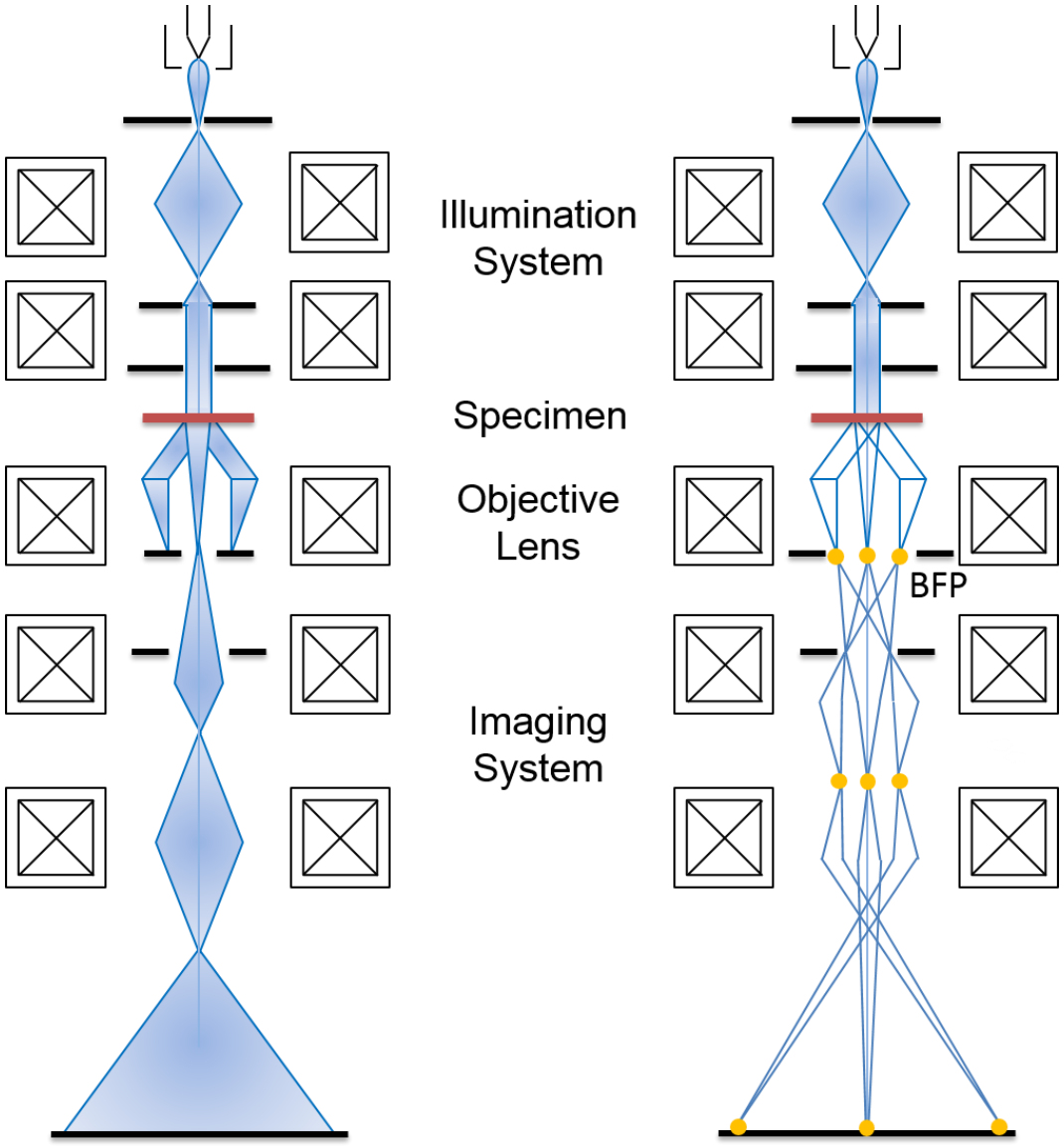

Figure 10 - Distinct operation modes of a transmission electron microscope: Imaging TEM mode (left) and diffraction mode (right).

It is important to point out that imaging the reciprocal space in the TEM allowed the development of various electron diffraction techniques. However, these only apply to highly crystalline materials. Electron diffraction works on the basis of X-ray diffraction principles (see section 1.4), with the advantage of a stronger scattering and therefore allows the crystallographic determination of single crystals and nanoparticles. Finally, it is important to remember that diffraction is a wave-like characteristic of elastically scattered electrons. The particle-like behaviour of elastically scattered electrons is important in STEM mode, since it is responsible for the ADF and HAADF images.

In inelastic scattering, X-rays and electrons also provide analogous information: the chemical composition. This information is provided by the excitation of inner-shell electrons of the sample to higher energy levels, which occurs by means of energy lost by the incoming electrons hitting the sample. The energy change of the incoming electrons (EELS) as well as the X-ray energy (EDS), are element-specific, allowing qualitative and quantitative compositional analysis [85]. EDS makes use of silicon-based X-ray detectors to identify the energy of characteristic X-rays. Conversely, EELS makes use of a spectrometer to separate the direct beam electrons according to their kinetic energy (by using magnetic prisms) and of CCD cameras (the same ones used for imaging) to perform electron counting as a function of their kinetic energy. On the one hand, EELS has the advantage of a high-count rate that allows better signal-to-noise ratio. On the other hand, EDS has the advantage of showing peaks instead of edges, which makes quantification much more straightforward. In fact, EDS is much more user friendly than EELS and, therefore, it is the preferred technique for TEM elemental mapping, in spite of the comparative low signal-to-noise ratio and high detection limits. However, frequently Si atom detection using EDS might be tricky due to the artefacts generated by the detector's Si atoms.

Even though EELS is a highly specialized technique that requires some theoretical knowledge from the operator, it is also an extremely powerful one. EELS combines in a single spectrum, pieces of information that may be achieved from various other spectroscopic techniques (e.g. infrared, visible light and X-ray) with the additional advantage of spatial resolution, which is a TEM feature Moreover, EELS does not require external standards neither for element identification nor for atomic ratio determination. An EELS spectrum, as the one shown in Figure 11, is a one-dimensional map of the direct beam kinetic energy distribution. It is presented as the number of

electrons (i.e. scattering intensity) as a function of the energy lost. Distinct types of information are obtained in distinct regions of the spectrum.

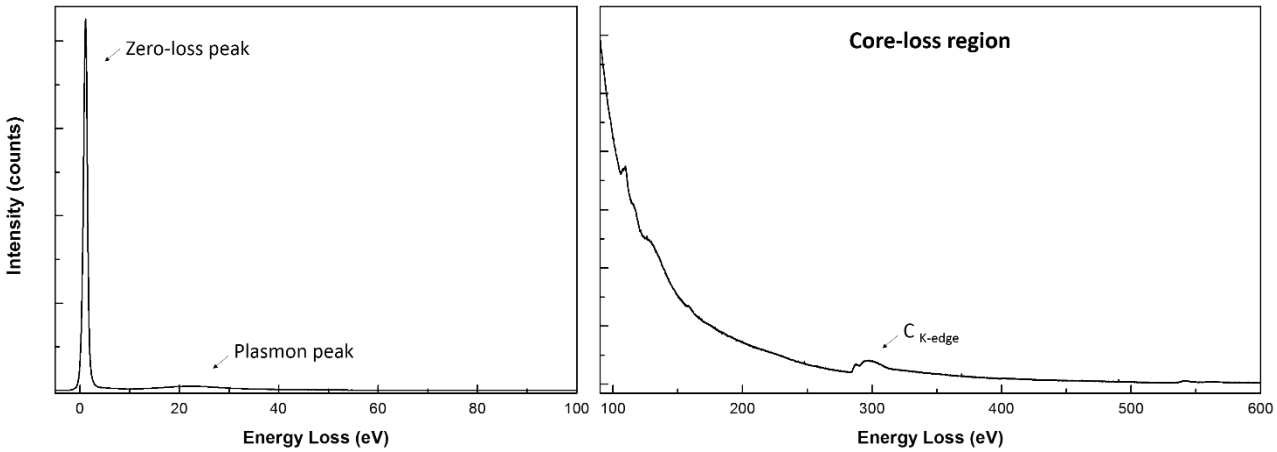

Figure 11 - Representative energy-loss spectrum highlighting the zero-loss and plasmon peaks (left), as well as an energy-loss spectrum at the core-loss region (right) with an example of an energy-loss edge.

Initially, at 0 eV, the zero-loss peak reflects the transmitted electrons that did not interact with the sample at all, or that lost an unappreciable amount of energy. This is the vast majority of the beam (when the sample is thin enough). The zero-loss peak is used for energy-loss calibration (x axis). Moreover, the full width at half maximum (FWHM) of the zero-loss peak is the measurement of the energy resolution (which is highly affected by sample thickness and microscope alignment). Currently, energy resolution in EELS is typically in the 0.8 to 1 eV range.

In the region of 4 – 40 eV plasmon peaks are observed. Plasma resonance (that produces plasmons) is a cooperative effect that occurs in both crystalline and amorphous materials. Plasma resonance is the rapid and collective excitation effect in which a longitudinal wave oscillates the free electrons present in the valence bands. Plasmon analysis is useful for calculating the sample thickness and MFP of the sample, allowing one to determine the quality of the spectrum for quantitative analysis. Moreover, the investigation of the plasmon peak as a function of time provides invaluable information concerning beam damage [86] and there is a wide variety of information that can also be obtained from the plasmon peaks, since peak position is composition sensitive and the shape is mass thickness sensitive. However, due to the plasmon peak fine structure complexity, it is frequently overlooked.

The actual compositional information of an EELS spectrum, the core-loss edges, may be found in the region above 50 eV. The excitation of a core electron (from the atom's inner shell) generates a characteristic energy-loss in the accelerated incoming electron that is equal to (or higher

than) the element binding energy. As a consequence, EELS spectra show edges rather than peaks. At the beginning of an energy-loss edge, a sharp and discrete intensity rise is verified, due to the ionization threshold, and is followed by a gradual intensity decay. The ionization threshold is at approximately the binding energy of the atom and the gradual decay is due to accelerated electrons that loose more than the binding energy or participate in more than one scattering event. Multiple scattering (produced by samples thicker than the MFP) will generate artefacts in the energy-loss spectra, since the overall energy-loss of a single atom will be the summing up of various scattering events. This is the reason why it is so important to work at a single scattering regime (as mentioned earlier). On the one hand, multiple scattering makes it difficult to perform quantitative EELS analysis, since deconvolution of a curve with a logarithmic background is needed. On the other hand, it may provide information on the chemical environment of the element of interest. Nevertheless, since it distorts the overall shape of the spectra, multiple scattering is generally undesirable. The logarithmic background observed in the EELS spectra (see Figure 11) is the main reason why EELS quantification of heavier elements is often difficult. The heavier the element, the higher is the energy-loss edge and, therefore the less intense is the signal. [87]

This brief overview of the transmission electron microscopy operation and capabilities is intended to highlight how powerful this technique is to the characterization of nanosized objects and domains. TEM is usually overlooked in polymer science and biomaterial science due to small sampling area; extensive sample preparation; intensive machine-operator interaction as well as low mass thickness contrast. Moreover, for soft materials such as polymers, beam damage due to radiolysis (chemical bond cleavage due to the incoming accelerated electrons) and heating are usually significant. Nevertheless, advances in sample preparation and TEM techniques are now overcoming most of these issues (except for the intensive machine-operator interaction). There is no doubt that EELS is the most reliable tool for investigating the chemical composition of polymeric materials and their composites. Moreover, the need for acquiring extensive knowledge on the nanostructure and chemical composition of multicomponent and polymeric systems is irrefutable. In this work, TEM and EELS were used to thoroughly investigate silicon distribution within the O-I hybrid nanocomposites developed herein, providing previously unreported information which was essential to the correct interpretation of X-ray scattering results.

1.4. X-RAY SCATTERING TECHNIQUES

In materials science, X-ray scattering techniques are the most widely used for investigating the internal structure of materials at both the atomic and the nanometric length scales. X-ray is an electromagnetic radiation in the 0.01 to 10 nm wavelength range that may be generated in two distinct forms. As already described in subchapter 1.3, an accelerated electron beam hitting a target ejects electrons from the inner shell of the atoms. As a consequence, an electronic reconfiguration occurs, which de-excites some electrons back to the atom inner-shell, resulting in characteristic X-rays. This is the X-ray generation mechanism used laboratory equipment. Through this mechanism, X-rays are mostly generated in the wavelength characteristic of the metallic target, which is usually the 0.154 nm Cu Kα wavelength. [88]

Conversely, in synchrotron machines a continuous X-ray wavelength spectrum is obtained. A synchrotron machine is a large-scale facility in which electrons (or positrons) are accelerated up to almost the speed of light and then injected into a storage ring, as shown schematically in Figure 12. At the storage ring, the accelerated electrons move around in discrete bunches which are forced by bending magnets and/or insertion devices, such as wigglers or undulators, to undergo a curved trajectory. Deviation from the linear trajectory into a circular one causes electron deceleration, producing high brilliance X-rays that propagate tangent to the storage ring, with an energy proportional to the forth power of electron speed and inversely proportional to the trajectory squared radius. Synchrotron sources have the advantage of providing a pulsed radiation with high brilliance (i.e. large flux in small areas). However, they also have the disadvantages of elevated cost and low availability, since there are only few synchrotron facilities available around the world. [89]

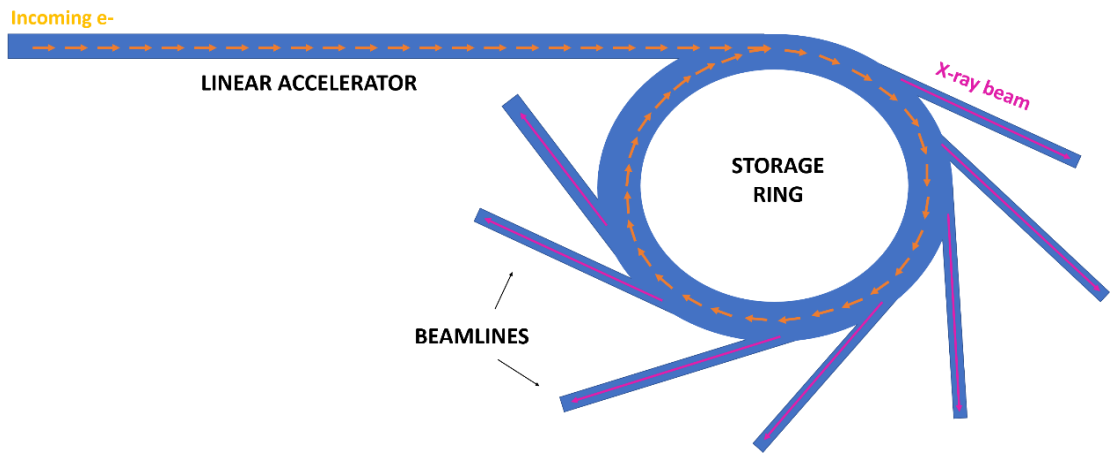

Figure 12 - Schematic representation of the synchrotron radiation generation process.

In scattering experiments, synchrotron facilities provide the advantages of increased resolution and small acquisition times, which allows a large variety of time-resolved and *in situ* measurements to be performed. One of the main advantages of X-ray scattering techniques over the electron microscopy techniques is that it requires very little sample preparation and almost any kind of sample (e.g. liquid, gases, gels, solids) might be investigated. Moreover, scattering patterns carry out structural information of all the illuminated area, which is in the order of squared millimetres. In contrast with the few squared nanometres observed by TEM, X-ray scattering techniques are much more representative of the overall sample behaviour.

In many aspects, X-rays interact with matter in a manner analogous to the electrons. If on the one hand, electrons are more strongly scattered than X-rays, on the other hand, X-ray interacts with matter through both absorption and scattering processes [83]. As consequence, in X-ray scattering techniques that operate in the transmission mode, such as the small-angle (SAXS) and the wide-angle (WAXS) X-ray scattering, usually thicker samples are preferred. Scattering experiments are performed in the reciprocal space, which means that the scattering-angle exhibit a reciprocal relationship with the real space lengths [90]. As a consequence, the larger the scattering-angle, the smaller the length-scale of the structural information achieved. Therefore, SAXS aims to investigating electron density variations at the nanometric length-scale, through the analysis of information obtained at low angles (< 5°), while WAXS aims to determining crystallographic parameters through the analysis of scattering angles larger than 5°.

The basic geometry of a SAXS/WAXS experiment is shown in Figure 13. The SAXS/WAXS set up consists of a source (i.e. synchrotron facility, Figure 12), a monochromator (to select the energy), a collimation system, the sample environment and the detectors. The collimation system comprises a pair of apertures: the defining aperture is placed close to the monochromator and defines the beam size, while the guard aperture is placed close to the sample and provides an incoming parallel beam reaching the sample. From the source to the guard aperture, X-rays are always travelling in vacuum, in order to maintain the incoming beam intensity. Analogously, from the sample environment to the detector, X-rays are also travelling in vacuum, in order to keep the background to a minimum. However, most samples used in SAXS experiments (i.e. solution or soft matter) cannot handle vacuum and, for this reason, usually the sample environment itself is under ambient conditions. [88,90]

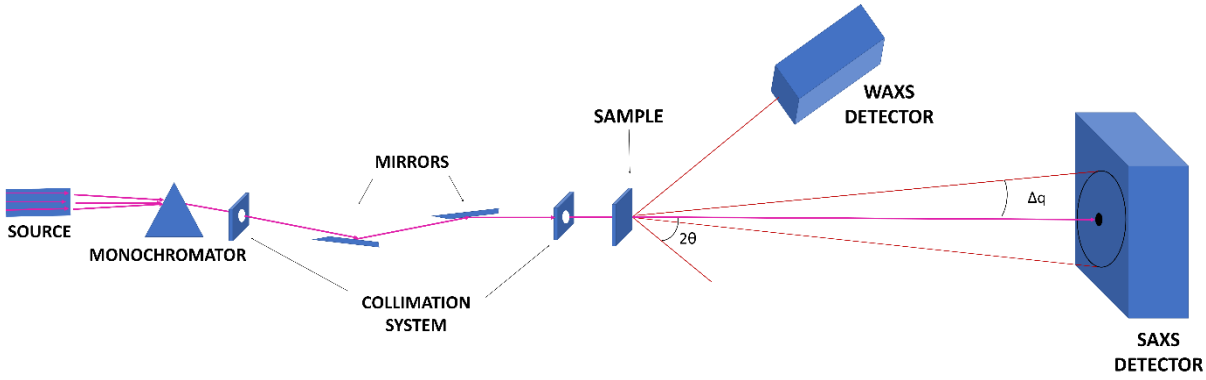

Figure 13 - Schematic demonstration of a small-angle X-ray scattering beamline set up, with an additional WAXS detector.

In both SAXS and WAXS, the incoming X-ray beam hits a sample surface perpendicularly and the resulting scattering patterns are collected from the opposite surface. Due to the small-angles used in SAXS experiments, SAXS detectors are usually placed at a sample-to detector distance larger than 1 m. Conversely, WAXS detectors are placed at sample-to-detector distances in the order of a few hundred millimetres. SAXS detectors are always parallel to the sample surface and WAXS detectors might be either parallel to the sample plane or at an angle. Usually, WAXS detectors are placed and above the SAXS detector tube at an angle, to allow simultaneous SAXS/WAXS experiments. Time-resolved and temperature-dependent simultaneous SAXS/WAXS experiments are now routine in the SAXS beamlines [91,92]. These experiments are of great interest to the polymer science, since it allows to investigate the kinetics of polymer melting and crystallization [93].

The ideal thickness of a sample in SAXS and WAXS experiments is a compromise between increasing scattering intensity and decreasing attenuation. Usually, it lies around a few millimetres. Attenuation is an absorption effect that results in the outgoing X-ray beam exiting the sample being the same wavelength of the incoming beam, however with a smaller intensity. X-ray scattering occurs when an X-ray photon hits an electron of the sample and deviates. If during this process the photon loses energy to the electron, the Compton scattering occurs. Compton scattering is incoherent and does not carry out structural information, since it is out of phase with the outgoing unscattered beam. Conversely, if the X-ray photon preserves its energy, Thomson scattering, occurs. Thomson scattering provokes electrons to oscillate at their frequency, producing secondary spherical waves in the same wavelength as the outgoing unscattered beam.

In Thompson scattering, not only the wavelength of the incoming radiation is preserved, but also all the secondary waves show the same amplitude. Therefore, the scattering patterns generated are formed by the constructive and destructive interference between the scattered

spherical waves, as well as between the unscattered plane wave and the scattered spherical waves. As a result, in SAXS, it is the electronic density difference, Δρ, rather than each phase absolute electronic density, ρ, that produces the observable scattering patterns. Scattering patterns are recorded in two-dimensions by the detectors. However, usually SAXS results are presented in one-dimensional intensity versus scattering-angle curves. Some examples are shown in Figure 14.

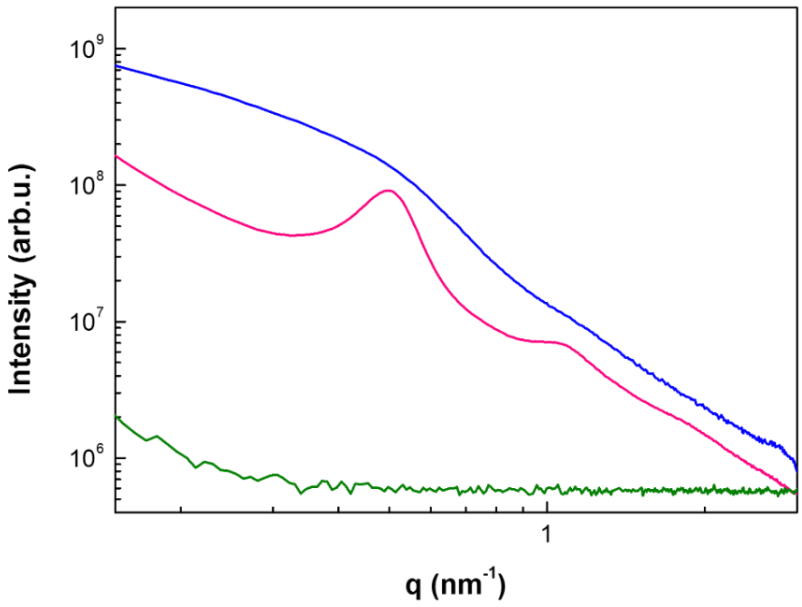

Figure 14 - One-dimensional SAXS curves showing a scattering curve in which the form factor is dominant (blue), a scattering curve in which the structure factor is dominant (pink) as well as an example of background scattering (green).

One-dimensional curves enable the qualitative and quantitative translation of the reciprocal information into a real space structure [94]. However, the interpretation of SAXS results is model-dependent, which means that it is necessary to have some prior knowledge on the sample, in order to interpret the data. The most important information one should know beforehand are the scattering objects form and concentration within the sample, as well as the number of phases present within the sample. Scattering objects are the structures responsible for the observable features at the scattering curves.

If we consider biphasic systems, such as a nanoparticle dispersion or a porous membrane, in which the nanoparticles and the membrane matrix share the same composition, the scattering objects would be the nanoparticles on the prior and the pores on the latter. This is due to the fact that, in SAXS, contrast is given by the squared electronic density differences, $\Delta\rho^2$:

$$\Delta\rho^2 = (\rho_s - \rho_b)^2 \qquad \text{Equation 3}$$

where ρ_s is the electronic density of scattering objects (i.e. nanoparticles or pores), and ρ_b is the electronic density of the matrix (i.e. solvent or the membrane matrix).

In SAXS, the scattering intensity relates to the scattering objects' form and concentration through the following:

$$I(q) = N.\langle I_0.(\Delta\rho)^2.V^2.P(q)\rangle.\langle S(q)\rangle \qquad \text{Equation 4}$$

where N is the number of scattering objects within the analysed area, I_0 is the intensity of the incoming X-ray beam, V^2 is the volume of a single scattering object, P(q) is the form factor and S(q) is the structure factor.

In diluted systems, S(q) might be approximated to 1 and I(q) becomes identical to N times the scattering of a single particle. The S(q) approximation is valid in diluted systems based on the assumption that particles do not interact with each other. In this case (diluted and biphasic), all factors within Equation 4 are constant except for P(q). The form factor, P(q), describes the scattering intensity of a single scattering object as a function of the scattering angle. Therefore, through the investigation of P(q) in diluted systems (Figure 14, blue curve), the form of the scattering objects (e.g. spheres, cylinders and others) might be determined.

Conversely, when the concentration of the scattering objects increases, the distance in between objects approximates to the size of the object itself. As a consequence, the approximation of the structure factor, S(q), is no longer valid and S(q) becomes the dominant factor in Equation 4. In concentrated systems S(q) usually results in a peak in a q-value corresponding to the average distance in between scattering objects (Figure 14, pink curve), Therefore, investigating S(q) in concentrated systems allows to determine the ordering of the scattering objects within the sample into, for example, lamellar, cubic or hexagonal superstructures.

When the sample of interest is not biphasic, usually P(q) and S(q) become too complex to be determined. In these cases, the invariant, Q is a measurement of the scattering power of the sample and does not depend on any assumption concerning the number of phases or the scattering object´s form or structuring [90]. Q is given by:

$$Q = \frac{1}{2\pi^2}\int_0^\infty I(q)q^2dq = 2\pi^2\sum_{i\neq j}\phi_i\phi_j\left(\rho_i-\rho_j\right)^2 \qquad \text{Equation 5}$$

where ϕ_i and ρ_i are, respectively, the volume fractions and electronic densities of each phase. Graphically, Q may be achieved by integrating the SAXS curves in an $I(q)q^2$ vs q plot. For multiphasic systems, the analysis of the invariant, based on the previous knowledge of each component's

volume fraction, may provide information concerning phase miscibility and interaction. However, it is noteworthy to mention scattering intensity provided by the detectors are in arbitrary units, or counts, which is a relative scale. If only structural information is intended, relative intensities are enough to investigate Q. However, if quantitative information concerning the scattering power of the sample, such as the M_w of a polymer, is intended, it is essential to calibrate the scattering intensity by the incoming beam's flux density and the illuminated sample volume.

In concentrated systems, the analysis of the peaks generated by the interaction between particles (see Figure 14, pink curve) may also be performed by means of Bragg's law, provided that the Bragg condition is attained. Bragg condition states that the incoming X-ray beam is scattered in a specular fashion by the periodically spaced planes of scattering objects (or atoms), resulting in a constructive interference that is shown as peaks in the scattering curves. In crystallography, Bragg´s law is given by:

$$2d_{Bragg}\sin(\theta_{hkl}) = n\lambda \qquad \text{Equation 6}$$

where n is the order of reflection, λ is the radiation wavelength, θ_{hkl} is the scattering semi-angle attributed to the (h k l) plane, and d_{Bragg} is the distance between two subsequent planes of the scattering objects (or atoms) in that orientation. In addition, the average grain size or long-range ordering in a specific crystalline orientation may be also estimated by the means of Scherer's equation:

$$D_{hkl} = \frac{K\lambda}{\beta cos(\theta_{hkl})} \qquad \text{Equation 7}$$

in which K is the shape factor accounting for the crystal habit (usually 0.91) and β is the peak full-width at half-maximum (FWHM). D_{hkl} must be calculated in all directions to estimate the average crystallite size in all directions.

The scattering angle (X-axis) may be either shown in the form of 2θ (see Figure 13), which is useful in WAXS measurements due to the direct 2θ relationship with the d-spacing (d_{Bragg}), or in the form of the scattering vector, q, which is given by:

$$q = \frac{4\pi}{\lambda}\sin(\theta) \qquad \text{Equation 8}$$

where λ is the radiation wavelength. The fact that the q vector takes into consideration both the scattering angle and the radiation wavelength allow the scattering curves to be comparable, irrespective of the radiation source.

From the q vector in concentrated systems with a structure-related peaks, the correlation distance (d_s) between scattering objects in terms of the scattering vector might be attained by combining Equation 6 and Equation 8:

$$d_s = {}^{2\pi}/_{q_{max}} \qquad \text{Equation 9}$$

where q_{max} is the maximum of the Bragg peak at the small-angle region. Analogously, the long-range ordering, L_c, may be achieved by converting Equation 7 in terms of q (Equation 8) [95]:

$$L_C = {}^{4\pi}/_{\Delta q} \qquad \text{Equation 10}$$

where Δq is the FWHM of the SAXS peak. It is noteworthy to mention that both d_s and L_c usually do not carry directional information since, conventionally, q is integrated in all directions[94].

L_c is a measurement of the extent at which the d_s correlation holds, or else, a measurement of the long-range ordering of the scattering objects. Figure 15 shows schematically the physical meaning of the d_s and L_c parameters based on an orderly arrangement of particles. If, on the one hand, d_s and L_c are valuable information that may be achieved irrespective of prior knowledge on the scattering objects' shape or specific arrangement. On the other hand, the scattering objects' dimensions, such as radius, cannot be achieved without making some assumptions. For example, if the scattering objects may be described as compact spheres in a concentrated system, the knowledge of their volume fraction ϕ and their correlation distance d_s may be used to calculate particle radius, R_s, from the following expression [96]:

$$R_s = \left({}^{3\phi}/_{8\pi}\right)^{1/3}\left({}^{d_s}/_{2}\right) \qquad \text{Equation 11}$$

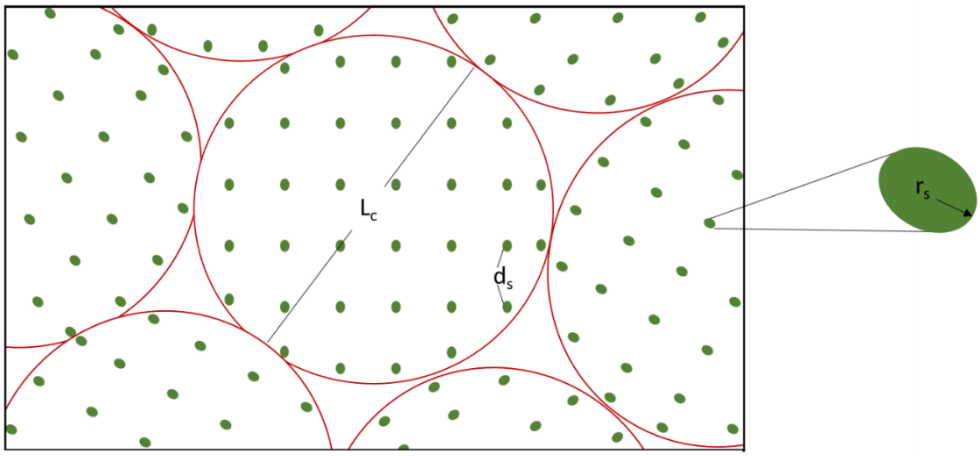

Figure 15 - Schematic representation of the L_c, d_s and R_s parameters within the superstructure formed by ordered scattering objects.

1.4.1. X-RAY SCATTERING OF POLYMERIC SYSTEMS

A semicrystalline polymer usually presents itself in a spherulitic morphology, such as the one shown in Figure 16, which is constituted of fibrils. Spherulite diameters are in the order of tens to hundreds of micrometres, while fibril thicknesses are in the order of hundreds of nanometres. Fibrils are made up of a lamellar arrangement of amorphous polymer and crystalline polymer, which is in the order of tens of nanometres and may be observed at the SAXS q-range. Conversely, on the WAXS q-range, the crystal lattice within the crystalline phase may also be investigated. [97]

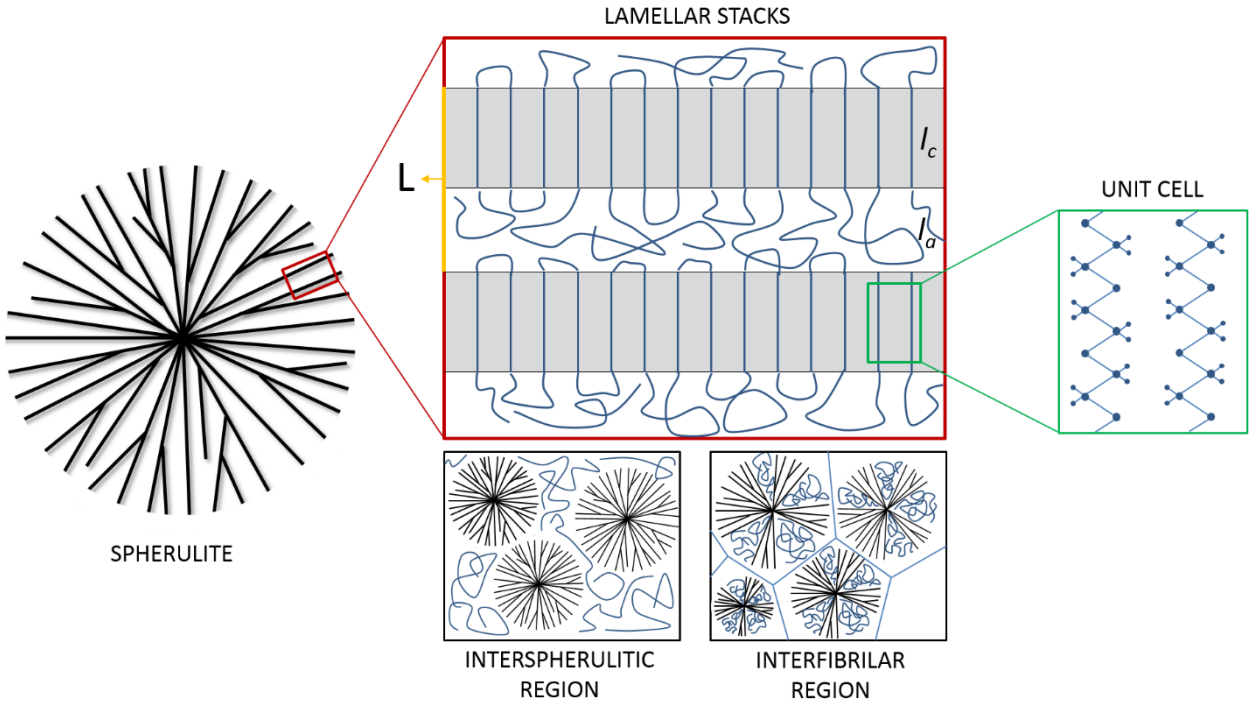

Figure 16 - Schematic representation of a semicrystalline polymer morphology, in which the physical meaning of the structural parameters L, l_a and L_c, obtained by SAXS, are indicated.

The typical three-dimensional spherical morphology of the spherulite superstructure turns the SAXS two-dimensional scattering pattern of a semicrystalline polymer to be isotropic, while the periodic lamellar stacks within the fibrils produce the characteristic Bragg peaks shown in their one-dimensional SAXS curves (see Figure 14, pink curve). Moreover, the existence of amorphous polymer in between lamellar polymer crystals, as well as in the interfibrillar and interspherulitic regions is the reason for their inherent electron density spatial inhomogeneities. As a result, at larger scattering angles polymeric systems show a constant scattering intensity increase, as shown in Figure 17. [91,93,98]

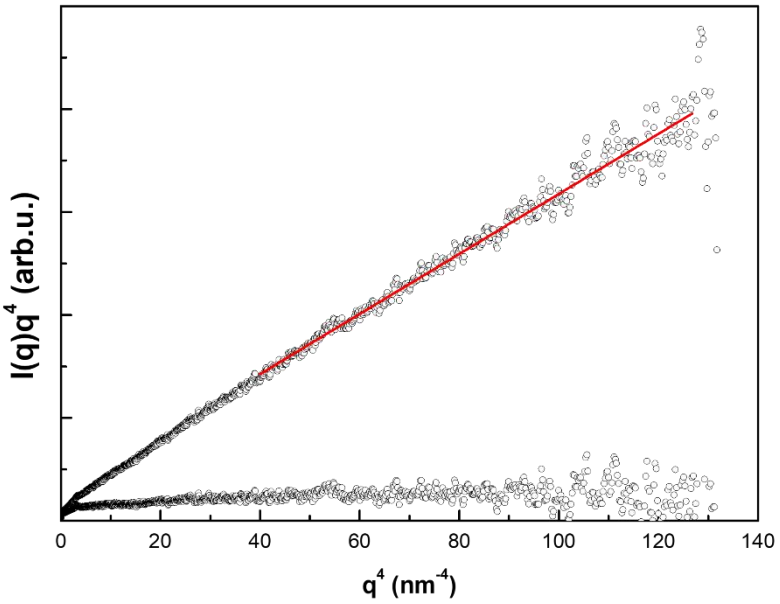

Figure 17 – Graphical approximation of a generic semicrystalline polymer scattering to the scattering of a biphasic systems by means of the background, I_b, subtraction. I_b is the slope of the linear fit (red line).

Scattering intensity increase correction allows the approximation of the scattering of a semicrystalline polymer with the scattering of an ideal biphasic system. It may be performed by linear fitting the qL>>1 region of an Iq^4 vs q^4 plot (Figure 17), resulting in the linear equation below:

$$I(q)q^4 = K_p + I_b q^4 \qquad \text{Equation 12}$$

in which K_p is the Porod´s constant and I_b is the background [90]. Afterwards, I_b is subtracted from the scattering intensity.

From the corrected SAXS curves, the structural parameters of the periodic lamellar structure, such as the long period, L, the thickness of the crystalline lamellae, l_c, and the amorphous interlamelar spacing, l_a, as well as the linear degree of crystallinity, X_{SAXS}, may be obtained. The long period, L, as shown schematically in Figure 16, is analogous to d_s, and corresponds to the periodic spacing in between two adjacent crystalline lamellae. This also means to say that L is the addition of the thickness of a single crystalline lamella (l_c) with the thickness of a single amorphous interlamellar spacing (l_a) [93]:

$$L = l_c + l_a \qquad \text{Equation 13}$$

To obtain these structural parameters, a Fourier transform of the scattering intensity, may be performed by using the following equation [99]:

$$\gamma_1(r) = \frac{1}{Q_i}\int_0^\infty [I(q) - I_b]q^2 \cos(qr)\, dq \qquad \text{Equation 14}$$

where Q_i is the ideal invariant, which gives the scattering power of the ideal biphasic polymer. In order to graphically apply Equation 14, K_p is used to extrapolate the experimental SAXS curve to infinity while the Guinier's law applied to a ln(I(q)) versus q^2 plot, is used to extrapolate the experimental SAXS curves to q = 0, by means of a_0 [100]. Guinier´s law is given by:

$$ln\big(I(q)\big) = \ln(a_0) - \frac{R_g^2 q^2}{3} \qquad \text{Equation 15}$$

where the linear coefficient, $\ln(a_0)$, provides the scattering intensity at q = 0 and the angular coefficient, $-R_g^2/3$, gives the gyration radius of the scattering objects, irrespective of their shape. It is important to point out that Guinier's law only applies when $0 < qR_g < 1$.

As a result, Equation 14 provides a one-dimensional correlation function, such as the one shown in Figure 18, as a function of distance (r). In an ideal biphasic system, crystalline and amorphous regions show a sharp interface. Moreover, all the crystalline lamellae and amorphous interlamellar spacings are of the same size. However, in real semicrystalline polymers, the interface in between amorphous and crystalline phases within the lamellar arrangement are diffuse. Moreover, the lamellar thicknesses vary within a certain range. As a consequence, the overall correlation function becomes curved, as it is clearly shown in Figure 18.

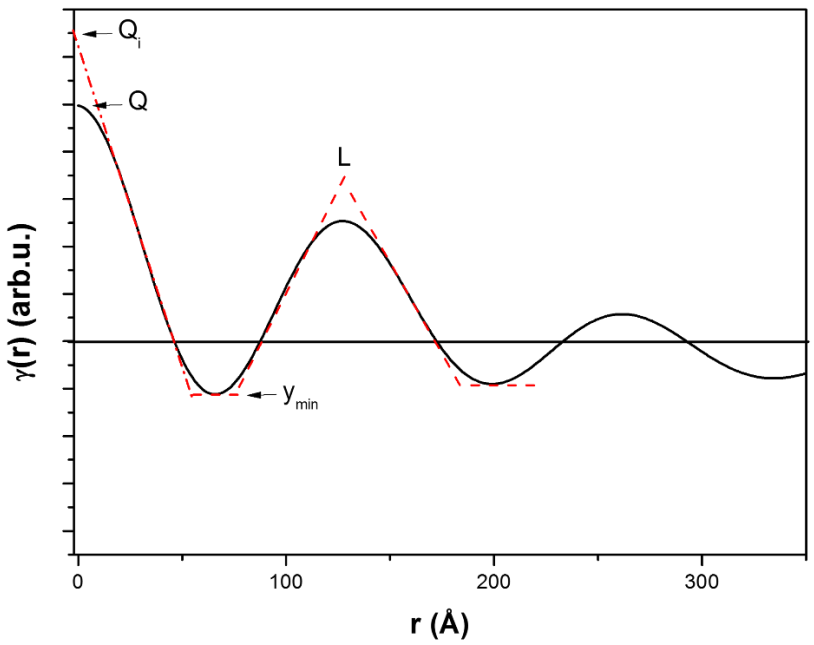

Figure 18 – Generic one-dimensional correlation function, obtained by means of Equation 14, of SAXS curve extrapolated to zero and infinity of a semicrystalline polymer. Red dashed line indicates the behaviour of an ideal biphasic system. Adapted from Rabiej et al. [98]

By means of the self-correlation triangle theory [101], all structural parameters may be achieved from the correlation function [102]. Initially, L is taken as the first maximum of the correlation function. Then, the first phase thickness is determined from the following relation:

$$l_x = \frac{y_{min} - Q_i}{B} \qquad \text{Equation 16}$$

in which y_{min} is the first minimum of the correlation function and B is the angular coefficient of the linear portion of the $0 < y < y_{min}$ region (see Figure 18). The linear coefficient of this same region gives Q_i.

It is noteworthy to mention that, due to the fact that SAXS scattering is provided by an electronic density difference l_x might be either l_c or l_a. If, for instance, l_a is obtained from Equation 16, l_c is obtained by the difference between L and l_a. In order to determine whether l_x is attributed to the crystalline or amorphous lamellae the bulk degree of crystallinity must be considered [103]. Ideally, the bulk degree of crystallinity is a volumetric measurement of the crystalline fraction within a semicrystalline material. However, experimentally the mass degree of crystallinity is typically provided in mass fraction and the density correction may frequently be overlooked. Mass degree of crystallinity may be obtained from WAXS, from the following equation[104]:

$$\chi_{WAXS} = \frac{A_c}{(A_c + A_A)} \qquad \text{Equation 17}$$

where A_c is the total area of all crystalline peaks and A_a is the total area of the amorphous halo.

If, on the one hand, χ_{WAXS}, is a measurement of the amount of crystals within the sample, X_{SAXS} is a geometric measurement of the amount of crystals within the lamellar arrangement. Therefore, X_{SAXS} is usually higher than χ_{WAXS}, due to the interfibrilar and interspherulitic amorphous polymer occurrence, which are accounted for in χ_{WAXS}. X_{SAXS} be described as:

$$X_{SAXS} = \frac{l_c}{L} \qquad \text{Equation 18}$$

Finally, it is important to point out that in multiphasic systems such as blends and copolymers, frequently the approximation to a biphasic model is not valid[99]. However, literature has already shown that due to polymers' low contrast, associated with their similar crystalline parameters (see section 1.1), in fact, this is not a bad approximation for PCL and PEG systems[30,46,105]. In this work, the invariant analysis was used to determine the number of phases present at the amorphous and ternary O-I hybrid nanocomposites, as well as to investigate the temperature effect

on the overall scattering power of the sample. In addition, the one-dimensional correlation function was used to determine and monitor the evolution of the structural parameters of the crystalline phases during temperature-dependent simultaneous SAXS/WAXS experiments.

2

AIMS & GOALS

Laura Caetano Escobar da Silva
INSTITUTE OF CHEMISTRY

2. AIMS AND GOALS

The present thesis consists of a thorough investigation of the morphology and nanostructure of atoxic and biocompatible organic-inorganic hybrid nanocomposites, with useful properties for the biomedical field, which are made up of bicomponent matrices containing both poly(ε-caprolactone) (PCL) and poly(ethylene glycol) (PEG). Therefore, the aim of this work was to understand, through the use of advanced characterization techniques, i.e. Transmission Electron Microscopy (TEM) and Synchrotron X-ray Scattering (SAXS/WAXS), how phenomena such as phase separation and/or crystallization affect the organic-inorganic hybrid nanocomposites' morphology and nanostructure.

Organic-inorganic hybrid nanocomposites made up of PCL and PEG, which were cross-linked by *in situ* generated silsesquioxane structures, were chosen as a model system due to their acknowledged biomedical potential as well as their ability to produce macroscopically uniform devices in spite of their multiphase structure at the nanometre length scale. In order to reach this major goal, a set of specific objectives was outlined:

a. To prepare organic-inorganic hybrid nanocomposites through an atoxic and solvent-free route by using (3-isocianatopropyl) triethoxysilane (IPTES), as the inorganic moiety prepolymer, and PCL/PEG, as the organic moiety prepolymers, at distinct weight ratio.

b. To propose a model nanostructure to explain the nanocomposites' morphology by the combination of electron microscopy and X-ray scattering techniques.

c. To investigate the effect of increasing the organic prepolymers' molecular weight in the O-I hybrids' nanostructure by means of structural analyses such as nuclear magnetic resonance, infrared spectroscopy and DSC.

d. To investigate the thermal behaviour of O-I hybrid nanocomposites by using temperature-dependent and time-resolved simultaneous SAXS/WAXS.

3

EXPERIMENTAL

Laura Caetano Escobar da Silva
INSTITUTE OF CHEMISTRY

3. EXPERIMENTAL SECTION

3.1. MATERIALS

All reagents were supplied either by Sigma Aldrich (New York, USA) or LabSynth (São Paulo, Brazil) and used as received, unless otherwise specified.

Sigma Aldrich supplied:

- Poly(ε-caprolactone) diol (PCL) with M_w 530 g mol^{-1} - low M_w PCL prepolymer;
- Poly(ε-caprolactone) diol (PCL) with M_w 2 000 g mol^{-1} - high M_w PCL prepolymer;
- (3-isocianatopropyl) triethoxysilane (IPTES), 247.36 g mol^{-1} - cross-linking agent;
- Poly(ethylene glycol) (PEG) with M_w 1 500 g mol^{-1} - high M_w PEG prepolymer.

LabSynth supplied:

- PEG with M_w 400 g mol^{-1} - low M_w PEG prepolymer;
- Nitric acid (HNO_3) – catalyst;
- Tetrahydrofuran (THF) – solvent for Soxhlet extraction.

3.2. METHODS

3.2.1. SOLVENT-FREE SYNTHESIS OF O-I HYBRID NANOCOMPOSITES

Initially, the organic (PCL or PEG) prepolymer was molten dried under vacuum for 12 hours at 60 °C and purged with argon for 30 min prior to use. (3-isocianatopropyl) triethoxysilane (IPTES) was added to the molten polymer, in a 2:1 (IPTES : Polymer) molar ratio to obtain PCL-IPTES or PEG-IPTES, which are the modified organic prepolymers containing triethoxysilyl groups at the chain ends. The reaction was kept under argon atmosphere and vigorous stirring at 70 °C for approximately 8 hours.

Afterwards, known masses of PCL-IPTES and PEG-IPTES were mixed at 40 °C in order to produce the ternary O-I hybrid nanocomposites. Silsesquioxane structures were obtained by the triethoxysilyl group hydrolysis, which was nitric acid catalysed, through the addition of a 1% aqueous solution in a 1:6 (Polymer-IPTES : HNO_3) molar ratio. Hydrolysis was spontaneously followed by silanol condensation. Therefore, after a viscosity increase was observed, the mixture was placed in a PTFE dish and heated at 90 °C for 2 hours to allow cross-linking to proceed. Table 1 shows the mass composition of the reaction media used to produce each one of the chemically cross-linked O-I hybrid nanocomposites. Binary nanocomposites were also synthesized as a comparison. In Table 1, and throughout the text, indexes denote the reagents' weight ratio at the reaction media. Amorphous samples were made up of the low M_w (PCL and/or PEG) prepolymers and were seen to be flexible and transparent self-standing films. Semicrystalline samples were made up of the high M_w (PCL and/or PEG) prepolymers (see section 3.1) and were seen to be opaque and flexible self-standing films.

Table 1 - Mass composition of the reaction media used for the synthesis of O-I hybrid nanocomposites.

	Sample	Weight ratio		
		PCL	PEG	SS
Amorphous	PEG_{45}/SS_{55}	0.00	0.45	0.55
	PCL_9-PEG_{37}/SS_{54}	0.09	0.37	0.54
	PCL_{19}-PEG_{28}/SS_{53}	0.19	0.28	0.53
	PCL_{24}-PEG_{24}/SS_{52}	0.24	0.24	0.52
	PCL_{29}-PEG_{20}/SS_{51}	0.29	0.20	0.51
	PCL_{40}-PEG_{10}/SS_{50}	0.40	0.10	0.50
	PCL_{52}/SS_{48}	0.52	0.00	0.48
Semicrystalline	PEG_{75}/SS_{25}	0.00	0.75	0.25
	PCL_{39}-PEG_{39}/SS_{22}	039	0.39	0.22
	PCL_{80}/SS_{20}	0.80	0.00	0.20

3.3. Instrumentation

3.3.1. Attenuated total reflectance infrared spectroscopy (ATR-IR)

ATR-IR spectra were obtained in a controlled environment using a Cary 630 (Agilent) spectrophotometer at a 4000 to 400 cm^{-1} wavenumber range using 64 scans and 4 cm^{-1} resolution. Liquid samples were measured by placing a drop directly on the Ge crystal. Solid samples were pressed against the Ge crystal for analyses. In between samples, Ge crystal was cleaned using ethanol.

3.3.2. Solid-state ^{29}Si Nuclear Magnetic Resonance (^{29}Si NMR)

Solid-state HPDEC MAS ^{29}Si NMR was performed in an Avance II 400 (Bruker) spectrometer, operating at 79.5 MHz for ^{29}Si nucleus and 400 MHz for ^{1}H nucleus. Samples were loaded onto a 4 mm ZrO_2 rotor as staked disks. The ZrO_2 rotor was spun at 6.1 kHz during analyses. Experiments were carried out using a 50 kHz decoupling power and a 20 s recycling delay.

3.3.3. Soxhlet Extraction (W_s)

Prior to the extraction, in order to remove any adsorbed water, samples of approximately 1 g were dried under vacuum at room temperature. Then, samples were weighed in an analytical balance, and placed in a cellulose cartridge, whose weight was also measured. The cellulose cartridge was placed into the extractor and left for 72 hours. After the extraction completion, sample and cartridge were dried again under vacuum for 24h to remove adsorbed THF. The soluble fraction was determined by weighting samples prior to and after Soxhlet extraction, using the following equation:

$$W_s(\%) = \left(\frac{(W_d - W_e)}{W_d}\right) \times 100 \qquad \text{Equation 19}$$

where W_s is the soluble fraction (expressed in percentage); W_d is the weight of the dried sample prior to extraction and W_e is the weight of the dry sample after the extraction.

3.3.4. Differential scanning calorimetry (DSC)

DSC experiments were performed in a Q2000 (TA instrument) equipment using approximately 10 mg sample disks which were placed in sealed aluminium pans. Samples were subjected to controlled heating and cooling at a rate of 5 °C min^{-1}. First heating went from room

temperature to 200 °C, cooling went from 200 to -90 °C and second heating occurred from -90 to 200 °C. 5 min isotherms were used in between.

The melting and crystallization peaks observed in the DSC curves were used to calculate the degree of crystallinity (χ_{DSC}) as follows:

$$\chi_{DSC} = \frac{\Delta H}{x_{PCL}.\Delta H^0_{PCL} + x_{PEG}.\Delta H^0_{PEG}} \qquad \text{Equation 20}$$

where ΔH is the enthalpy of the thermal event, x_{PCL} and x_{PEG} are PCL and PEG weight ratios, respectively, and ΔH^0_{PCL} (142 J g^{-1}) [106] and ΔH^0_{PEG} (188,9 J g^{-1}) [107] are attributed to the enthalpy of the 100% crystalline homopolymers (PCL and PEG respectively).

3.3.5. Helium picnometry (D_{HP})

Nanocomposite densities were obtained by helium picnometry (D_{HP}). Approximately 140 mg of pulverized samples were inserted into the "NANO" sample holder in order to fill it entirely. The sample holder was then placed inside an Ultrapic 1200e (Quantachrome) instrument, which had been previously calibrated by using commercial silica (SiO_2) as a reference.

3.3.6. Thermogravimetric analyses (TGA)

TGA thermograms were obtained in a 2950 thermobalance (TA instrument). In order to do so, approximately 10 mg disk samples were heated at a 10 °C min^{-1} heating rate, from room temperature up to 900 °C, under argon atmosphere.

3.3.7. Water uptake (*S*)

Water uptake was obtained by immersing 100 mg sections of previously dried nanocomposites in 10 mL of deionized water at 37 °C for up to 24 hours. Sections were weighed in an analytical balance prior to and after deionized water immersion. Experiments were performed in 3 to 5 specimens of each sample. Swelling percentage was calculated as follows:

$$S\ (\%) = \left(\frac{(W_w - W_d)}{W_d}\right) \times 100 \qquad \text{Equation 21}$$

where S is the degree of swelling (expressed in percentage); W_w is the weight of the wet section and W_d is the weight of the dry section.

3.3.8. Scanning electron microscopy (SEM)

Scanning electron micrographs (SEM) were taken in a Quanta 250 FEG (FEI) microscope operating at an acceleration voltage of 10 kV. In order to prevent roughness-induced artefacts and, most importantly, to enable the observation of nanosized features, cryoultramicrotomed cross-

sections were used. Cryoultramicrotomy was performed with a diamond knife (Diatome) in an EM FC6 Reichert Ultracut (Leica) cryoultramicrotome operating at -120 °C. Prior to SEM observation, the cross-sections were mounted on aluminium stubs and carbon and iridium sputter coated in a Bal-TEC MD 020 (Balzer) sputter coater.

3.3.9. Transmission electron microscopy (TEM)

Transmission electron micrographs (TEM) were taken in a JEM 1400 Plus (JEOL) microscope, operating at 120 kV (LNNano-Brazil), and equipped with a One View 4k x 4k CMOS camera (Gatan). Nanocomposites were investigated through 60 nm thick ultrathin sections, obtained by cryoultramicrotomy, which were then mounted on TEM copper grids. Digital Micrograph 4.0 software was used for image acquisition and ImageJ software was used to calculate domain size and spacing.

3.3.10. Electron energy loss spectroscopy and electron spectroscopic imaging (EELS/ ESI-TEM)

EELS and ESI-TEM experiments were performed in a Libra 120 Plus (Zeiss) transmission electron microscope, operating at 80 kV and equipped with an in-column OMEGA filter and an Olympus 2k x 2k (Cantega) CCD camera. iTEM software was used for data acquisition. To ensure that sample thickness was smaller than 0.25 times the mean free path of inelastic scattering, 45 nm ultrathin sections mounted on TEM copper grids were used.

For EELS experiments, the microscope was aligned in imaging mode. A 10 mrad objective lens aperture was used to select the area of interest and an entrance filter aperture was used to set the collection angle at 7mrad. A spectral dispersion of 125 eV was used.

For ESI-TEM imaging of the Si atom distribution, taken at the 99 eV Si $L_{2,3}$-edge, the microscope was also aligned in imaging mode and the objective lens and entrance filter apertures were also used. Moreover, a 10 eV energy slit was placed at 110 eV to select the energy.

3.3.11. Small-angle synchrotron X-ray scattering (SAXS)

Small-angle synchrotron X-ray scattering (SAXS) experiments were performed at the D01B-SAXS1 beamline located at the Brazilian Synchrotron Laboratory (LNLS-Brazil) [92]. A $\lambda = 0.1544$ nm point collimated monochromatic beam and a Pilatus 300k (Dectris) hybrid pixel X-ray detector were used. SAXS detector was placed at a sample-to-detector distance of 2995 mm, which covers the 0.8 nm^{-1} to 4 nm^{-1} q-range (see Equation 8, section 1.4). SAXS two-dimensional scattering patterns were collected over 30 s and 2D data reduction was performed with the aid of the FIT2D

software[108]. Silver behenate was used as a q-vector standard while the scattering of an empty sample holder was used for background subtraction.

3.3.12. WIDE-ANGLE SYNCHROTRON X-RAY SCATTERING (WAXS)

Wide-angle synchrotron X-ray scattering (WAXS) experiments were performed at the D01B-SAXS1 beamline at the Brazilian Synchrotron Laboratory (LNLS-Brazil) [109]. Figure 19 shows the beamline set-up used, with indications on the X-ray beam direction, sample and detector positions. A λ = 0.1544 nm point collimated monochromatic beam was used at D01B-SAXS1. Scattered X-rays were recorded using a Pilatus 300k (Dectris) hybrid pixel X-ray detector at a 232 mm sample-to-detector distance, which covers the 0.6 nm^{-1} to 18 nm^{-1} q-range (see Equation 8, section 1.4).

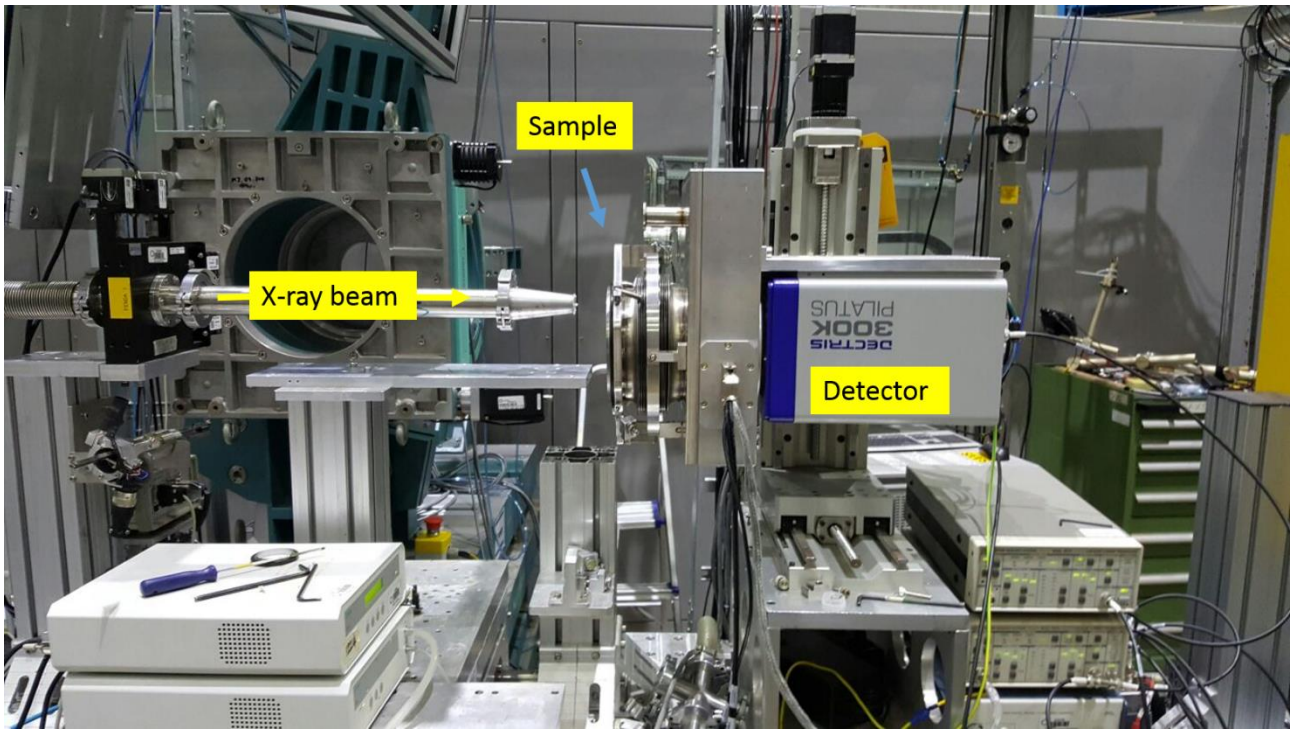

Figure 19 – Photograph of the WAXS experimental set-up at DB01-SAXS1 beamline, LNLS (Brazil).

2D WAXS images were collected over 300 s. The 2D data reduction was performed using FIT2D software[108] and included azimuthal integration, intensity normalization, background subtraction and the q-vector calibration. The scattering of an empty sample holder was used for background subtraction, while the α-alumina standard was used for q-vector calibration. Further data post-processing was performed with Origin 8.5 Pro® software and consisted of the scattering intensity normalization by sample thickness and background correction by I_b (see Equation 12, section 1.4).

Wide-angle scattering curves obtained herein were fitted by the addition of three Lorentzian peaks, as it can be seen in Figure 20. To do so, Origin 8.5 Pro® and the Equation 22 below were used:

$$I(q) \propto \sum_{j=1}^{3} \left[\frac{\Delta q/2}{(q - q_{max})^2 + \left(\Delta q/2\right)^2} \right] \qquad \text{Equation 22}$$

where I(q) is the scattering intensity; q_{max} is the scattering vector at peak maximum, Δq is the full width at half-maximum of the scattering peak and j is an integral number that accounts for the peak assignment shown in Figure 20.

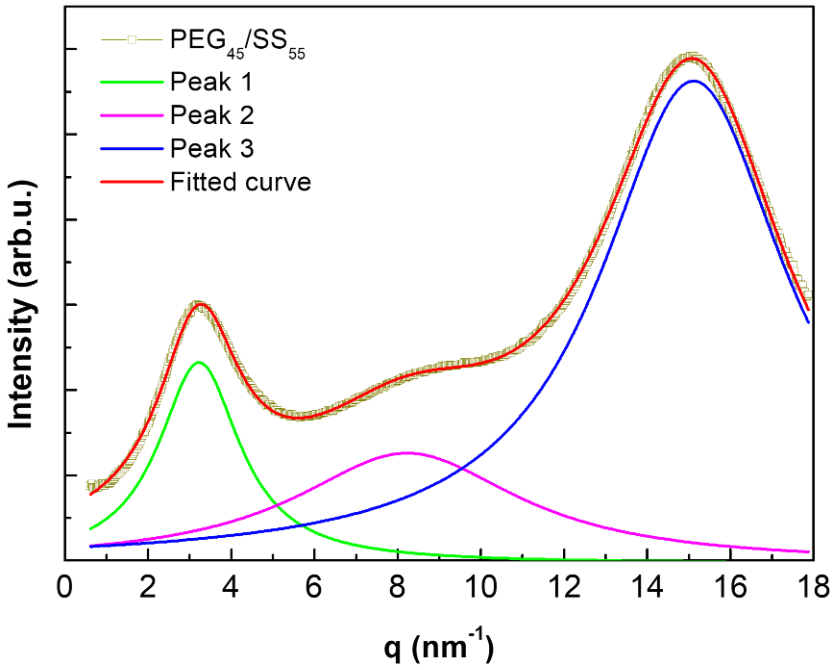

Figure 20 - Typical fit (red line) of the wide-angle X-ray scattering data measured at LNLS. The individual contribution of each peak, for clarity, are also shown by the green, pink and blue curves.

3.3.13. Temperature- and time-dependent small-angle and wide-angle synchrotron X-ray scattering (SAXS/WAXS)

Temperature-dependent simultaneous SAXS/WAXS measurements were performed at the BM26B-DUBBLE beamline at the *European Synchrotron Radiation Facility* (ESRF-France) [91]. Figure 21 shows the beamline set-up used. X-ray beam direction, sample environment (heating stage) and WAXS detector positions are indicated (right). A λ = 0.1033 nm monochromatic beam with point collimation was used at the DUBBLE beamline. Small-angle (SAXS) detection was performed using a Pilatus 1M (Dectris) hybrid pixel X-ray detector at a 3250 mm sample-to-detector distance, covering the 0.04 nm^{-1} to 4 nm^{-1} q-range. Wide-angle (WAXS) detection was performed

simultaneously by using a Pilatus 300K-W (Dectris) hybrid pixel X-ray detector located at an angle and in a 280 mm distance from the sample to cover the 6 nm^{-1} to 50 nm^{-1} q-range.

In all the simultaneous temperature- and time-dependent experiments, each frame has a collection time of 10 s, with 10 ms interval in between frames. SAXS and WAXS scattering curves were collected simultaneously to ensure synchronism. The temperature treatment of the sample was implemented using a DSC600 (Linkam) heating stage, which was adapted to perform X-ray scattering experiments. The adapted DSC600 heating stage is able to perform controlled heating and cooling, however, it does not provide quantitative information concerning heat flow. Indium was used to perform temperature calibration. Approximately 10 mg disk specimens of the samples were compressed and sealed in modified DSC aluminium pans with mica windows. Each sample specimen was subjected to controlled heating and cooling at a rate of 5 °C min^{-1}. Heating scan went from 10 to 200 °C and cooling scan went from 200 to -90 °C with a 5 min isotherm in between.

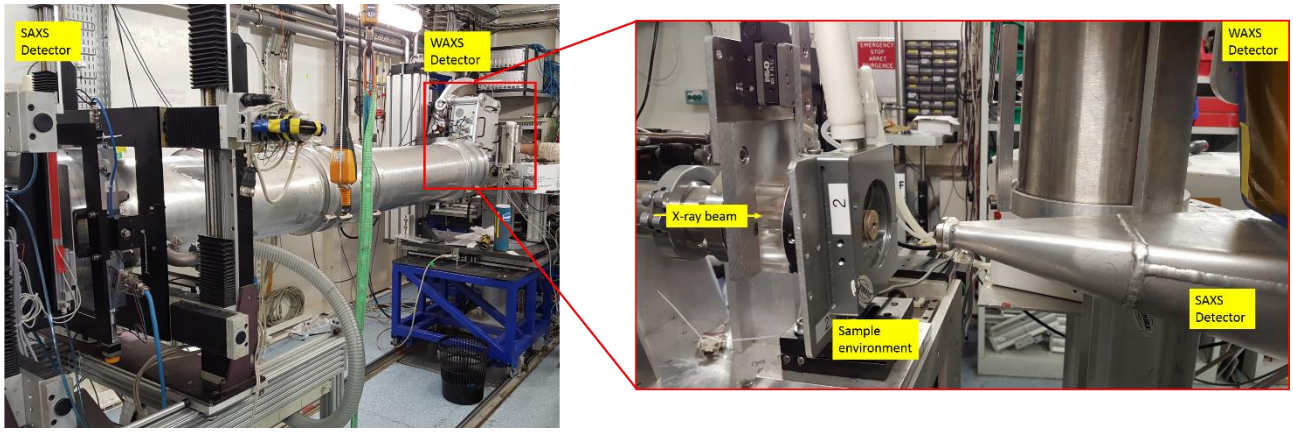

Figure 21 - Photographs of the experimental set-up used at BM26B-DUBBLE beamline, ESRF (France). On the left, it is shown the vacuum tube located in between sample environment and SAXS detector. SAXS and WAXS detector positions are also indicated. On the left, a closer view of the sample environment.

BUBBLE software [110] was used for data reduction, intensity normalization and background subtraction. The scattering of an empty aluminium pan with mica windows was used as background reference, while silver behenate and α-alumina were used as q-vector calibration standards for the SAXS and WAXS data respectively. Further data analyses were performed by using Origin 8.5 Pro® software. In order to obtain each sample crystalline parameters, their correlation function, **γ(r)** (see Equation 14), described in detail in section 1.4, was calculated using the SAXSDAT software [98]. Prior to the correlation function calculation, either the last frame before crystallization or the first frame after melting was subtracted from the analysed frame, with the intent of removing the scattering intensities associated with the silsesquioxane structures.

Apart from the correlation function calculation, a fitting of the $I(q)q^2$ vs q plot was performed, as shown in the Figure 22 (left) example. $I(q)q^2$ vs q plots were used to obtain d_s Equation 9) and Q (Equation 5) values (see section 1.4). For scattering peaks associated with polymer crystallinity, a Lorentzian model analogous to Equation 22 was used, while for scattering peaks associated with silsesquioxane structures the Bigaussian model below was used:

$$I(q) = \begin{cases} I_{max}.e^{-0.5\left(\frac{(q-q_{max})}{\Delta q_1}\right)^2}, & q < q_{max} \\ I_{max}.e^{-0.5\left(\frac{(q-q_{max})}{\Delta q_2}\right)^2}, & q \geq q_{max} \end{cases} \qquad \text{Equation 23}$$

where I_{max} is the scattering intensity at $q_{max,}$ and $\Delta q = (\Delta q_1 + \Delta q_2)/0.85$.

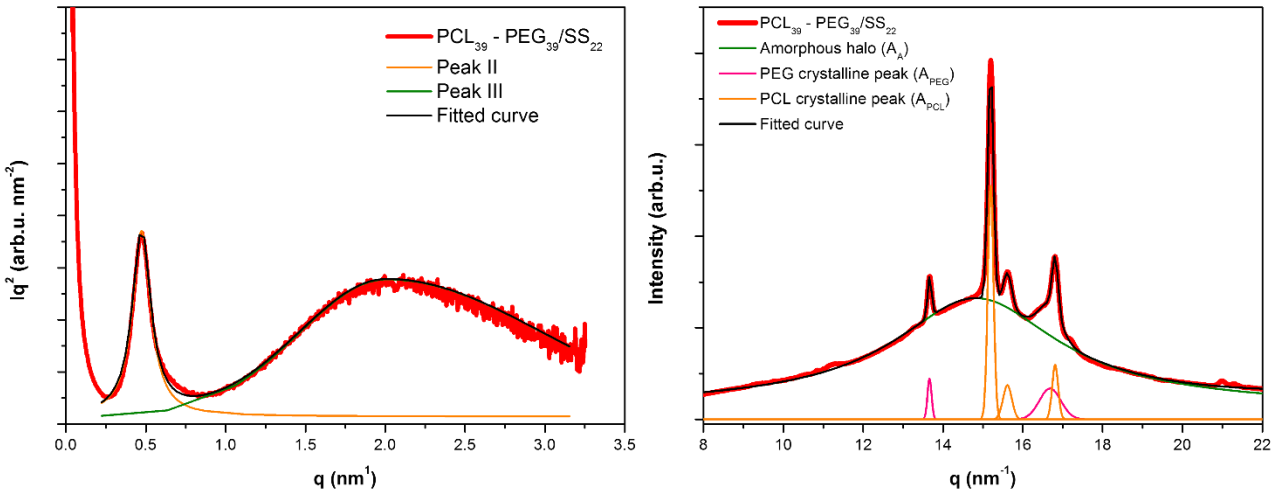

Figure 22 - Typical fit (black lines) of the SAXS (left) and WAXS (right) organic-inorganic hybrid nanocomposite data (red lines) measured at ESRF. The individual contribution of each peak is also shown (green, orange and pink curves) for clarity.

WAXS data were used to investigate the mass degree of crystallinity (χ_{waxs}) variation during the melting and crystallization processes. To do so, the total area of the crystalline and amorphous peaks was used in the following expression:

$$\chi_{WAXS} = \frac{(A_{PCL} + A_{PEG})}{x_c(A_{PCL} + A_{PEG} + A_A)} \qquad \text{Equation 24}$$

where A_{PCL} is the total area of crystalline peaks attributed to PCL; A_{PEG} is the total area of crystalline peaks attributed to PEG; A_A is the amorphous peak total area, irrespective of composition, and x_c is the mass fraction of the crystallizable moieties (excluding silsesquioxane). Figure 22 (right) shows a fitting example of a WAXS curve in which a Lorentzian model, analogous to Equation 22, was used to fit crystalline peaks and obtain A_{PCL} (orange lines) and A_{PEG} (pink lines), while and the following Pseudo-Voigt model to was used to fit the amorphous halo (green line) and obtain A_A:

$$I(q) = A\left[\mu\left(\frac{2}{\pi}\frac{w}{4(q-q_{max})^2+w^2}\right)+(1-\mu)\frac{\sqrt{4ln2}}{\sqrt{\pi}w}e^{-\frac{4ln2}{w}(q-q_{max})^2}\right] \quad \text{Equation 25}$$

where A is the amplitude, $w = {}^{\Delta q}/_{0.85}$ and 0<μ<1 in which μ is the profile shape factor for the linear combination of the Lorentzian and Gaussian models. It is important to mention that the q_{max} and w values of the amorphous peak was fixed throughout the thermal event (i.e. melting or crystallization) of interest.

3.3.14. Atomic force microscopy (AFM)

AFM was performed in a NX10 (Park systems) atomic force microscope operating in tapping mode. Experiments were carried out in air, with a NCHR Si tip (Nanoworld) which presented 8 nm diameter, 125 µm length and 320 kHz resonance frequency. Scanning speed was set at 0.4 to 0.6 line s^{-1} with a 5 µm x 5 µm scan head range. Samples used in this experiment were exactly the same as the ones used in SEM, already mounted on the aluminium stubs. However, before carbon and iridium sputter coating.

4

RESULTS

Laura Caetano Escobar da Silva
INSTITUTE OF CHEMISTRY

4. RESULTS AND DISCUSSION

In this chapter, results concerning the preparation, characterization, morphology and nanostructure of the O-I hybrid nanocomposites developed are presented and discussed. Initially, in subchapter 4.1, typical techniques for the O-I hybrids structural, physical-chemical and thermal characterization are used to demonstrate the effectiveness of the synthetic method developed in this work. Moreover, the results shown in subchapter 4.1 will provide evidences that the atoxic and solvent-free O-I hybrid synthesis developed herein is able to produce materials with similar properties to the ones obtained by conventional sol-gel techniques. In subchapter 4.2, the nanostructure of the amorphous and semicrystalline O-I hybrids are investigated in detail. Based on the combination of the amorphous O-I hybrids' TEM and SAXS results, a model nanostructure to explain the O-I hybrids' morphology (section 4.2.1) is proposed. Finally, in section 0, X-ray scattering results are used to investigate the complex multicomponent nanostructure of the semicrystalline O-I hybrids as well as their thermal behaviour. Part of the results presented herein is already published in *Soft Mater* [111].

4.1. PHYSICAL-CHEMICAL PROPERTIES AND MORPHOLOGY

In this work, a new solvent-free method to synthesize chemically cross-linked organic-inorganic (O-I) hybrid materials was developed and is shown schematically in Figure 23 [111]. This new, simple and atoxic pathway was inspired by the mild conditions of the sol-gel methodology and consists of two subsequent steps. The first step is to incorporate triethoxysilyl groups, from (3-isocianatopropyl) triethoxysilane (IPTES), at the organic prepolymers' (PCL and/or PEG) chain ends. It is noteworthy to mention that PCL and PEG organic prepolymers were studied in two distinct molecular weights. In this first step, carbamate bonds are formed by the reaction of the organic prepolymers' (PCL and/or PEG) hydroxyl terminal groups with the IPTES isocyanate group, generating chemically modified polymers (PCL-IPTES and/or PEG-IPTES). On the one hand, the organic prepolymers are hydroxyl terminated on both ends. On the other hand, IPTES has only one isocyanate group. Therefore, a 1:2 (polymer: IPTES) stoichiometry was used in this first step.

The second step consisted of the triethoxyl group hydrolysis and condensation, which was carried out by the addition of an acid solution (1 wt.% HNO_3) in a 1:6 (polymer: acid) stoichiometry. This second step is made up of two subsequent reactions: triethoxyl hydrolysis, in

which gaseous ethanol evolves and silanol groups are generated at the organic polymer chain ends; and the silanol condensation, in which Si-O-Si bridges, that act as cross-linkers to the polymeric chains, are formed. Silanol formation is the limiting step to the organic moiety cross-linking by the inorganic moieties, since Si-O-Si formation is spontaneous.

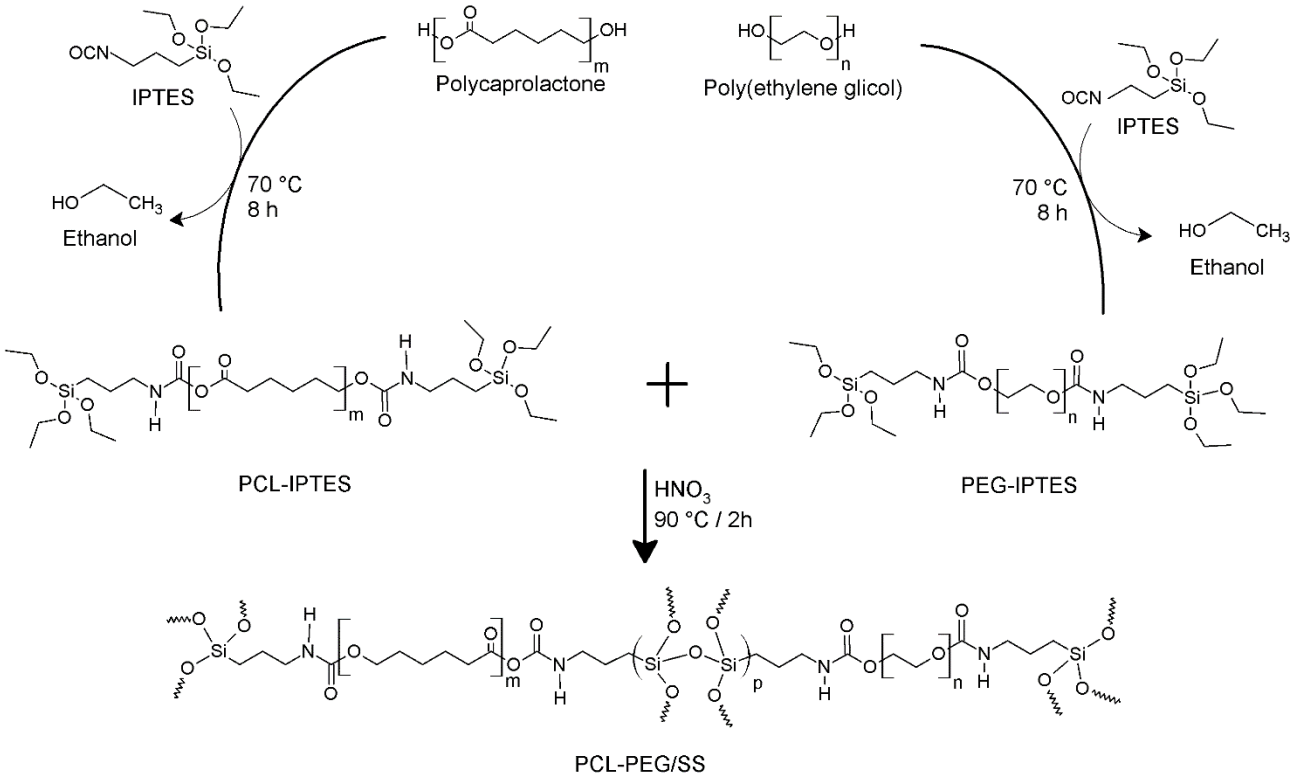

Figure 23 - Schematic and simplified demonstration of the solvent-free *in situ* syntheses of silsesquioxane structures within bicomponent matrices made up of PCL and PEG. PCL-IPTES and PEG-IPTES are the chemically modified organic prepolymer to contain triethoxysilyl end groups.

ATR-IR was used to monitor the reaction evolution over time. Figure 24 shows the first and last spectra taken during PCL (left) and/or PEG (right) chain end modification (hydroxyl to triethoxysilyl), as well as the last spectra taken after the triethoxysilyl hydrolysis-condensation. Samples investigated in Figure 24 resulted in the binary cross-linked O-I hybrids, which were synthesized for comparison. Table 2 shows the ATR-IR band assignment. As can be verified, in all the cases the chain end modification was successful, as the complete consumption of the isocyanate group at the IPTES propyl end, as well as the carbamate bond formation were both observed 8 h after IPTES addition [49]. Triethoxysilyl hydrolysis-condensation (coloured curves) was also confirmed. Hydrolysis was confirmed by the absence of a Si-O-C band, as well as the presence of a small and broad Si-O-H (silanol) band [112]. The presence of a silanol-specific band shows that either condensation did not occur, or it was incomplete. Nevertheless, the multiple overlapping and broad

Si-O-Si bands, show that silanol condensation did in fact occur and, therefore, was incomplete [113]. Literature attributes the occurrence of multiple Si-O-Si bands to the presence of distinct silsesquioxane structures [72,114].

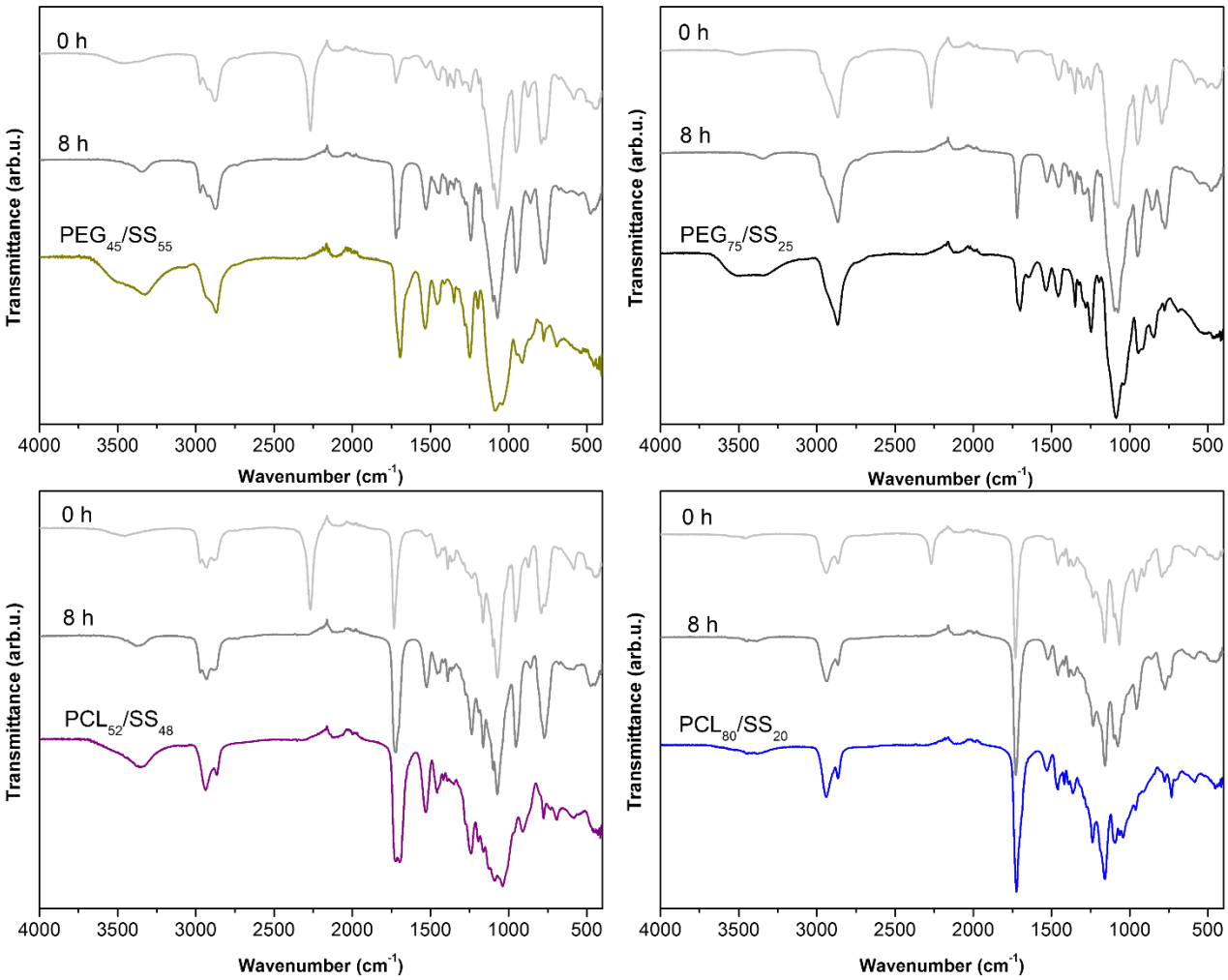

Figure 24 - ATR-IR follow-up of the binary O-I hybrid syntheses: Reaction start (0 h); end of the first step (8 h) and final product (bottom coloured curves).

Table 2 - Band assignment for the infrared spectra shown in Figure 24.

Band (cm^{-1})	Assignment
3526	-OH stretching
3338	-NH stretching (urethane)
2930	-CH stretching (PCL)
2865	-CH stretching (PEG
2274	-CN stretching (IPTES)
1720	-C=O stretching (carbamate)
1530	-N-H bending (carbamate)
1200-1000	-Si-O-Si stretching
912	-Si-O-H stretching
770	-Si-O-C stretching

At last, ATR-IR may also be used to qualitatively confirm the occurrence of both PCL and PEG at the organic moiety of the ternary O-I hybrids. As can be seen in Figure 24, both the 2930 cm^{-1} and 2865 cm^{-1} bands are present in both PCL and PEG, however with reversed relative intensities. At the ATR-IR spectra of the ternary O-I hybrids, such as the ones shown in Figure 25, the distinct relative intensities of the CH stretching bands (2930 cm^{-1} and 2865 cm^{-1}) indicate that both polymers are present. In Figure 25, and throughout this section, for the sake of clarity, only the results related to PCL_{24}-PEG_{24}/SS_{52} and PCL_{39}-PEG_{39}/SS_{22} ternary O-I hybrids are shown. PCL_{24}-PEG_{24}/SS_{52} was prepared by using equal masses of low M_w PCL and PEG prepolymers, while PCL_{39}-PEG_{39}/SS_{22} was prepared by using high M_w PCL and PEG prepolymers. These samples were chosen due to the fact that they represent the properties of all the ternary O-I hybrids. Additional noteworthy information provided by the samples not shown herein, lies solely on the fact that by varying the PCL/PEG weight ratio, the 2930 cm^{-1} and 2865 cm^{-1} band intensities changed accordingly, suggesting that ATR-IR could be used to verify the ternary O-I hybrids composition.

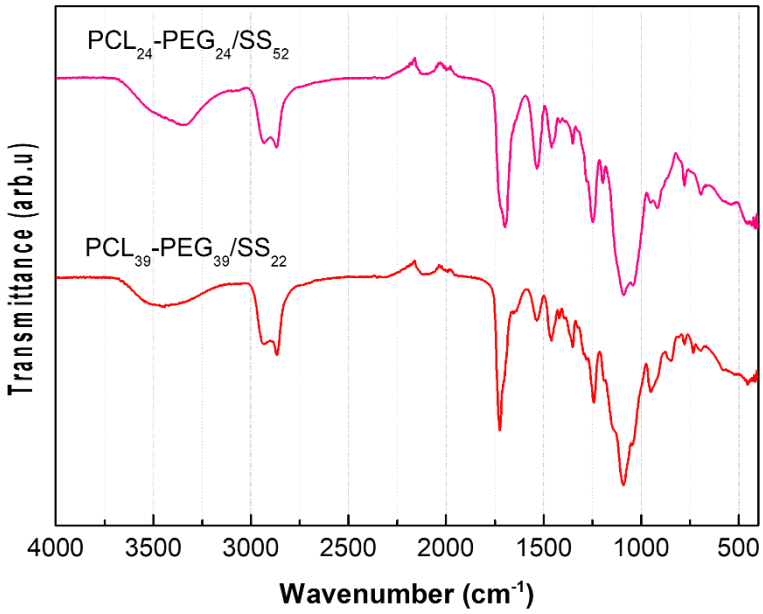

Figure 25 - ATR-IR spectra of the ternary organic-inorganic hybrid nanocomposites made up of low M_w (PCL_{24}-PEG_{24}/SS_{52}) and high M_w prepolymers (PCL_{39}-PEG_{39}/SS_{22}) by using equal masses of PCL and PEG.

Due to the evidences provided by the ATR-IR results that multiple silsesquioxane structures may occur, solid-state ^{29}Si NMR was performed. Figure 26 shows that in fact, in all cases, silicon occurred in distinct molecular arrangements throughout the samples. Moreover, the results also showed that the organic prepolymer's M_w, rather than their chemical structure, was significant to determining which silsesquioxane structures could be formed. This may be verified by the fact that all O-I hybrids made up of low M_w prepolymers (Figure 26, left) show the same

^{29}Si NMR profile. The same is also true for the high M_w prepolymers (Figure 26, right). O-I hybrids made up of low M_w prepolymers presented two distinct signals, T^2 and T^3 (see section 1.2), while O-I hybrids made up of high M_w prepolymers presented three distinguishable signals, T^1, T^2 and T^3. Moreover, the lack of signals in the -40 ppm region, showed that in all cases 100% of the Si atoms were involved in at least one Si-O-Si bond [115]. Assuming that each Si atom is effectively linked to a polymeric chain, a Si atom can only be involved in either one (T^1; -48 ppm), two (T^2; -58 ppm) or three (T^3; -65 ppm) Si-O-Si bonds. Therefore, in the case of T^1 and T^2 atoms, hydroxyl groups (i.e. silanol) complete the Si valence shell (see section 1.2), as it is widely reported [72] and also shown by the ATR-IR results.

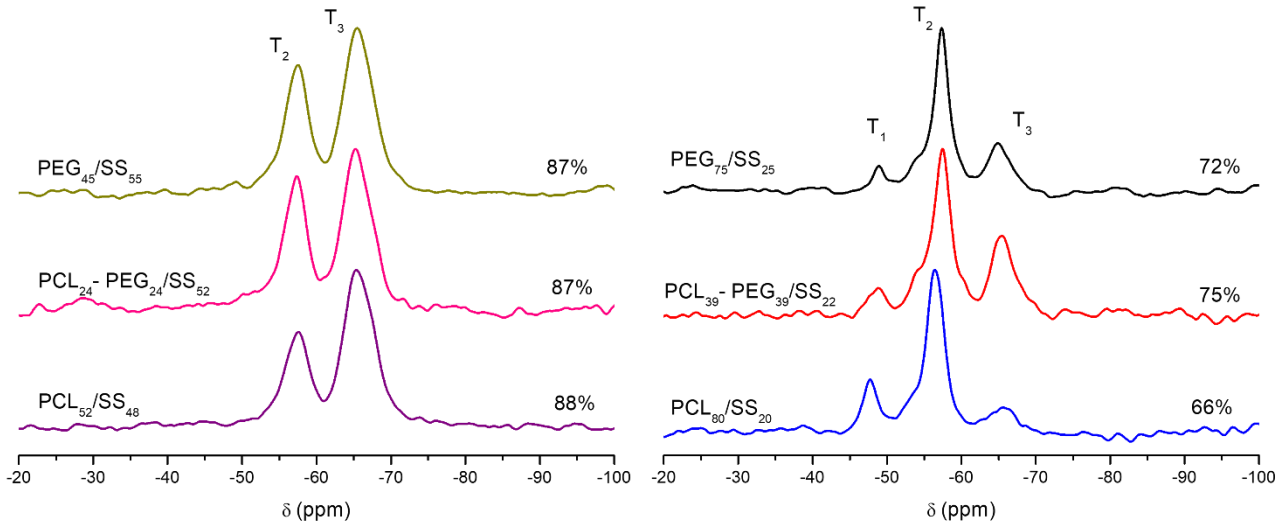

Figure 26 - Solid-State ^{29}Si NMR of the organic-inorganic hybrid nanocomposites made up of low (left) and high (right) M_w prepolymers. The percentages shown are the condensation yield (Equation 26).

The signal integration of HPDEC MAS ^{29}Si NMR curves allows quantitative information concerning atomic ratio. Therefore, it is possible to estimate the degree of condensation, CY, of the samples through the following equation:

$$CY = \frac{(1T^1_{A\%}) + (2T^2_{A\%}) + (3T^3_{A\%})}{3} \qquad \text{Equation 26}$$

where $T^1_{A\%}$ is the area percentage of the peak attributed to T^1 Si atoms, $T^2_{A\%}$ is the area percentage corresponding T^2 Si atoms and $T^3_{A\%}$ is the area corresponding to T^3 Si atoms. CY is an estimate of the amount of ethoxy groups that were effectively converted into Si-O-Si cross-links. In O-I hybrids with low M_w prepolymers, CY revolved around 87% and fluctuations between samples were within experimental error.

Conversely, in O-I hybrids with high M_w prepolymers, CY revolved around 72%. In this case, not only variations within samples were significant (see Figure 26), but also PCL_{80}/SS_{20} showed an abnormally large T_1 abundance (18%), which lead to a smaller T_3 abundance (15%). The PCL prepolymer used as the organic moiety for the PCL_{80}/SS_{20} O-I hybrid preparation has the highest M_w of all prepolymers (see section 3.1). At that M_w range, it is expected that significant viscosity increase occurs with small M_w increase [104]. Therefore, it is possible to conclude that viscosity is the predominant factor governing the cross-linking yield. This is due to the fact that increased viscosity impairs the most thermodynamically stable silsesquioxane structures (silsesquioxane cages containing 100% T^3 Si atoms [72]) to be formed, due to the chain ends mobility restrictions imposed.

Based on the CY, calculated from Equation 26, and the reaction media composition, shown in Table 1 (see section 3.2.1), estimates of the O-I hybrid nanocomposite weight ratios were obtained and are shown in Table 3Table 4. However, these estimates do not take into consideration the unusually low soluble fraction values (W_s), obtained by Soxhlet extraction and shown in Table 4, due to the fact that it is not possible to determine which component was, in fact, extracted during the experiment. W_s results show that irrespective of molecular weight or chemical composition, O-I hybrid nanocomposites were insoluble and, therefore, effectively cross-linked. The PCL-based binary O-I hybrids showed the lowest soluble fractions in both sets of samples (made up of low or high M_w prepolymers), while the ternary O-I hybrids showed increased soluble fractions in comparison with their corresponding binary O-I hybrids. This is an indication that in addition to the triethoxysilyl chain end mobility, the chain end miscibility in the organic moiety also plays an important role in cross-linking efficiency.

Table 3 - Composition estimate, in weight ratio of the O-I hybrid nanocomposites based on the ^{29}Si NMR condensation yield.

	Sample	Weight ratio		
		PCL	**PEG**	**SS**
Amorphous	PEG_{45}/SS_{55}	0.00	0.58	0.42
	PCL_9-PEG_{37}/SS_{54}	0.11	0.48	0.41
	PCL_{19}-PEG_{28}/SS_{53}	0.24	0.36	0.40
	PCL_{24}-PEG_{24}/SS_{52}	0.31	0.30	0.39
	PCL_{29}-PEG_{20}/SS_{51}	0.37	0.25	0.38
	PCL_{40}-PEG_{10}/SS_{50}	0.50	0.11	0.37
	PCL_{52}/SS_{48}	0.65	0.00	0.35
Semicrystalline	PEG_{75}/SS_{25}	0.00	0.83	0.17
	PCL_{39}-PEG_{39}/SS_{22}	038	0.48	0.14
	PCL_{80}/SS_{20}	0.87	0.00	0.13

The O-I hybrid nanocomposites developed in this work were seen to be flexible self-standing films, which are shown in Figure 27. All the materials showed air bubbles visible to the naked eye, which were formed by ethanol evolution during triethoxysilyl hydrolysis-condensation. Nevertheless, most of them were transparent in spite of the bubbles. Transparency is the most compelling evidence that most O-I hybrid nanocomposites were amorphous. Conversely, the opaque PCL_{80}/SS_{20} and PCL_{39}-PEG_{39}/SS_{22} samples have proven to be less flexible and more brittle than the remaining samples. This is a strong indicative that significant amount of polymer crystals are also present in those particular samples. In addition, most samples physical aspects remained unchanged after Soxhlet extraction, indicating that mild heating did not impact significantly on their physical-chemical properties. However, this latter conclusion was not valid to the PEG_{75}/SS_{25} sample, which became opaque after extraction. Probably, this is due to the occurrence of an isothermal crystallization due to the mild heating conditions of the extraction experiment. These assumptions, made on the basis of the physical aspect of the samples, were confirmed by the DSC curves shown in Figure 28. The second heating DSC results are shown in Table 4.

Table 4 – Thermal and physical-chemical properties of the O-I hybrid nanocomposites.

Sample	W_s (wt.%)	D_{HP} (g cm^{-3})	W_r (wt.%)	T_g* (°C)	T_m* (°C)	T_c** (°C)	χ_{DSC}*
PEG_{45}/SS_{55}	9.2	1.05 ± 0.01	23	-23	-	-	-
PCL_{24}-PEG_{24}/SS_{52}	15.5	1.06 ± 0.02	21	-34	-	-	-
PCL_{52}/SS_{48}	3.7	1.14 ± 0.01	22	-19	-	-	-
PEG_{75}/SS_{25}	11.3	1.38 ± 0.01	11	-53	33	-6	0.43
PCL_{39}-PEG_{39}/SS_{22}	12.1	1.54 ± 0.02	11	-53	28	8	0.38
PCL_{80}/SS_{20}	6.3	1.29 ± 0.01	10	-42	48	-12	0.37

* Data taken from the second heating. ** Data taken from the cooling.

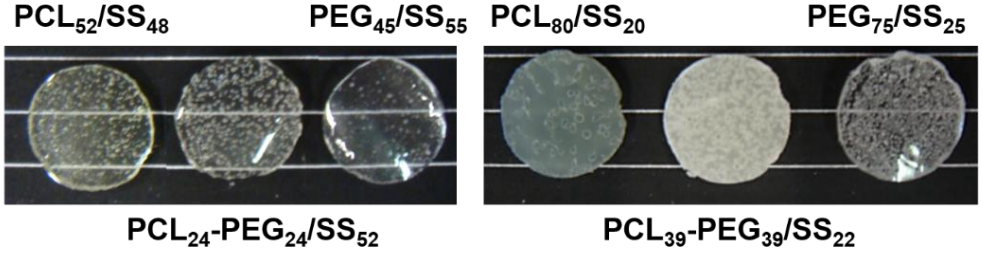

Figure 27 - Photographs of the two sets of O-I hybrids nanocomposites: transparent O-I hybrids made up of low M_w prepolymers (left) and opaque O-I hybrids made up of high M_w prepolymers (right).

Figure 28 shows the first heating, cooling and second heating DSC curves of the two sets of O-I hybrids prepared. O-I hybrids of low M_w prepolymers are on de top, while the O-I hybrids of high M_w prepolymers are on the bottom. The only noticeable feature that these two sets of

materials do share is an endothermic event present at around 125 °C (first heating; left) when the hydrophilic PEG moiety is present at the O-I hybrid composition. This may be attributed to the evaporation of entrapped ethanol and/or absorbed water and was also observed at the thermogravimetric analyses (TGA) shown in Figure 29. PCL_{80}/SS_{20} and PCL_{52}/SS_{48} samples did not show the endothermic event at 125 °C in the DSC analysis, nor the first degradation event in TGA due to their increased hydrophobicity, which impairs water and/or ethanol entrapment.

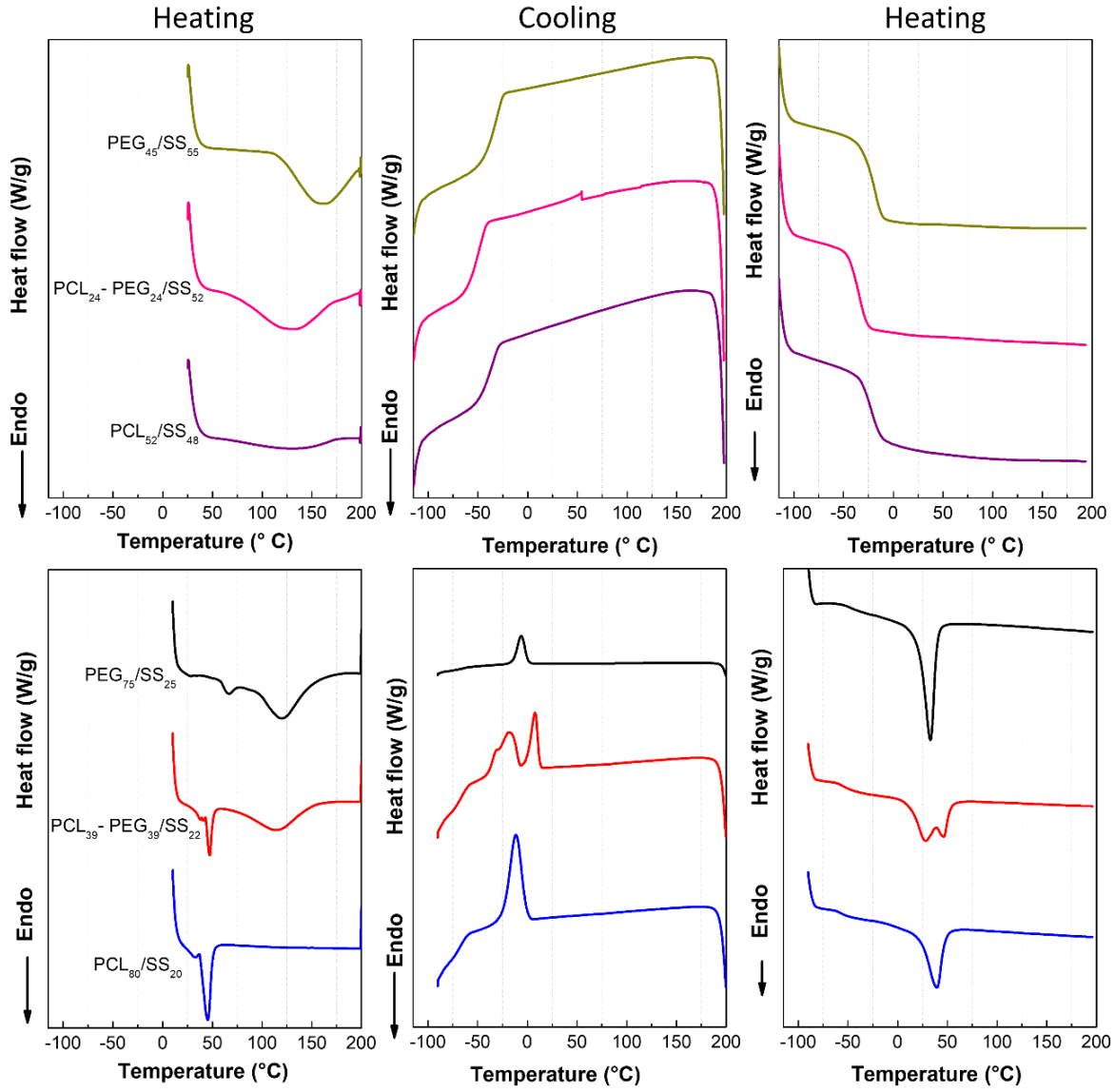

Figure 28 - DSC curves of the organic-inorganic hybrid nanocomposites. First heating (left), cooling (middle) and second heating (right). O-I hybrids of low M_w prepolymers are shown on the top and O-I hybrids of high M_w prepolymers are shown on the bottom.

Apart from this, Figure 28 also showed that O-I hybrids with low M_w prepolymers (top) were all amorphous, while O-I hybrids with high M_w prepolymers (bottom) were all semicrystalline. Moreover, irrespective of crystallinity all O-I hybrids exhibit a single glass transition temperature

(T_g). O-I hybrids with low M_w prepolymers, exhibit a T_g (see Table 4) which is at least 30 °C higher than the original T_g of the PCL (T_g ≈ - 60°C) and/or PEG (T_g ≈ - 50°C) organic prepolymers. This is direct evidence of the mobility restrictions imposed by the silsesquioxane cross-link. In contrast, the T_g of O-I hybrids with high M_w prepolymers was very similar to that of the PCL and/or PEG prepolymers, indicating that in this case the silsesquioxane cross-linking does not impose severe mobility restrictions to the amorphous phase. This is probably due to the prepolymers M_w increase that leads to an approximate 3-fold decrease on the silsesquioxane content.

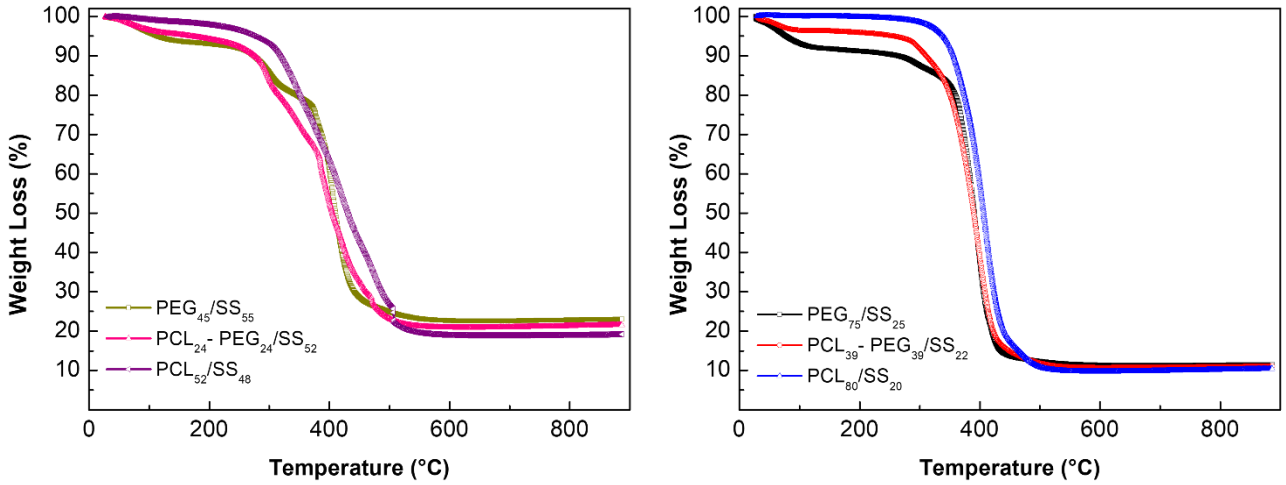

Figure 29 - Thermogravimetric curves of the O-I hybrids made up of low M_w prepolymers (left) and made up of high M_w prepolymers (right).

Even though all O-I hybrids with high M_w prepolymers were semicrystalline, PEG_{75}/SS_{25} was also transparent (see Figure 27). PEG_{75}/SS_{25} transparency is probably due to the low degree of crystallinity at the first heating (see Figure 28). Binary and ternary semicrystalline O-I hybrids showed lower melting (T_m) and crystallization (T_c) temperatures than both PCL (T_m ≈ 60 °C; T_c ≈ 35 °C) and PEG (T_m ≈ 70 °C; T_c ≈ 45 °C) prepolymers. These reductions show that cross-linking occurrence disturbs the crystallization kinetics significantly, despite the amorphous phase being unaffected. Moreover, it is noteworthy to mention that the melting enthalpies might be strikingly different from the first heating to the second heating.

Typically, literature attributes the cross-linking and transparency of O-I hybrid nanocomposites to the formation of siloxane clusters, which are smaller than the visible light wavelength and, therefore, do not scatter it. According to literature, these siloxane clusters are the network nodes that bind the polymeric chains together in a homogeneous network and are expected to have low M_w, being polysilsesquioxane oligomers [95]. Park et al. [113] described that low M_w silsesquioxanes, in particular silsesquioxane cages evaporate at TGA, while high M_w

silsesquioxanes remain as residues. Therefore, based on the estimate sample composition (Table 3) and the weight measured by TGA (Figure 29; Table 4, W_r), it is possible to conclude that both low and high M_w silsesquioxane structures might be present simultaneously at the amorphous O-I hybrids, while the semicrystalline O-I hybrids are mainly composed of high M_w polysilsesquioxane.

Ultimately, the results gathered up to now suggests that there may be distinct silsesquioxane molecular structures present simultaneously at the O-I hybrids nanostructure. Figure 30 shows a suggestion of the possible high and low M_w silsesquioxane chemical structures that might be present within the O-I hybrids. Based on the solid-state ^{29}Si NMR results (see Figure 26), it is possible to suggest that amorphous O-I hybrids are rich in the low M_w silsesquioxane cages, since T^3 is the predominant Si atom conformation in those samples. Conversely, random polysilsesquioxane is expected to be the major silsesquioxane structure at the semicrystalline O-I hybrids, due to the occurrence of T^1 Si atom as well as the high T^2 content. It is important to point out that, based on the thermograms, within a single set of O-I hybrids, the proportion between low and high M_w silsesquioxane structures can be considered unchanged, despite the organic moiety composition, since the residual weight percentage is constant within samples.

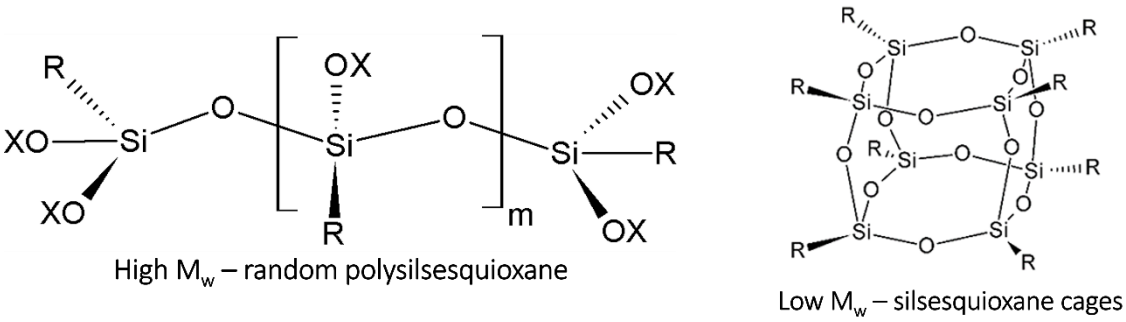

Figure 30 - Possible chemical structures of the *in situ* synthesized silsesquioxanes in which X represents either hydroxyl or ethoxyl groups and R represents either PCL or PEG.

Table 4 also shows the O-I hybrids density (d_{HP}), measured by helium picnometry, which is another important physical-chemical property. Results showed that the amorphous O-I hybrids (made up of low M_w prepolymers) presented densities smaller than the semicrystalline O-I hybrids (made up of high M_w prepolymers), and also smaller than the PCL and PEG prepolymers (1.10 g cm^{-3} and 1.12 g cm^{-3}, respectively). On the one hand, the amorphous O-I hybrids' low density is most likely due to the increase in free volume, provided by the mobility restrictions imposed by the cross-linking. On the other hand, the comparatively large semicrystalline O-I hybrids density is possibly a result of the combination of dense silsesquioxane structures with the organic moiety

crystallization. The absence of density increments in the amorphous O-I hybrids, in comparison with the organic prepolymers, in spite of the occurrence of denser silsesquioxane structures suggests that there is little to none silsesquioxane long-range ordering (i.e. packing), since in these samples the silsesquioxane content is close to 50 wt.%. Conversely, the significant density increments shown in the semicrystalline O-I hybrids suggests that either these two sets of O-I hybrids do not share the same inorganic moiety composition (in terms of silsesquioxane structure distribution), or else that the Si-O-Si cross-link leads to more closely packed crystalline phases and, therefore, a material denser than the original organic prepolymers.

Up to now, the organic moiety composition does not seem to significantly affect the O-I hybrids properties. Nevertheless, it is important to remember that the PCL and PEG prepolymers thermal properties are already similar (see section 1.1), which could explain the lack of composition effect on the O-I hybrids thermal properties. However, one must also remember that PEG is the hydrophilic polymer, while PCL is the hydrophobic one. Therefore, it is expected that their effect on properties such as water uptake should be markedly distinct. Figure 31 shows the O-I hybrids water uptake as a function of time. In equilibrium, there is a clear swelling dependency with PEG content. The PEG prepolymer M_w also seems to be a significant factor for O-I hybrid swelling, since the PEG_{45}/SS_{55} water uptake is smaller than the PCL_{39}-PEG_{39}/SS_{22} water uptake. The swelling dependency on M_w is due to the fact that the length of the molecular chain in between nodes is higher and, therefore, the cross-linking density is smaller. Smaller cross-linking density allows increased mobility in between nodes and, as a consequence, increased swellability. Finally, it is important to mention that all samples preserved not only their spatial dimensions but also their physical aspect throughout the whole experiment. The spatial dimensions preservation irrespective of water uptake associated with the water uptake dependency with PEG content provides basis for the development of new implantable devices made up of the O-I hybrids developed herein.

Another important swellability feature may be observed by accompanying the amorphous ternary O-I hybrids' water uptake as a function of time (Figure 31, left). Increasing PCL/PEG weight ratio up to equal masses of PCL and PEG (PCL_{24}-PEG_{24}/SS_{52}) the water uptake reaches a maximum value. Interestingly, by increasing PCL content even further, samples began to show significant weight loss if left immersed in water after equilibrium (more than 4 hours). This could be associated with PCL hydrolysis [116]. Typically, PCL degrades through a surface erosion mechanism [3]. However, PEG presence in the amorphous ternary O-I hybrids allowed water

permeation and, as a consequence, PCL bulk degradation, which generates weight loss. This ability to induce biodegradation, or else to tailor the degradation rate, provides further basis for the development of biomedical devices. However, it is important to point out that this phenomenon was not observed for the semicrystalline O-I hybrids.

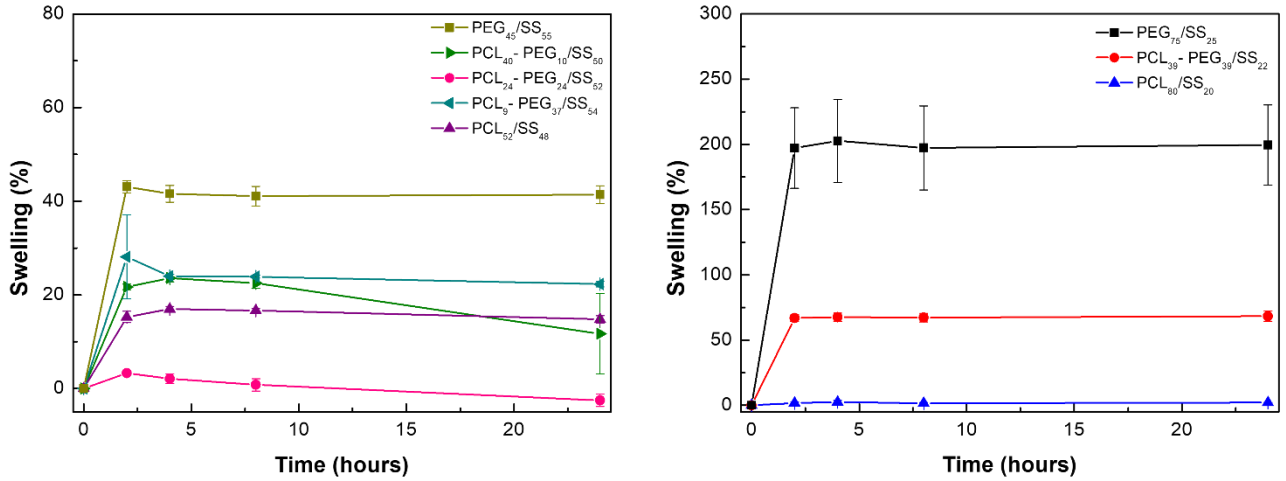

Figure 31 - Water uptake as a function of time: amorphous O-I hybrids on the left and semicrystalline O-I hybrids on the right.

Figure 32 shows the SEM micrographs of the PCL_{24}-PEG_{24}/SS_{52} (amorphous; left) and PCL_{39}-PEG_{39}/SS_{22} (crystalline; right) cross-sections. SEM micrographs were taken at the cryoultramicrotomed cross-sections to enable the visualization of nanosized features in a flat surface without artefacts induced by the cryogenic fracturing. It is possible to observe that the amorphous and semicrystalline O-I hybrids are quite distinct in terms of morphology. PCL_{24}-PEG_{24}/SS_{52} is totally flat at the micron-scale and resembles a starry sky, with bright spots uniformly distributed throughout the imaged area. The morphology observed herein resembles previous reports for other O-I hybrids [71,117] and suggests that amorphous and ternary O-I hybrids are homogeneous at the micron and macro scale, with no evidences of micrometric phase separation. Conversely, the PCL_{39}-PEG_{39}/SS_{22} micrograph shows round-shaped regions surrounded by small micrometric platelets, which are perpendicular to the imaging plane. Even though the cross-section was cryoultramicrotomed, the charge accumulation observed in these platelets show that they are much higher than the rest of the sample, as if they had been expelled from the bulk. This phenomenon highlights the existence of mobile species within the semicrystalline O-I hybrids nanostructure. Moreover, the occurrence of the round-shaped areas suggest that phase separation might also occur.

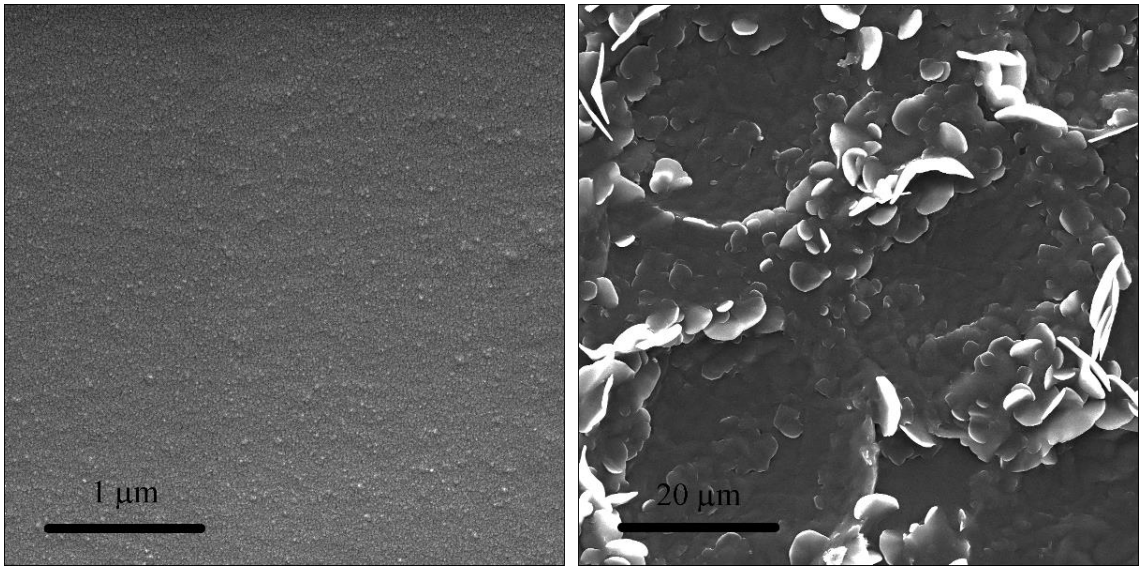

Figure 32 - SEM micrographs of the PCL_{24}-PEG_{24}/SS_{52} (left) and the PCL_{39}-PEG_{39}/SS_{22} (right) samples.

In order to acquire further knowledge on the topic, the same O-I hybrid samples were also imaged using AFM. Figure 33 shows the topography (left) and phase (right) images from AFM tapping mode. At the PCL_{24}-PEG_{24}/SS_{52} (middle) topographic image, two distinct regions are verified. The left region is attributed to the accumulation of a soft material expelled from the bulk. This attribution is made based on the fact that micrometric phase separation would promote visible light scattering and PCL_{24}-PEG_{24}/SS_{52} is transparent. The presence of mobile species might be attributed to the soluble fraction (see Table 4) since the binary O-I hybrids made up solely of PCL (low or high M_w), which show extremely low soluble fractions, did not present evidences of exudation.

The PCL_{39}-PEG_{39}/SS_{22} (top left) topographic image does not show any special features. However, a height variation of around 300 nm is verified in this sample. In this case, height variation is much higher than the thickness of the ultrathin slices cut from that cross-section (≈ 45 - 60 nm). This elevated roughness is probably due to sample deformation, which is a consequence of the room temperature being well above the semicrystalline O-I hybrid T_g (see Table 4). Deformation evidences that the cross-linked network formed at the PCL_{39}-PEG_{39}/SS_{22} O-I hybrid is loose and, therefore, flexible. Conversely, similar roughness is not observed at the PCL_{80}/SS_{20} (Figure 33, bottom) and the PCL_{24}-PEG_{24}/SS_{52} (Figure 33, middle) samples, even though their T_g are also well below room temperature. This result shows that the hybrid networks formed at the PCL_{80}/SS_{20} and the PCL_{24}-PEG_{24}/SS_{52} O-I hybrids are much tighter than the latter. On the one hand, PCL_{24}-PEG_{24}/SS_{52} network tightening may be attributed to the elevated silsesquioxane content that significantly increases cross-linking density, improving resiliency and turning the material less prone to deformation. On the other hand, PCL_{80}/SS_{22} network tightening is attributed to an elevated degree

of crystallinity (see Figure 28), that stiffens the polymer chains between network nodes, hardening the material.

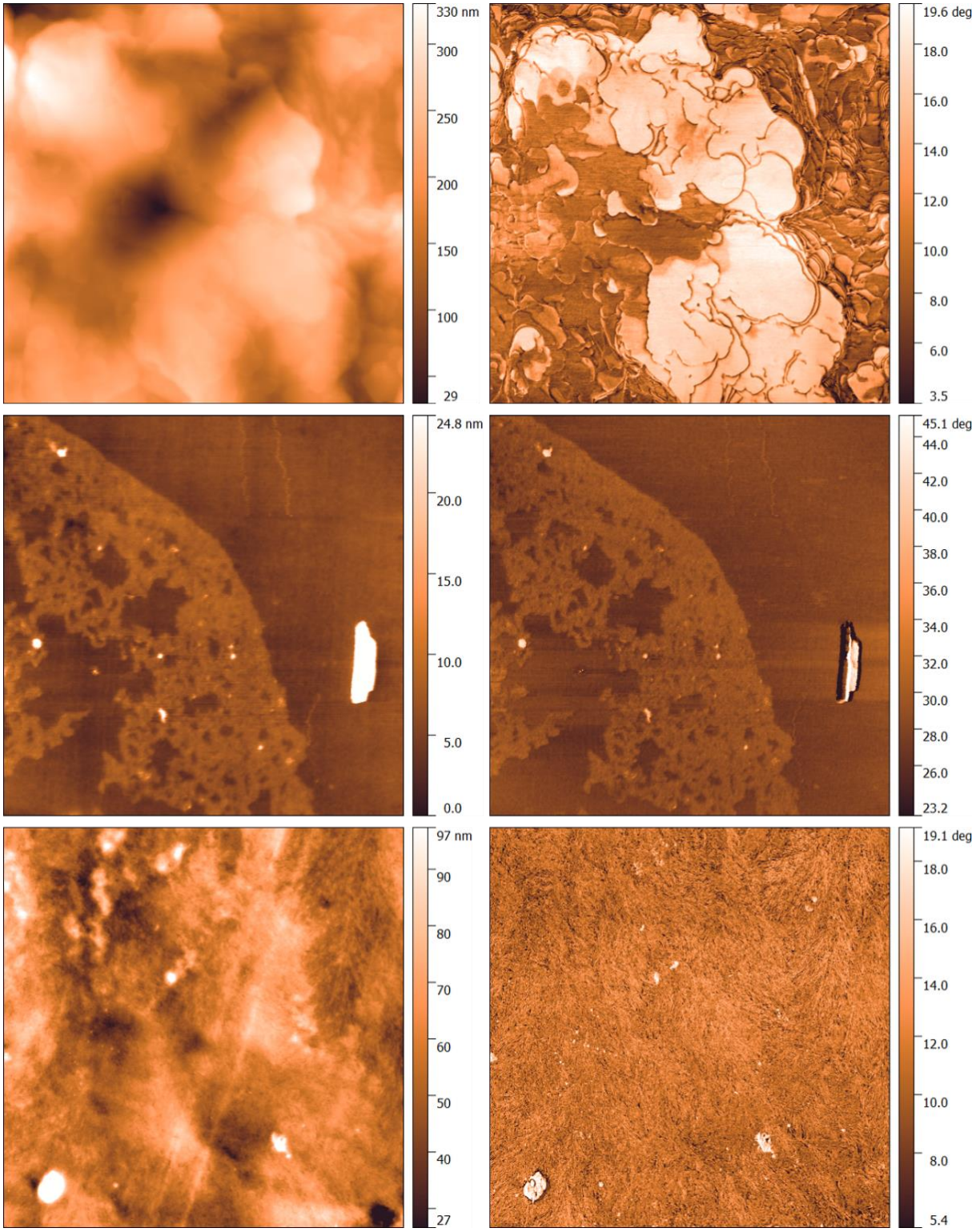

Figure 33 - Topography (left) and phase (right) images of tapping-mode AFM in a 5µm x 5 µm area of the PCL_{39}-PEG_{39}/SS_{22} (top), PCL_{24}-PEG_{24}/SS_{52} (middle) and the PCL_{80}/SS_{20} (bottom) organic-inorganic hybrid nanocomposites.

Apart from the topographic images, Figure 33 also shows the O-I hybrids phase images. Phase and topographic images are taken simultaneously. If on the topographic image the colour scale describes height variations, at the phase images the colour scale shows variations in the sample-tip interaction. Topography and phase do not directly correlate, since sample-tip interaction is only affected by compositional changes (i.e. distinct phases) [118]. PCL_{80}/SS_{20} (bottom) phase image shows a single phase and reveals a spherulitic-like morphology. This result indicates that the crystalline structure at the PCL_{80}/SS_{20} O-I hybrid overpowers the morphology and, possibly, governs the mechanical behaviour of the material. Moreover, there are no evidences of silsesquioxane phase separation at the micron scale. PCL_{24}-PEG_{24}/SS_{52} (middle) phase image shows a flat, rigid and homogeneous matrix from which a soft phase arises (the exudate). The matrix does not show evidences of phase separation of any kind. In contrast, the PCL_{39}-PEG_{39}/SS_{22} phase image shows two distinct phases, since brighter and darker areas ranging from few micrometres to a few hundred nanometres can be clearly distinguished. A clear interface is also observed. Even though the occurrence of two distinct phases is indisputable, from the phase image it is not possible to determine their composition, or even to infer on the silsesquioxane distribution. Nevertheless, based on the known PCL/PEG weight ratio (seeTable 3) and the DSC results (see Figure 28) it is possible to conclude that phase separation is due to the well-known PCL/PEG immiscibility (see section 1.1) while phase contrast is due to the crystalline phase.

Even though AFM provided invaluable information concerning the morphology and phase separation of the investigated materials, it does not offer any insight on the Si distribution. Possibly due to the low resolution. Nevertheless, TEM might bring up valuable information on this topic. Figure 34 shows the TEM micrographs of ultrathin sections cut from the same cross-sections investigated earlier. In TEM, contrast is related to atomic number and electron density fluctuations (see section 1.3). Due to the fact that PCL and PEG average atomic number variation is minimal, the dark spherical domains shown in the PCL_{24}-PEG_{24}/SS_{52} TEM micrograph (top left), that corresponds to the bright spots shown in the SEM micrograph (Figure 32 left), can only be attributed to silsesquioxane. TEM results showed that even at the nanometric scale, the organic moiety of the amorphous and ternary O-I hybrids is homogeneous. However, with silicon-rich spherical domains uniformly distributed throughout the bulk. Conversely, the semicrystalline PCL_{39}-PEG_{39}/SS_{22} O-I hybrid's TEM micrograph (top right) shows an obvious phase separation, which is also in agreement with the SEM and AFM conclusions. In addition, the smaller length scale and the absence of topographical features at the TEM micrographs also revealed that silsesquioxane domains are

also present at the semicrystalline O-I hybrids and the PCL_{39}-PEG_{39}/SS_{22} shows silsesquioxane domains on both phases.

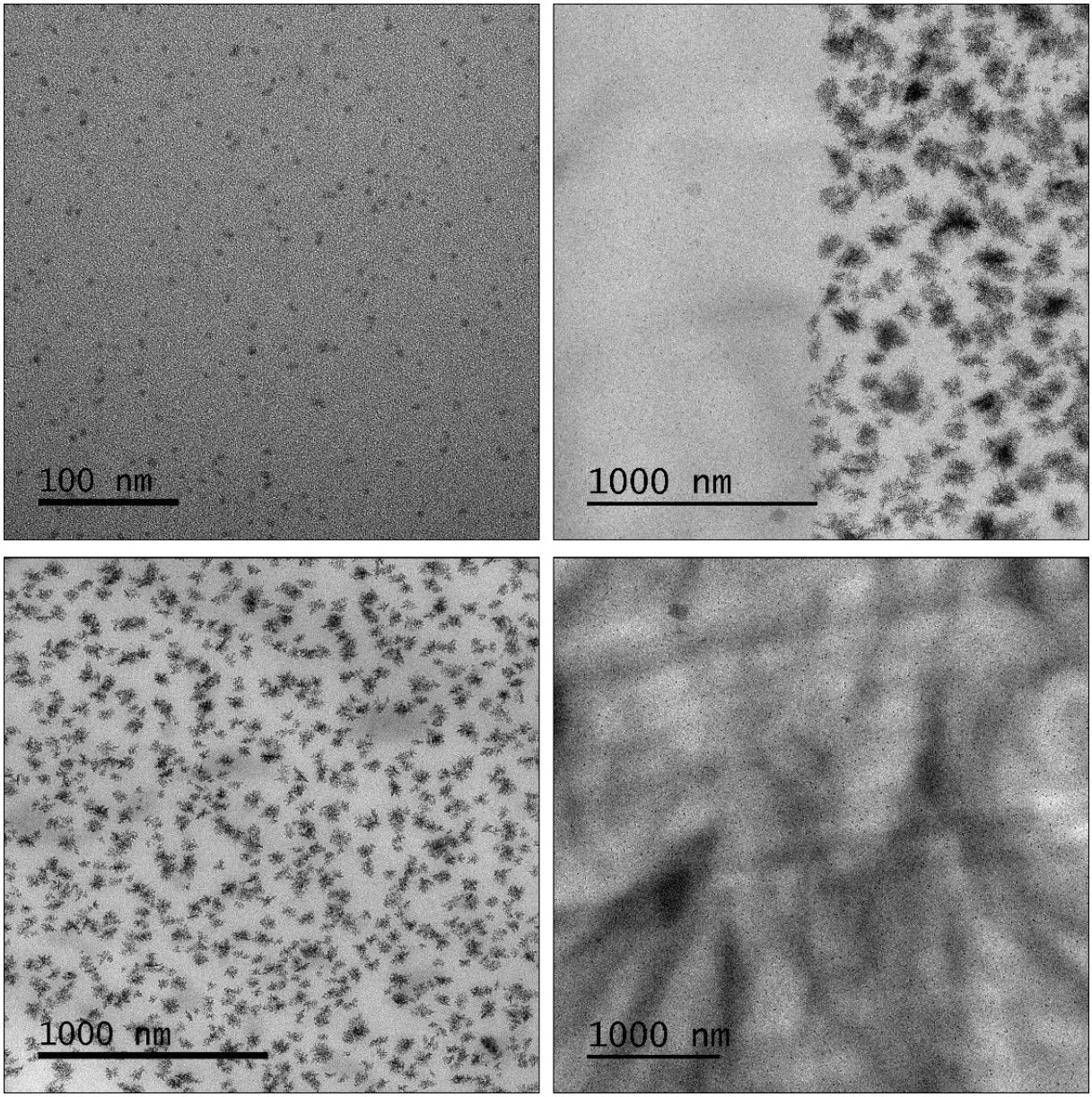

Figure 34 - TEM micrographs of the PCL_{24}-PEG_{24}/SS_{52} (top left), PCL_{39}-PEG_{39}/SS_{22} (top right) PEG_{75}/SS_{25} (bottom left) and the PCL_{80}/SS_{20} (bottom right) samples.

Silsesquioxane occurrence on both phases of the semicrystalline PCL_{39}-PEG_{39}/SS_{22} O-I hybrid confirms that phase separation is due to the organic prepolymers immiscibility and that both phases have an organic and an inorganic moiety. However, it does not allow phase assignment to either PCL/SS or PEG/SS. To shade light on this matter it is necessary to look at the binary PCL_{80}/SS_{20} and PEG_{75}/SS_{25} O-I hybrids TEM micrographs (Figure 34, bottom), from which the phase assignment becomes obvious. PEG/SS phase is the most heterogeneous, with silsesquioxane domains aggregated in large fractal-like structures. In contrast, PCL/SS phase is homogeneous, with

much smaller silsesquioxane domains (few nanometres in diameter) that are uniformly distributed. Nevertheless, the marked PCL_{80}/SS_{20} crystallinity, which is observed at both AFM and TEM, is not observed at the ternary PCL_{39}-PEG_{39}/SS_{22} O-I hybrid. This could either be due to a lower PCL degree of crystallinity at the semicrystalline and ternary O-I hybrid or to the higher contrast at the ternary sample, which is promoted by the larger and denser silsesquioxane structures at the PEG/SS phase. At last, it is important to point out that even though a defined interface between the hybrid phases can be observed and each phase is reasonably free of contamination by the other, phases are well adhered. This result shows that there is limited interaction between the micrometric phases, even though they are chemically bonded to each other. Moreover, it explains the lack of PCL degradation during the water swelling experiments (see Figure 31).

With the intention of further investigating silicon distribution between the bright and dark regions of the PCL_{24}-PEG_{24}/SS_{52} and the PCL_{39}-PEG_{39}/SS_{22} samples, electron energy loss spectra (EELS) and electron spectroscopic images (ESI-TEM) were taken. Figure 35 shows the EELS spectra taken at the region from which the ESI-TEM images, shown in Figure 36, were obtained. Both the amorphous (left) and the semicrystalline (right) O-I hybrids EELS spectra have clear and well-defined Si and C edges, indicating that both the organic and inorganic moieties occur within the imaged area of Figure 34. Moreover, the distinct Si/C ratio between samples (qualitatively verified by the areas of the corresponding edges at the EELS spectra), highlights their distinct chemical composition. An interesting aspect of the PCL_{24}-PEG_{24}/SS_{52} sample is the occurrence of a sharp Si L_1-edge at 155 eV, which represents a chemical shift of 6 eV in relation to the Si L_1-edge of bulk silicon. This chemical shift evidences that, within the investigated region, at least a fraction of the Si atoms are bonded to an oxygen atom in a silica-like environment [119] (i.e. $(SiO_{1.5})_n$ rings and cages). At the PCL39-PEG_{39}/SS_{22} spectra the Si L_1-edge is not resolved; however, an unexpected S K-edge is verified at 165 eV. Sulphur occurrence might be attributed to antioxidants used by the PEG manufacturer to prevent polymer degradation [120].

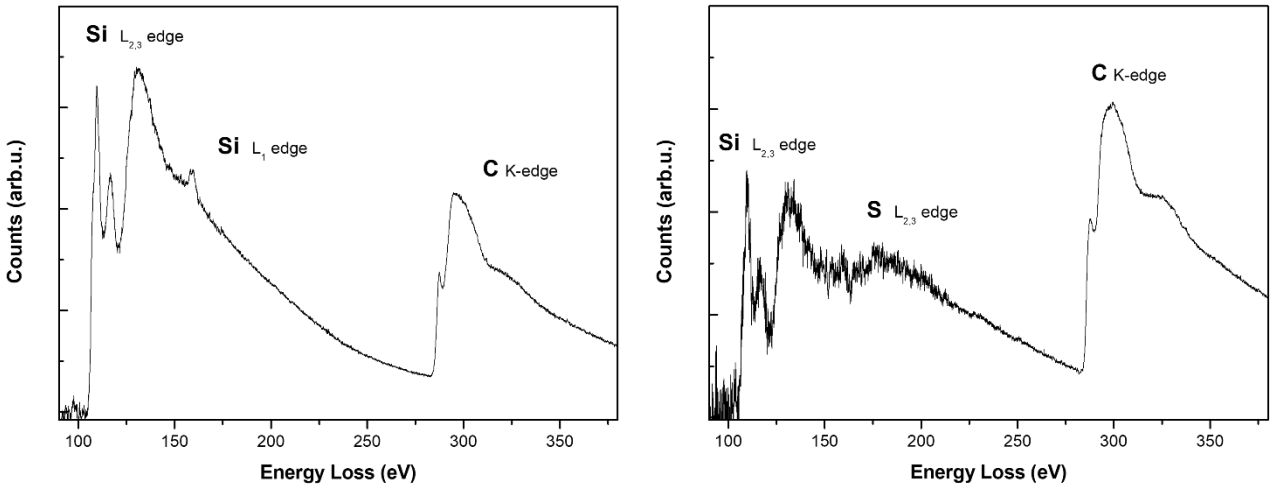

Figure 35 - Electron energy-loss spectra of the PCL_{24}-PEG_{24}/SS_{52} (left) and the PCL_{39}-PEG_{39}/SS_{22} (right) samples.

Figure 36 shows the bright field TEM (top) and the corresponding ESI-TEM (bottom) of the amorphous (left) and semicrystalline (right) ternary O-I hybrids. The bright regions in the bottom images represent Si atom location. Comparing the PCL_{24}-PEG_{24}/SS_{52} (left) images, it is clearly observed that Si is present throughout the whole sample; however, it is more concentrated in the dark domains, such as the ones highlighted by circles. This result showed that, in fact, the inorganic moiety was present in both matrix and nanodomains, suggesting that two distinct silsesquioxane molecular structures and/or phases may occur.

PCL_{39}-PEG_{39}/SS_{22} (right) bright field TEM and ESI-TEM images were taken at the PEG/SS (upper area) and PCL/SS (lower area) interface. From ESI-TEM it is possible to conclude that the Si atoms are mainly located at the darker domains on both the PEG/SS and PCL/SS phases. This result suggests that the inorganic moiety is segregated from the organic moiety at the semicrystalline O-I hybrids. However, this is on the opposite direction from the conclusions reached for the amorphous O-I hybrids. It is important to point out that these opposite results could simply be a consequence of the lower Si concentration at the PCL_{39}-PEG_{39}/SS_{22} O-I hybrid. Therefore, in order to confirm the absence of Si atoms at the PCL_{39}-PEG_{39}/SS_{22} bright matrix, further EELS spectra were taken from the PEG/SS phase. Figure 37 shows a bright field TEM micrograph in which the analysed areas are highlighted. EELS spectra, also shown in Figure 37, are colour coded to aid correspondence. The red spectrum was taken from the bright matrix, while the orange spectrum was taken from the dark domains. Si $L_{2,3}$-edge is clearly observed in both regions. C, N and O K-edges are also observed in both regions, while the S $L_{2,3}$-edge is only verified at the dark domains. Moreover, the Si L_1-edge is only observed at the brighter matrix, indicating that $(SiO_{1.5})_n$ rings and cages are present at the continuous bright matrix. These results point out to the conclusion that

semicrystalline O-I hybrids also show two distinct silsesquioxane structures, one located at the matrix and another located at the dark domains. These results are in agreement with the TGA and solid-state ^{29}Si NMR results.

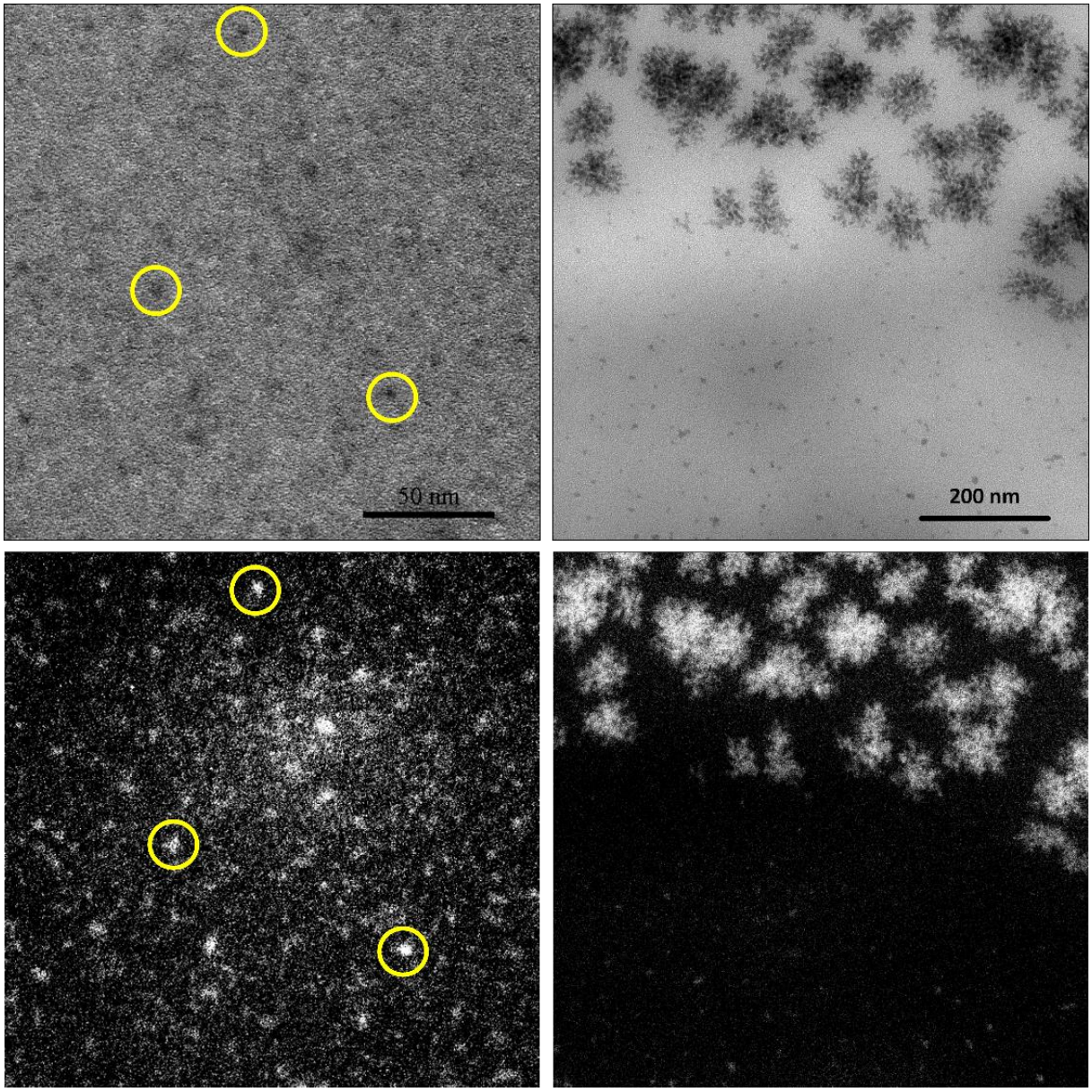

Figure 36 -Bright field TEM micrographs (top) and the corresponding silicon atom distribution map (bottom) of the PCL_{24}-PEG_{24}/SS_{52} (left) and the PCL_{39}-PEG_{39}/SS_{22} (right) samples. Yellow circles are placed to assist image correspondence.

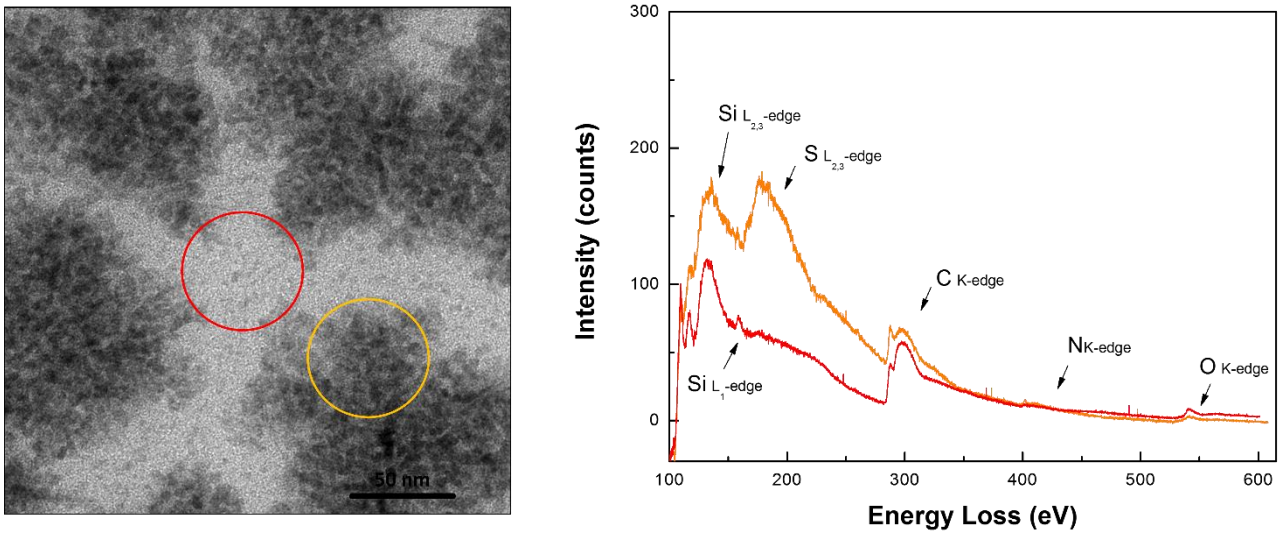

Figure 37 - Bright field TEM micrograph of the PCL_{39}-PEG_{39}/SS_{22} at the PEG/SS domain and its respective electron energy-loss spectra. Colour coded spectra correspond to the selected areas at the micrograph.

4.2. NANOSTRUCTURE INVESTIGATION

In this subchapter the nanostructure of both the amorphous and semicrystalline O-I hybrid nanocomposites are investigated by means of SAXS and TEM. However, amorphous and semicrystalline O-I hybrids are presented separately for clarity. The nanostructure investigation by means of SAXS and TEM of the whole series of amorphous O-I hybrids is shown in section 4.2.1. In this section a representative model that explains the nanostructure of both the binary and ternary O-I hybrids is developed. Conversely, in section 0 the addition of the PCL and PEG crystalline phases to form the semicrystalline O-I hybrids is investigated by means of temperature-dependent and time resolved *in situ* SAXS/WAXS. Crystalline phases addition increased significantly the complexity of the O-I hybrids' nanostructure.

4.2.1. AMORPHOUS O-I HYBRIDS

The nanostructure of O-I hybrid nanocomposites is typically obtained from the interpretation of small-angle X-ray scattering (SAXS) data. Nevertheless, SAXS alone gives room for diverse interpretations and one has to know beforehand the number of phases present in the sample in order to correctly interpret the data (see section 1.4). Dahmouche et al. [95] were the first to propose a model for the nanostructure of chemically cross-linked hybrid nanocomposites obtained through a sol-gel route. In their work, based solely on the SAXS results, the authors suggest that the O-I hybrids are two-phase systems made up of organic polymer chains as matrix and siloxane clusters (≈0.3 nm radii) as network nodes. The authors attribute the single correlation distance (≈2.5 nm), found by SAXS experiments, to the length of the folded polymer chain that is separating the orderly distributed siloxane nodes. Up to now, this two-phase model is the most widely accepted description of an O-I hybrid nanostructure.

However, the results shown in subchapter 4.1 provide compelling evidence that there may be multiple silsesquioxane structures composing the O-I hybrids nanostructure. Nonetheless, based on the TEM results, it is fair to assume that amorphous O-I hybrid nanocomposites such as PCL_{24}-PEG_{24}/SS_{52} could easily be reduced to a two-phase system (Figure 34). In that case, based on the Dahmouche et al. [95] model, the dark domains observed would be attributed to siloxane clusters. In order to verify this assumption, the dark domains size and distance were measured from the TEM micrographs. Figure 38, shows the average domain radius (left) and interdomain distances (right) plotted as a function of PCL weight ratio. For each sample at least 150 nanodomains were measured from at least five distinct regions. Results showed that with increasing PCL content, nanodomains

became smaller and less frequent at the nanoscale, even though there was no significant variation on the interdomain distance. In terms of morphology, there are still few studies available concerning the microscopic bulk characterization of O-I hybrid nanocomposites. Nevertheless, the results shown herein are in good agreement with literature, where it is frequently reported the occurrence of dark domains with sizes at the range of tens of nanometres up to a few microns [71,117,121].

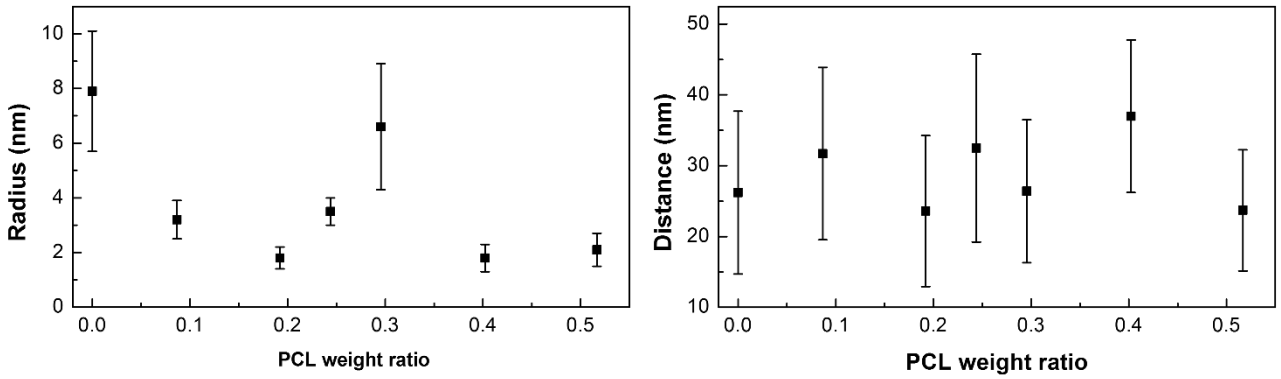

Figure 38 - Radius of the dark domains (left) and interdomain distances (right) measured by TEM as a function of PCL weight ratio at the amorphous O-I hybrid nanocomposites.

Figure 39 shows the synchrotron X-ray scattering measurements performed at the amorphous O-I hybrid nanocomposites. At both the small-angle and the wide-angle regions, all samples presented a similar scattering profile. However, it is noteworthy to mention that even after background subtraction and intensity normalization the PEG_{45}/SS_{55} scattering intensity at the wide-angle (WAXS) region was abnormally higher than the rest of the O-I hybrid nanocomposites. SAXS (left) and WAXS (right) curves of the binary and ternary amorphous O-I hybrids overlap at the 1 nm^{-1} to 4 nm^{-1} q-range. At the very low q-region of the SAXS curves, $q < 0.25$ nm^{-1}, a monotonic decrease of the scattering intensity, characteristic of gel-like systems, is observed, while at the WAXS region three Lorentzian peaks are clearly distinguished. In X-ray scattering, peaks usually indicate the occurrence of periodic electronic density fluctuations or orderly spaced scattering objects. Section 1.4 describes in detail the mathematical treatment used to extract structural parameters, such as d_s, R_s an L_c from the observed peaks.

Peak 1, which is observed at both the SAXS and WAXS curves, can be related to an approximate 2 nm correlation distance, d_s (Equation 9), between scattering objects and, therefore, was attributed to the distance between siloxane clusters in the ordered network [14]. Peak 2, only shown at the WAXS curve, can be linked to a correlation distance of approximately 0.7 nm and was attributed to electron density fluctuations due to amorphous high M_w random polysilsesquioxane.

At last, peak 3, at a correlation distance of 0.4 nm, was attributed to the characteristic amorphous halo of both PCL and/or PEG [23].

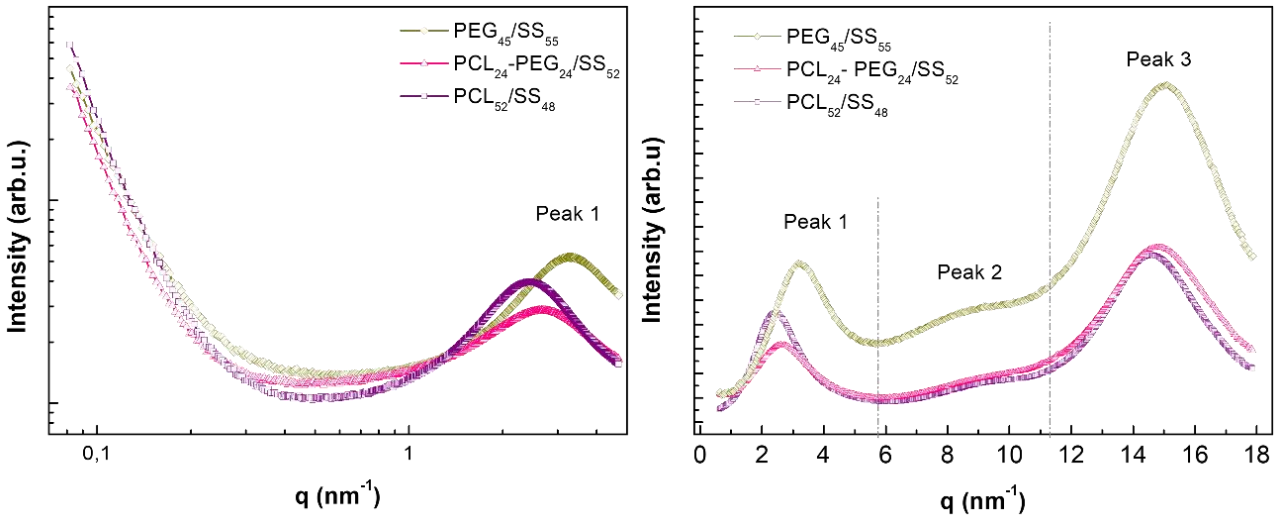

Figure 39 - Small-angle (left) and wide-angle (right) scattering curves of the amorphous O-I hybrid nanocomposites. SAXS andWAXS data overlap at 1 < q < 4 nm^{-1}.

The correlation distance associated with peak 3 was unchanged as a function of the amorphous O-I hybrid composition, whereas the correlation distance associated with peak 2 decreased linearly in relation to the PCL weight ratio. This result showed that the random polysilsesquioxane chemical structure is highly affected by the organic prepolymer composition. In contrast, the correlation distance associated with peak 1, showed a linear increase in relation to the PCL weight ratio. Peak 1 and peak 2 correlation distances (d_s) as a function of PCL weight ratio are shown in Figure 40. The linear increase of the peak 1 d_s value with increasing PCL content could be attributed to an increase in the average length of the polymeric chain between the network nodes. In order to verify this assumption, the Avogadro® software was used to estimate the extended chain lengths of the low M_w PCL and PEG prepolymers. PEG extended length was found to be 4.5 nm, while PCL extended length was found to be larger, 5.3 nm. PEG_{45}/SS_{55} d_s value was 1.9 nm while PCL_{52}/SS_{48} d_s value was 2.6 nm. Therefore, the d_s values obtained herein could, in fact, be related to the length of the PCL and/or PEG chains, provided that chain folding in between nodes is assumed. In addition, this linear d_s increase with increasing PCL content clearly showed that for the ternary and amorphous O-I hybrid nanocomposites, the cross-linked network included indistinctly both PCL and PEG organic prepolymers. However, it is important to point out that the d_s values reported from the scattering data are only 15% of the interdomain distances measured by TEM (33 ± 13 nm). This

is a clear indication that these parameters are related to distinct lengths within this system, which is in agreement with the results shown in section 4.1.

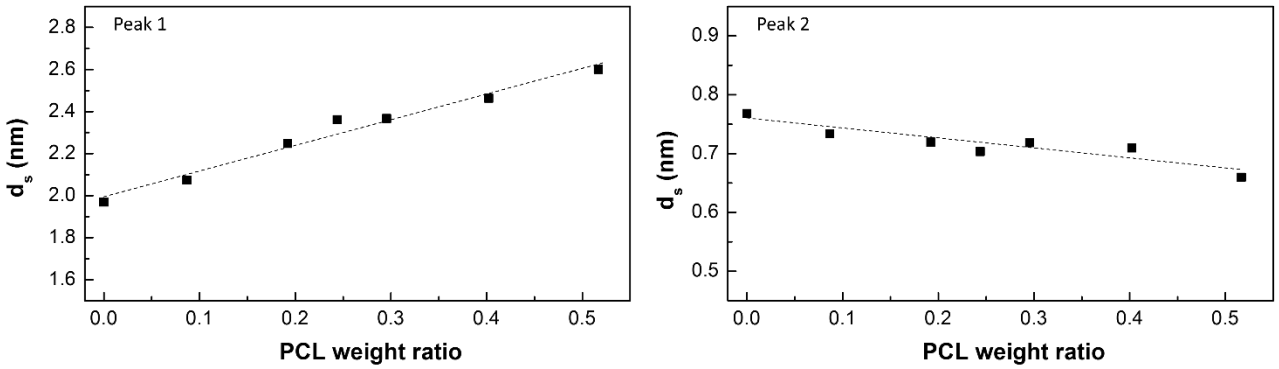

Figure 40 - Correlation distances (d_s) found for WAXS peaks 1 and 2 (see Figure 20) as a function of PCL weight ratio at the amorphous O-I hybrid nanocomposites.

The radii, R_s, of the scattering objects related to peak 1 were estimated by means of Equation 11 (see subchapter 1.4). The R_s values as a function of PCL weight ratio are shown in Figure 41. As it can be seen, R_s values also increase linearly with increasing PCL weight ratio and lie in the 0.32 to 0.45 nm range. Typically, $(SiO)_8$ closed cage radius is 0.5 nm [122]. Therefore, R_s values indicate that the network nodes are actually silsesquioxane cages rather than amorphous siloxane clusters. Possibly, the increased R_s values with increasing PCL weight ratio is related to the PCL hydrophobicity, which could facilitate the triethoxysilyl chain ends' mobility. As a consequence, the most thermodynamically stable silsesquioxane cages, which are the closed $(SiO)_8$ cages (see Figure 30), may be predominant at the binary PCL_{52}/SS_{48} nanocomposite. Finally, similar to the d_s results, R_s values do not show correlation with the TEM data.

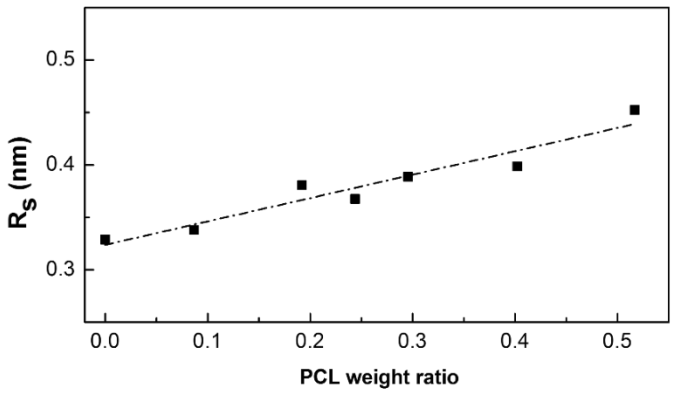

Figure 41 - Scherrer's radius of the silsesquioxane nodes as a function of PCL weight ratio at the amorphous O-I hybrid nanocomposites.

In contrast with d_s and R_s, the coherence length (L_c) values (Equation 10; Figure 42) do not show a linear behaviour in relation to the PCL weight ratio. As discussed in subchapter 1.4, the

coherence length is a measurement of the long-range ordering of the scattering objects that is based on the Bragg's peak FWHM (see Figure 15; subchapter 1.4). L_c assumes that scattering objects form a compact arrangement (i.e. a concentrated system). Amorphous and ternary O-I hybrid nanocomposites showed much smaller L_c than both PCL_{52}/SS_{48} and PEG_{45}/SS_{55} nanocomposites. PCL_{52}/SS_{48} has the highest coherence length (approximately 8 nm), which is attributed to the highest d_s and R_s values.

The significant reduction in the L_c values for the ternary nanocomposites in relation to the binary nanocomposites is an evidence that, in the ternary O-I hybrid nanocomposites, both PCL and PEG prepolymers were involved in the cross-linked network (as also shown by the d_s values). However, due to the low PCL and PEG prepolymers' affinity, the addition of a second polymer to the reaction media disturbed the network formation, resulting in smaller L_c. The relatively low L_c values (approximately 3 times the d_s values for all samples) are an indication of a short-range order and a gel-like morphology, in which small grains of an ordered network (i.e. gel domains, see Figure 5) are isotropically arranged and collapsed together, forming a homogeneous and transparent solid. This gel-like structure has already been reported for other silicon-based materials such as glass [123].

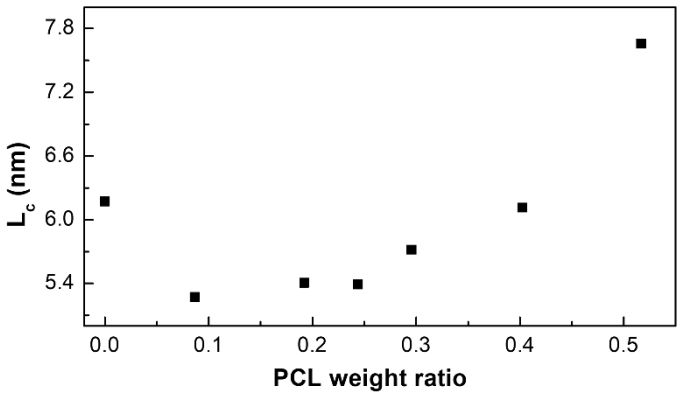

Figure 42 - Length of coherence of the silsesquioxane nodes' arrangement at the amorphous O-I hybrid nanocomposites.

In this work, X-ray scattering curves were not obtained in absolute scale and, therefore, the invariant and the relative electron density difference between phases were calculated. Figure 43 shows Q^{exp} obtained from the integration of the isolated peak 1 scattering curve (see subchapter 1.4 and subchapter 3.3.12). It is evident that Q^{exp} follows a complex and non-linear behaviour as a function of PCL weight ratio. This is an indicative that the O-I hybrids developed herein cannot be approximated to a biphasic system.

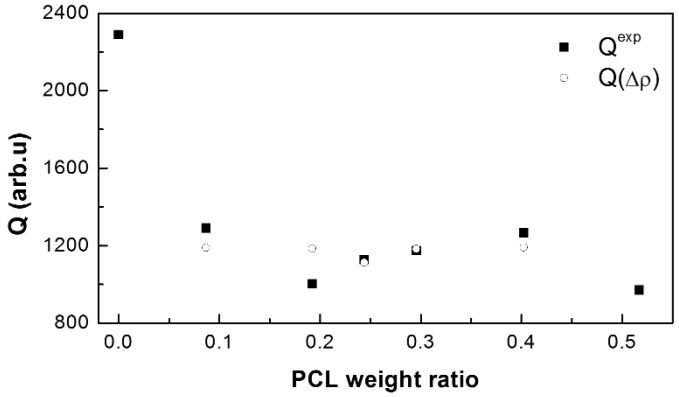

Figure 43 - Amorphous O-I hybrid nanocomposites measured (Q^{EXP}) and calculated ($Q_k(\Delta\rho)$) invariants as a function of PCL weight ratio.

In order to investigate the non-linear behaviour of the invariant, the electronic density differences, Δρ = ($\rho_i - \rho_j$), were calculated based on Equation 5 (see subchapter 1.4). Assuming that not only all the five ternary hybrid nanocomposites own the same number of phases, but also that there is a single Δρ set that is a solution to all, Equation 27, was used to fit calculated invariants $Q(\Delta\rho)$ to the Q^{exp} obtained experimentally, as a way of confirming O-I hybrids' phase composition.

$$f(\Delta\rho) = \sum_{k=1}^{5} \left(\frac{Q^{exp}}{2\pi^2} - \frac{Q(\Delta\rho)}{2\pi^2} \right)^2 \qquad \text{Equation 27}$$

The solution to Equation 27, in which the k subscript is a reference to the five ternary and amorphous O-I hybrid nanocomposites, is given by the Δρ set for which $f(\Delta\rho)$ is minimal. A gradient descent optimization was performed, using the built-in *fminunc* function in GNU Octave® software[124], to find the minimum $f(\Delta\rho)$ and its corresponding Δρ set. Nevertheless, estimates on the number of phases and their respective volumetric ratio need to be provided. Initially, biphasic and triphasic systems were assumed. However, the overall $Q_k(\Delta\rho)$ fit, as a function of PCL weight ratio, was not good and elevated squared residues were found. Conversely, the fit of a four-phase system (see Figure 43) was found to be satisfactory. This four-phase system consisted of high M_w polysilsesquioxane nanoparticles (NP), silsesquioxane cages (SC), cross-linked polymer (CP) and unbound polymer (UP) and was reached through the following equation:

$$\mathrm{Q}(\Delta\boldsymbol{\rho}) = 2\pi^2 \Big[\emptyset_{up}\emptyset_{cp}(\rho_{up} - \rho_{cp})^2 + \emptyset_{up}\emptyset_{np}(\rho_{up} - \rho_{np})^2 + \emptyset_{up}\emptyset_{sc}(\rho_{up} - \rho_{sc})^2 + \emptyset_{cp}\emptyset_{np}(\rho_{cp} - \rho_{np})^2 + \emptyset_{cp}\emptyset_{sc}(\rho_{cp} - \rho_{sc})^2 + \emptyset_{np}\emptyset_{sc}(\rho_{np} - \rho_{sc})^2 \Big] \qquad \text{Equation 28}$$

where ϕ and ρ are, respectively, the volumetric ratio and the electronic contrast of each phase.

Table 5 presents a summary of the volumetric fractions used in Equation 28 to fit Equation 27 to Q^{exp}. Based on the results presented in subchapter 4.1, the only soluble component

in this system is the unbound polymer, described by the Soxhlet experiments. Therefore, the soluble fractions shown in Table 4 were directly converted into the unbound polymer's volume fraction (Φ_{up}). The difference between the overall volume fraction of organic polymers (PCL+PEG) and Φ_{up} was assumed to be the cross-linked polymer's volume fraction (Φ_{cl}). In order to determine the two remaining volume fractions (Φ_{np}, Φ_{sc}), the average silicon atomic ratio found in the ^{29}Si NMR analysis (Figure 26), was converted into volume ratio. For that, it was necessary to approximate that all Si atoms present in the cross-linked matrix (silsesquioxane cages) are T^3 type and all Si atoms present in the polysilsesquioxane nanoparticles are T^2 type.

Table 5 - Volume fractions used in the estimation of the electron density differences.

Sample	Volume fraction			
	ϕ_{up}	ϕ_{cp}	ϕ_{np}	ϕ_{sc}
PEG/PSS	0.082	0.338	0.238	0.348
PCL_1-PEG_4/PSS	0.056	0.374	0.226	0.344
PCL_2-PEG_3/PSS	0.067	0.379	0.220	0.333
PCL_1-PEG_1/PSS	0.140	0.314	0.217	0.329
PCL_3-PEG_2/PSS	0.074	0.387	0.214	0.325
PCL_4-PEG_1/PSS	0,069	0.407	0.208	0.316
PCL/PSS	0.034	0.459	0.169	0.338

It is important to highlight that for the gradient descent optimization method performed in this work only the ternary hybrids were considered. Moreover, in the four-phase model, the final sum of the minimum squared residues was 36 while in the biphasic and triphasic models it was around 200 or above. The Q(ρ) values found by the four-phase model are also shown in Figure 43, while the relative electronic densities for each phase are shown in Table 6. From these results, the strongest relative contrast found is between the cross-linked polymer and the silsesquioxane nodes (ρ_{sc} - ρ_{cl}), which is in agreement with the experimental data and the two-phase model usually shown in literature [95], but not with the TEM micrographs. The main reason for this apparent contradiction is that this contrast occurs only at a molecular level and, therefore, is not observable by TEM.

Table 6 - Relative electronic densities of each phase present in the amorphous O-I hybrid nanocomposites.

Phase	ρ
np	9.3
sc	12.3
cl	8.2
up	3.2

Based on these findings, a model for the nanostructure of these solvent-free and amorphous O-I hybrid nanocomposites is proposed in Figure 44. The cross-linked hybrid network

forms grains, whose average size is given by L_c. Gel grains are isotropically distributed throughout the matrix and within these grains, the silsesquioxane cages (red squares) are orderly spaced by the cross-linked polymeric chains (blue lines). High M_w polysilsesquioxane is segregated into spherical nanoparticles (pink spheres). The unbound polymer (purple lines) may be found either entrapped between the network grains or in the nanoparticle-matrix interface, in which case the unbound polymer's chain-ends can act as compatibilizer. PCL and PEG chains are undistinguishable and randomly distributed between the two organic phases.

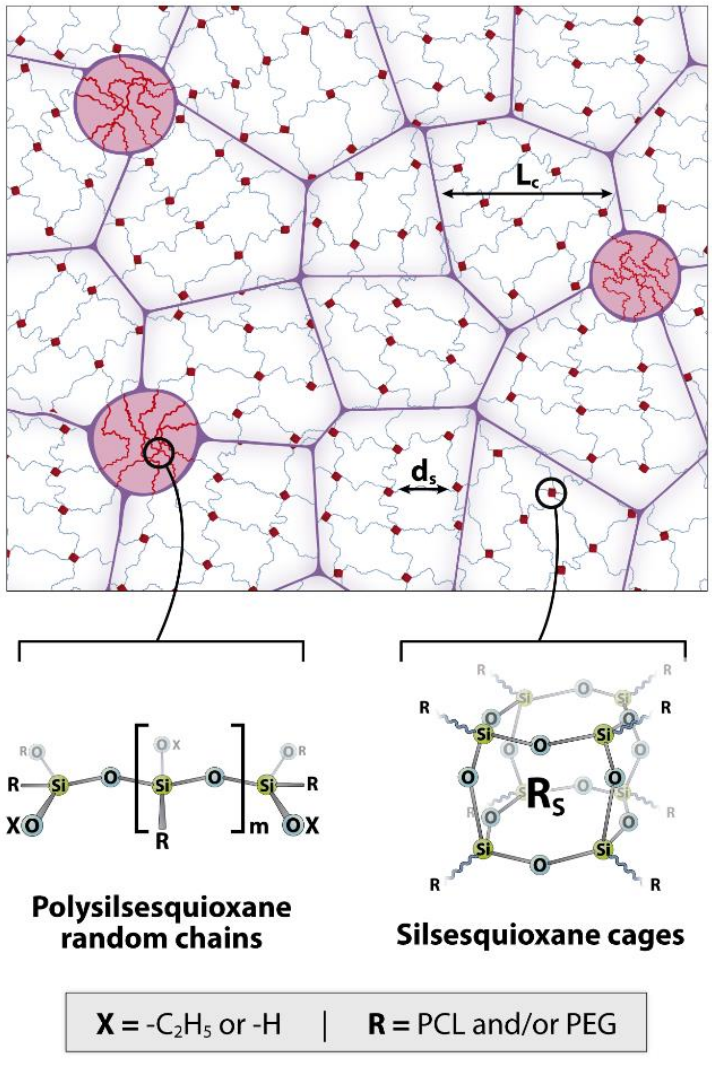

Figure 44 - Schematic representation of the morphology and nanostructure of the amorphous binary and ternary O-I hybrid nanocomposites, extracted from da Silva et al. [111], in which the cross-linked polymer and the silsesquioxane nodes form ordered structures that nucleate and grow isotropically into grains that collapse together to form a solid. The L_c. d_s and R_s parameters calculated from X-ray scattering are indicated.

Finally, complementary SAXS measurements, shown in Figure 45, were performed with the intent of acquiring further evidences to support this nanostructural assumption. As mentioned earlier, the low-q region of the SAXS curves (Figure 39) already pointed out to the conclusion of a

gel-like behaviour. However, the temperature-dependent SAXS experiments (Figure 45) showed that the monotonic intensity decrease at this low-q region, which is attributed to the gel-like morphology, remained unchanged throughout the whole experiments. This result showed that the gel-like morphology is most likely preserved even at 200°C, indicating that the amorphous O-I hybrids' nanostructure is stable. Moreover, this results also showed that the gel-like structure is in a higher volumetric ratio than the high M_w random polysilsesquioxane nanoparticles, since the form factor of the nanoparticles is overpowered by the gel scattering, even at high temperatures.

The temperature-dependent SAXS experiments also showed an unexpected result: a strong and temperature-dependent intensity change at the peak 1 region ($1.5 \leq q \leq 3.5$ nm^{-1}). Noticeable intensity changes were not followed by changes in peak position or FWHM (i.e. d_s or L_c variations). This result shows that the network structure within the gel-like grains is not affected by temperature variations. However, the strong intensity changes in the peak 1 region suggests the existence of mobile structures within the ternary O-I hybrid nanocomposites, even at the nanometric length scale, or else that strong temperature-dependent variations in the electronic density of the phases occur. In conclusion, the advanced morphological characterization of the ternary O- hybrids showed that, in spite of the homogeneous macroscopic morphology, binary and ternary amorphous O-I hybrids having low M_w PCL and/or PEG prepolymers at the organic moiety present a complex four-phased nanostructure with a temperature-dependent behaviour.

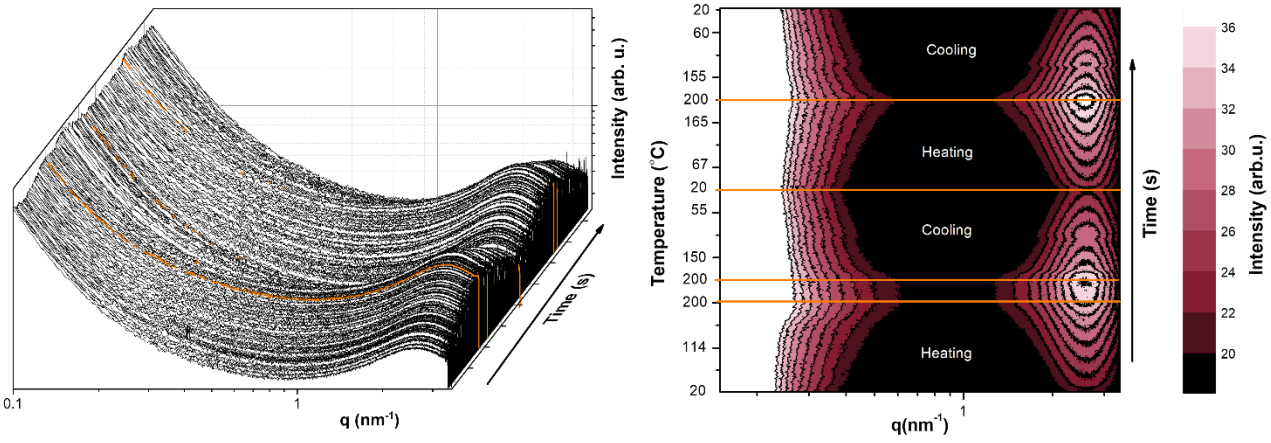

Figure 45 – Three-dimensional (left) and contour (right) plots showing the evolution of the SAXS curves of the PCL_{24}-PEG_{24}/SS_{22} sample as a function of time. Orange lines are used to point the beginning or end of the heating and cooling runs.

4.2.2. SEMICRYSTALLINE O-I HYBRIDS

In bulk methods are an excellent alternative not only for the production of biomedical devices, but also for the production of all sorts of sustainable devices, due to the absence of both solvent and residues. However, in these solvent-free syntheses the number of parameters that may be used to control the devices' final properties is limited. In terms of temperature, the cross-linked materials developed herein allowed a limited temperature range to be used, due to the proximity of the melting and degradation temperatures for both PCL and PEG. In terms of catalyst, biomedical applications limit the possibilities. Moreover, literature has already shown that stoichiometric quantities are the most efficient "catalyst" concentrations [68,125,126]. The organic prepolymer/inorganic prepolymer (IPTES) molar ratio may also be used to tailor device properties. However, it is important to consider that non-stoichiometric molar ratios may also lead to increased heterogeneity and increased soluble fraction.

Therefore, the most efficient way of controlling the physical-chemical properties and morphology of the devices is to manipulate the organic prepolymer's composition and their M_w. On the one hand, in ternary O-I hybrids made up of PCL and PEG, the organic prepolymer composition showed a direct relationship with both water uptake and biodegradation rates, as shown earlier in section 4.1. (Figure 31). On the other hand, increasing the PCL and/or PEG prepolymer M_w inevitably leads to changes in the volumetric fraction of both the organic and inorganic moieties, as well as to the crystallization of either one or both polymers, which increases the number of phases and complexity of these intricate O-I hybrid systems. Therefore, in order to tailor O-I hybrids physical-chemical properties and, as a consequence, to achieve their biomedical potential, it is necessary to study the effect of the additional crystalline phase(s) on the overall O-I hybrids' morphology and nanostructure.

One of the challenging aspects of studying the morphology and nanostructure of multicomponent soft materials, such as the semicrystalline O-I hybrids developed herein, is determining the main crystalline structural parameters. To do so, simultaneous small-angle (SAXS) and wide-angle (WAXS) X-ray scattering are widely used techniques. In multicomponent systems, WAXS allows the assignment of melting and crystallization events to each component, as well as the determination of the mass degree of crystallinity (χ_{WAXS}). Conversely, SAXS allows the quantification of nanometric parameters, such as the long period (L), the lamellar and interlamellar thicknesses (l_c and l_a, respectively) determination, as well as the linear degree of crystallinity (χ_{SAXS})

calculation. Therefore, SAXS and WAXS combination in simultaneous temperature-dependent experiments is a valuable alternative to fully comprehend the crystalline behaviour of complex and/or multicomponent systems.

In the case of samples that combine PCL and PEG, with some exceptions[28], SAXS results usually show a single correlation distance (i.e. long period), which is generally attributed to a global crystalline ordering that comprises both PCL and PEG, while WAXS results show the occurrence of distinct PCL and PEG crystalline phases. One possible explanation for this phenomenon is given by Xue et al. [46] and He et al. [127]: an alternating crystalline-crystalline structure (see Figure 3; section 1.1). Another possibility to explain this behaviour is to consider these multicomponent systems as biphasic, due to the lack of electron density contrast between the PCL and PEG moieties in both the crystalline and amorphous regions [30]. Nevertheless, the most widely accepted explanation in block copolymer systems for the single lamellar peak in SAXS experiments is that, even though PCL and PEG crystallize separately, sometimes even in physically separated domains, a templating effect in which PEG crystallizes with the same lamellae thickness as the already crystallized PCL, might be observed [42]. However, it is noteworthy to mention that PCL and PEG crystallization behaviour in cross-linked matrices might also be strikingly distinct from the crystallization behaviour within blend or copolymer systems due to the mobility restrictions imposed by the cross-links. Nevertheless, few studies are available on the subject due to the increased complexity attributed to cross-linking. This is yet another reason why the thermal behaviour of the semicrystalline O-I hybrids investigated herein are relevant.

In order to correctly interpret the semicrystalline O-I hybrids' thermal behaviour from the temperature-dependent SAXS/WAXS experiments, it is important to keep in mind some of the results found in sections 4.1 and 4.2.1, which are summarized below:

- **DSC (Figure 28)**: O-I hybrids made up of high M_w prepolymers are semicrystalline. Ternary PCL_{39}-PEG_{39}/SS_{22} O-I hybrid nanocomposite showed two distinct melting and crystallization peaks, which indicates that both PCL and PEG are semicrystalline.

- **TEM (Figure 34)**: ternary PCL_{39}-PEG_{39}/SS_{22} O-I hybrid nanocomposite showed microscopic phase separation. The morphological comparison with the binary PCL_{80}/SS_{20} and PEG_{75}/SS_{25} samples, allowed to attribute each phase of the ternary PCL_{39}-PEG_{39}/SS_{22} sample to either PCL/SS or PEG/SS.

- ESI-TEM (Figure 36): high M_w random polysilsesquioxane nanoparticles were present on both PCL_{39}-PEG_{39}/SS_{22} phases as well as on both PCL_{80}/SS_{20} and PEG_{75}/SS_{25} binary O-I hybrids.

- **Solid-state ^{29}Si NMR (Figure 26)**: semicrystalline O-I hybrids, analogously to the amorphous O-I hybrids, show two distinct silsesquioxane structures.

- **Soxhlet extraction (Table 4)**: at least 2/3 of the triethoxysilyl chain ends are effectively condensated into Si-O-Si bridges, which is in agreement with the condensation yields calculated from solid-state ^{29}Si NMR.

- **X-ray scattering (Figure 44)**: amorphous O-I hybrids showed a complex four-phase nanostructure, elucidated in da Silva et al.[111], in which PCL and PEG are indistinctly cross-linked by low M_w silsesquioxane cages, forming grains of a gel-like network that are collapsed together to form the matrix. Throughout the homogeneous gel-like matrix, unbound PCL and/or PEG, as well as high M_w random polysilsesquioxane nanoparticles are uniformly distributed.

In summary, these results point out to the conclusion that semicrystalline O-I hybrids showed the same four-phased nanostructure found for the amorphous O-I hybrids, with the addition of the crystalline phase(s) and microscopic phase separation (in the case of the ternary PCL_{39}-PEG_{39}/SS_{22}). Another noteworthy information is that, if on the amorphous O-I hybrids, the silsesquioxane moiety, accounts for approximately 40 wt.% of the sample, in the semicrystalline O-I hybrids, the silsesquioxane moiety accounts for approximately 15 wt.% of the sample. Therefore, the organic moiety, which is the crystallizable moiety, is the majority and the crystalline phase should play a significant role in the overall morphology.

Finally, it is also necessary to carefully consider the O-I hybrids formation process in order to correctly interpret the temperature-dependent SAXS/WAXS experiments. Solvent-free syntheses require that the organic prepolymers are molten at all times. In this work, after the organic prepolymer´s chain ends modification by the addition of the triethoxysilyl groups, hydrolysis-condensation (i.e. curing), samples were left to cool naturally. During the 2 hours annealing time, most of the ethoxy groups had already been effectively hydrolysed into silanol groups (see Figure 7). However, even though most of silanol condensation into Si-O-Si cross-links and silsesquioxane structures had also already occurred during the natural cooling process, Si-O-Si condensation was still an important process.

If, on the one hand, during hydrolysis-condensation at 90°C the organic polymers were melted, on the other hand, during natural cooling, PCL and PEG crystallization competed with the

residual condensation. Moreover, for the semicrystalline ternary PCL_{39}-PEG_{39}/SS_{22} O-I hybrid sample, the PCL/PEG phase separation is yet another competing process. Possibly, at 90 °C the PCL and PEG phase separation was the dominant process, since the silsesquioxane structures formed at both microscopic phases (PCL/SS and PEG/SS) did not suffer with the other phase influence.

Figure 46 and Figure 47 show the evolution of the SAXS and WAXS profiles, respectively, as a function of time (and temperature) in three-dimensional (left) and contour (right) plots for the binary PCL_{80}/SS_{20} (top), PEG_{75}/SS_{25} (bottom) and the ternary PCL_{39}-PEG_{39}/SS_{22} (middle) semicrystalline O-I hybrid nanocomposites. Contour plots show intensity in the colour scale, while the main temperatures are indicated on the left Y-axis. To highlight the morphology distinctions prior to (as prepared) and after recrystallization, Figure 48 shows a representative SAXS (left) curve and a representative WAXS curve (right) for each sample. As prepared samples are shown on the top, while recrystallized samples (after the heating and cooling experiment) are shown on the bottom.

In the WAXS region, the characteristic crystalline peaks for both PCL and PEG are found. Moreover, both PCL and PEG characteristic crystalline peaks are present within the PCL_{39}-PEG_{39}/SS_{22} O-I hybrid, indicating that a double crystallization process, rather than a co-crystallization process, occurs [128]. In all cases, peaks centred at the 15.2, 15.6 and 16.8 nm^{-1} q-values are attributed to the (110) (111) and (200) PCL crystalline planes and correspond, respectively, to the 4.1, 4.0 and 3.7 Å d_{Bragg} [129]. Conversely, PEG crystalline planes are centred at the 13.7 nm^{-1} (d_{Bragg}≈ 3.8 Å) and 16.6 nm^{-1} (d_{Bragg}≈ 4.5 Å) are attributed respectively to the (120) plane and a superposition of several planes [130]. Possibly, the increased FWHM after recrystallization, which was verified in all cases, is responsible for the overlap of the 15.2 nm^{-1} and 15.6 nm^{-1} PCL peaks at the binary PCL_{80}/SS_{20} sample, which resulted in the latter being unresolved.

There are three distinct regions in the SAXS data. Region I shows a monotonic intensity decrease, whereas region III shows a broad peak. Both features are attributed to the gel-like morphology shown in the amorphous O-I hybrids (see Figure 39). The high intensity peaks found in region II are attributed to the PCL and PEG semicrystalline morphology. Analogously to the amorphous O-I hybrids, the q_{max} and FHWM values found for the broad peak in region III provided the correlation distance in between silsesquioxane cages as well as the average size of the gel-like grains. Conversely, from the high intensity peaks found in region II, a one-dimensional correlation function was calculated (see Equation 14), providing average values of L, l_a and l_c.

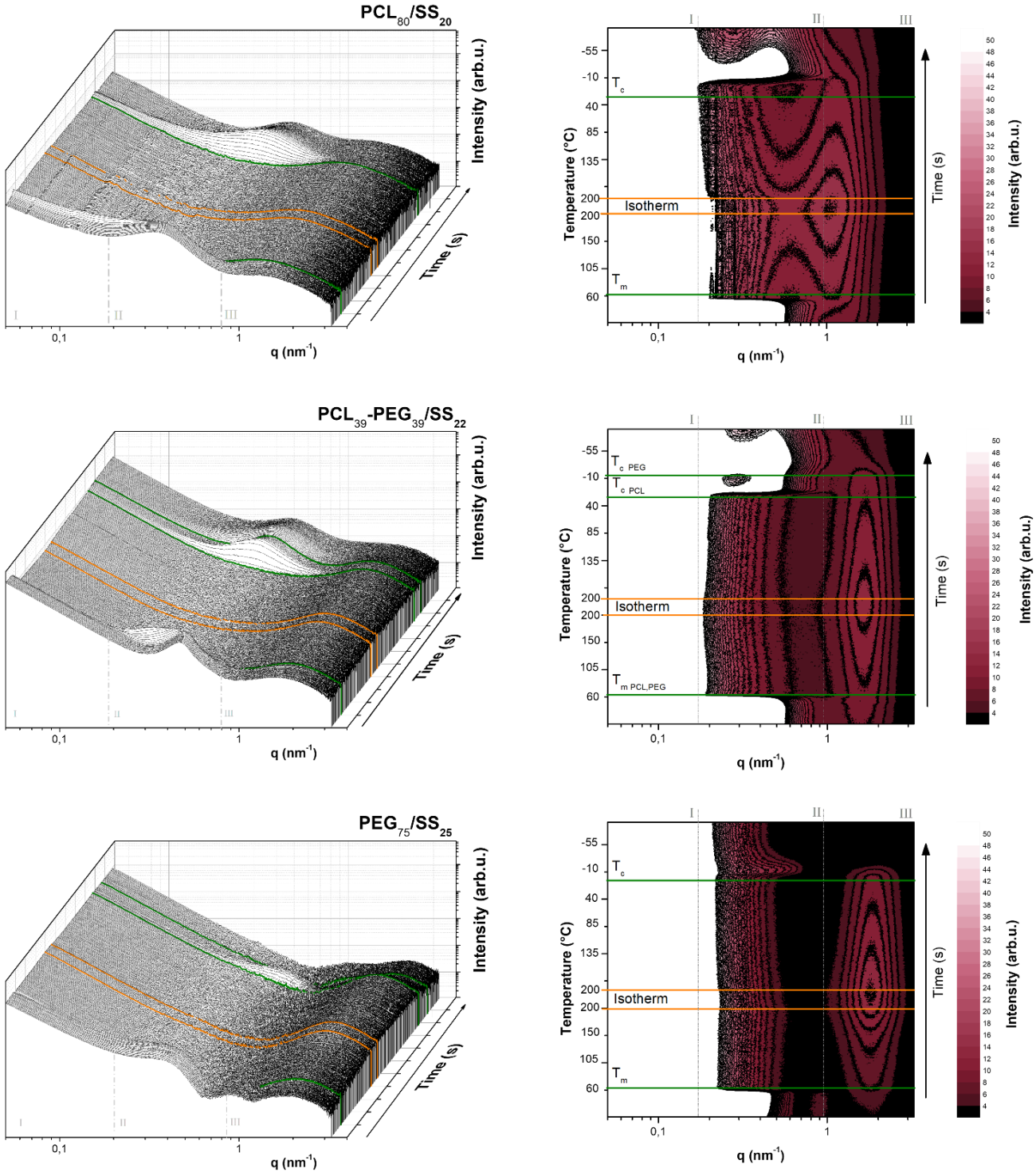

Figure 46 – Three-dimensional (left) and contour (right) plots showing the evolution of PCL_{80}/SS_{20} (top); PCL_{39}-PEG_{39}/SS_{22} (middle) and PEG_{75}/SS_{25} (bottom) semicrystalline O-I hybrid nanocomposites' SAXS curves as a function of time. Green lines are used to mark specific thermal events. Orange lines are used to mark the isotherm interval.

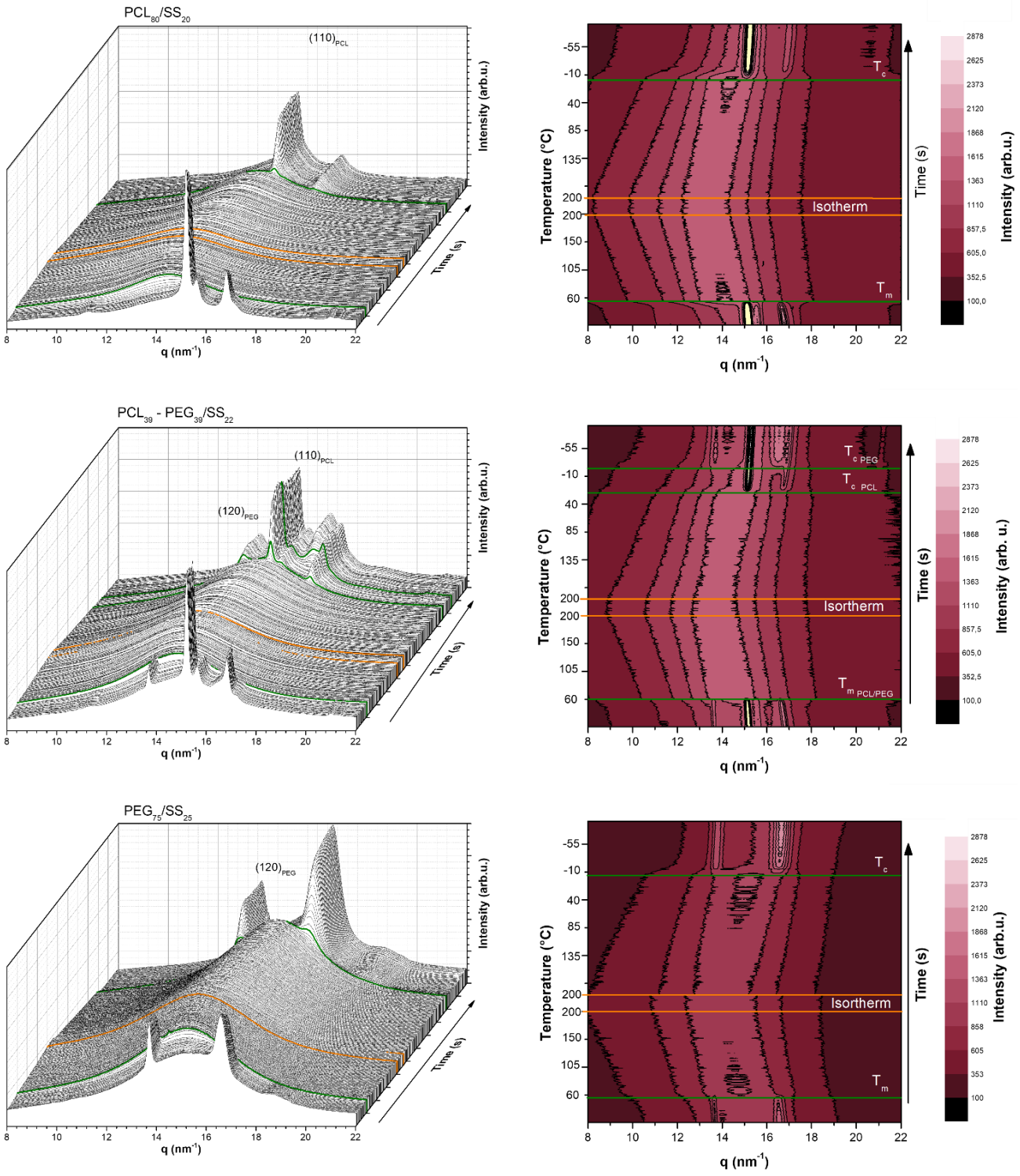

Figure 47 - Three-dimensional (left) and contour (bottom) plots showing the evolution of PCL_{80}/SS_{20} (top); PCL_{39}-PEG_{39}/SS_{22} (middle) and PEG_{75}/SS_{25} (bottom) semicrystalline O-I hybrid nanocomposites' WAXS curves as a function of time. Green lines are used to mark specific thermal events while the orange lines are used to mark the isotherm interval.

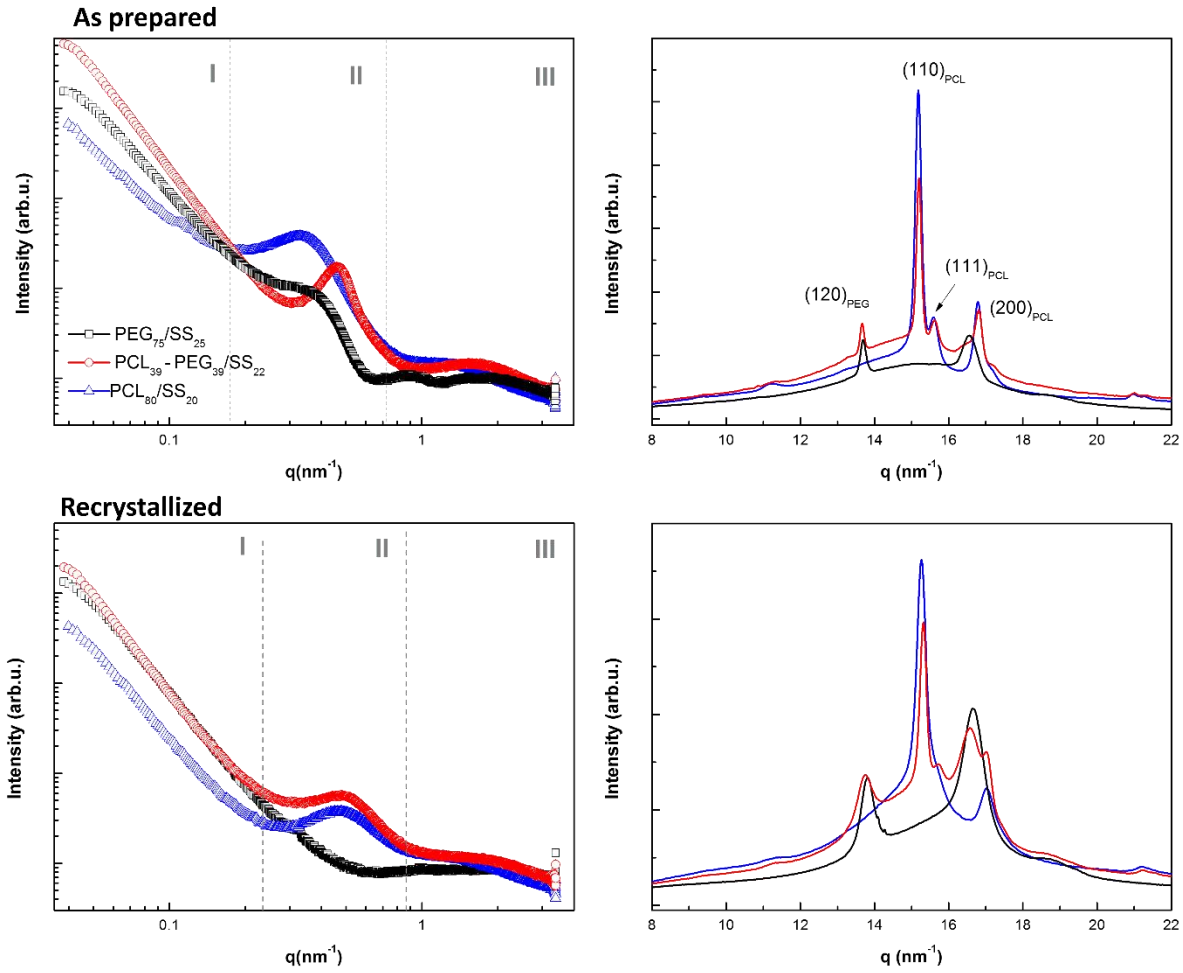

Figure 48 – SAXS (left) and WAXS (right) representative curves of the as prepared (top) and recrystallized (bottom) semicrystalline O-I hybrid nanocomposites. Crystallographic planes are indicated on the WAXS curves.

Figure 49 shows the one-dimensional correlation functions obtained in the complete time/temperature scan of the X-ray scattering experiments. The one-dimensional correlation curves were calculated from the high intensity peaks in the SAXS region II having the scattering intensity related to silsesquioxane structures removed (see section 3.3.13). The qualitative analysis of the correlation function shows that, in all cases, it is valid to approximate these multicomponent systems to a biphasic model. It is interesting to highlight that neither during melting (left) nor during recrystallization (right) the first maximum position, which gives the L values, shows linear variations in the PCL_{39}-PEG_{39}/SS_{22} sample. This is a clear evidence that, even though the biphasic model fits well, the single peak in the ternary O-I hybrid in the SAXS region II is actually a superposition of distinct peaks related to two distinct semicrystalline structures. As a consequence, the crystalline parameters calculated from these correlation functions for the ternary O-I hybrid samples are

actually an average of the crystalline parameters of the semicrystalline PCL within the PCL/SS phase and the crystalline parameters of the semicrystalline PEG within the PEG/SS phase.

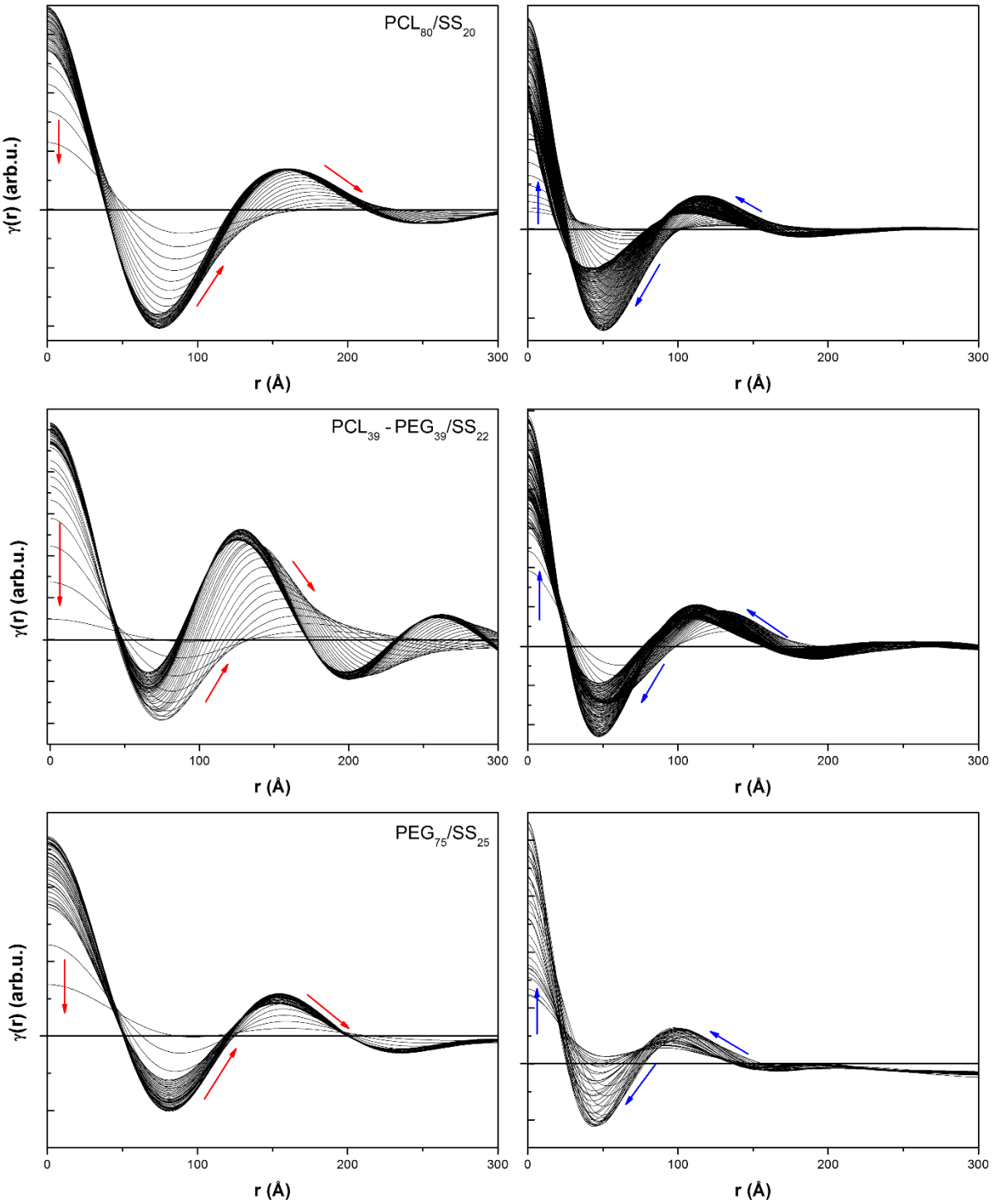

Figure 49 - Correlation functions obtained of the PCL_{80}/SS_{20} (top); PCL_{39}-PEG_{39}/SS_{22} (middle) and PEG_{75}/SS_{25} (bottom) semicrystalline O-I hybrid nanocomposites. As prepared samples are shown on the left, in which the red arrows indicate increasing temperature effect. Recrystallized samples are shown on the right, in which the blue arrows indicate decreasing temperature effect.

Figure 50 shows the evolution over time of the lamellar parameters calculated for all samples. Table 7 shows the lamellar parameter values for the as prepared and recrystallized samples obtained from the one-dimensional correlation functions, shown in Figure 49. The as prepared binary PCL_{80}/SS_{20} and PEG_{75}/SS_{25} O-I hybrids showed a lamellar arrangement similar to the commonly reported in literature for neat PCL or PEG homopolymers (L≈ 16 nm; l_c ≈ 6 nm) [30]. This is due to the fact that a competition between Si-O-Si condensation and polymer crystallization, during the O-I hybrid formation, associated with the low cross-linking density (as shown earlier by the T_g results of Table 4) allowed the organic moieties to mostly behave as free. Conversely, significant decrease in both L and l_c were observed in both cases, upon recrystallization. This is mainly due to the complete formation of the silsesquioxane structures (gel-like grains and nanoparticles) that not only restricted the mobility of the polymeric chains, but also promoted a steric hindrance to the crystal growth. The absence of annealing treatment on the recrystallized samples can also influence the smaller l_c values found.

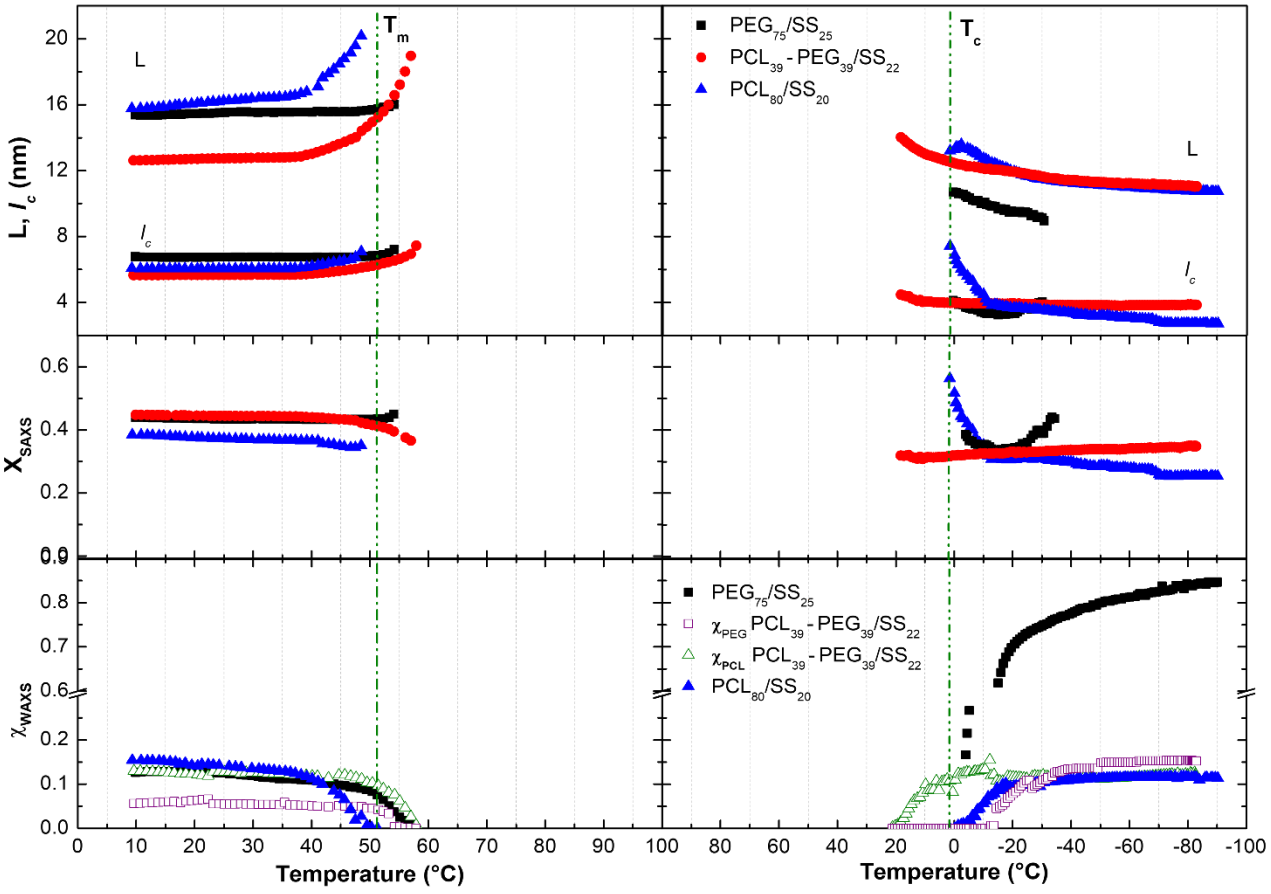

Figure 50 – Lamellar parameters and degrees of crystallinity, obtained from the simultaneous SAXS/WAXS temperature-dependent experiments. Green lines indicate PCL melting and crystallization temperatures in the PCL_{80}/SS_{20} sample. χ_{PCL} and χ_{PEG} denote the PCL and PEG phase contributions, respectively, to the overall χ_{WAXS} of the PCL_{39}-PEG_{39}/SS_{22} sample.

Table 7 – Lamellar and silsesquioxane structural parameters calculated by SAXS for both the as prepared and recrystallized semicrystalline O-I hybrid nanocomposites. Mass degree of crystallinity (χ_{WAXS}), T_m and T_c onset values were obtained from WAXS data and are added as reference.

Sample	As prepared							
	Peak II						Peak III	
	l_c (nm)	l_a (nm)	L (nm)	X_{SAXS}	T_m^*(°C)	χ_{WAXS}	d_s (nm)	L_c (nm)
PCL_{80}/SS_{20}	6.0	10.5	16.5	0.38	29	0.15	3.9	7.7
PCL_{39}-PEG_{39}/SS_{22}	5.6	7.7	13.3	0.45	25	0.18	3.2	7.7
PEG_{75}/SS_{25}	6.7	10.2	16.9	0.44	23	0.09	2.8	7.0
Sample	**Recrystallized**							
	Peak II						Peak III	
	l_c (nm)	l_a (nm)	L (nm)	X_{SAXS}	T_c^* (°C)	χ_{WAXS}	d_s(nm)	L_c (nm)
PCL_{80}/SS_{20}	3.6	7.7	11.3	0.25	4	0.11	3.4	6.5
PCL_{39}-PEG_{39}/SS_{22}	3.8	7.6	11.4	0.34	$21^{\dagger}$/-15^{F}	0.27	2.9	7.0
PEG_{75}/SS_{25}	3.3	9.4	12.7		3	0.87	2.4	7.0

*WAXS Onset temperatures. † value refers to the PCL phase. ^{F} value refers to the PEG phase.

Interestingly, the as prepared ternary PCL_{39}-PEG_{39}/SS_{22} O-I hybrid nanocomposite showed L and l_c values significantly smaller than the binary PCL_{80}/SS_{20} and PEG_{75}/SS_{25} samples. Possibly this is due to the occurrence of phase separation, which decreased the mobility of the polymer chains during O-I hybrid formation. As it is clearly observed from the WAXS data in Figure 50 (bottom), PCL and PEG melted simultaneously at approximately 50°C but crystallized separately at 21 °C and -15 °C respectively. Therefore, in the recrystallized sample, it is possible to separate the PCL and PEG L-value contributions. During crystallization, initially a 12.1 nm long period was found from the one-dimensional correlation functions of the PCL_{39}-PEG_{39}/SS_{22}, sample. This can safely be attributed to PCL, based on the WAXS results. When PEG crystallizes, an average long period of 11.4 nm was found. Based on the knowledge of the PCL long period and the mass fractions of the PCL and PEG phases, an approximate 10.7 nm L-value can be estimated for the recrystallized PEG. This result could suggest that the commonly reported templating effect of the PCL crystalline phase over PEG crystallization was not observed herein.

Table 7 also shows the onset melting and crystallization temperatures as well as the linear (χ_{SAXS}) and mass (χ_{WAXS}) degrees of crystallinity. In terms of temperatures, the binary O-I hybrids showed smaller melting temperatures (T_m) than the commonly reported for both PCL (≈ 60°C) and PEG (≈ 50°C) homopolymers (see section 1.1). Conversely, the crystallization

temperatures (T_c) were significantly reduced in comparison with PCL (≈ 35°C) and PEG (≈ 45°C) homopolymers. These results are in agreement with the L and l_c findings and highlight the effect of cross-linking on chain mobility. If we compare melting and crystallization temperatures of the ternary O-I hybrid with the PCL and PEG homopolymers, or even PCL/PEG blends [130,131], the direct conclusions that could be drawn is that ternary O-I hybrids are, in fact, cross-linked. However, by comparing PCL T_c in the ternary O-I hybrid with the PCL T_c in the binary PCL_{80}/SS_{20} sample, an obvious nucleation effect is observed, since PCL T_c at the ternary sample is much higher, at 21 °C. This phenomenon was also verified by DSC (see Figure 28). Nevertheless, it is unprecedented in literature. Possibly this could be due to a nucleation effect promoted by the interface. The possibility of interface nucleation in immiscible polymer blends has already been theoretically proven by Ma et al. [132]. Nevertheless, it was never reported in PCL/PEG systems. In their work, Ma et al. [132] attribute the interface nucleation to local polymer dilution at diffuse interfaces, which is the case herein due to the cross-linking.

In terms of degrees of crystallinity, χ_{SAXS} and χ_{WAXS} have distinct physical meanings. As it can be observed in Table 7, χ_{SAXS} is usually higher than χ_{WAXS}, due to the fact that the SAXS model does not take into consideration the amorphous polymer outside the lamellar arrangement (i.e. interfibrillar and interspherulitic, see Figure 16) [93]. The PCL χ_{WAXS} values are fairly unchanged at both the binary and the ternary O-I hybrid nanocomposites and revolves around 0.15. To further investigate the matter, Figure 51 shows the behaviour of the quantity Q_{II} plotted against χ_{WAXS} for the binary PCL_{80}/SS_{20} (top) and PEG_{75}/SS_{25} (bottom) and the ternary PCL_{39}-PEG_{39}/SS_{22} O-I hybrid nanocomposites. As shown in Equation 29, Q_{II}, is a fraction of the invariant, Q:

$$Q = Q_I + Q_{II} + Q_{III} \approx Q_{II} + Q_{III} \qquad \text{Equation 29}$$

where Q_I accounts for the region I contribution, Q_{II} accounts for the contribution of the high intensity peak in SAXS region II and Q_{III} accounts for contribution of the broad peak in SAXS region III.

In the case of PCL_{80}/SS_{20}, Q_{II} (closed symbols) behaves as in a typical semicrystalline biphasic polymer: initially increasing during melting, due to the early melting of thinner lamellae. A peak is observed when the crystalline and amorphous lamellae thicknesses become equal, due to contrast inversion [93]. The same is also true for recrystallization. Initially, χ_{WAXS} (open symbols) and Q_{II} grow parallel, then contrast inversion occurred and Q_{II} starts do decrease while χ_{WAXS} reaches a

plateau. PCL_{80}/SS_{20} showed approximately the same degree of crystallinity on both thermal events while Q_{II} maximum value is approximately half after recrystallization.

The Q_{II} χ_{WAXS} quantities in PEG_{75}/SS_{25} followed the same behaviour as in PCL_{80}/SS_{20}. However, after recrystallization, χ_{WAXS} is surprisingly high, reaching 0.87, while Q_{II} reaches zero. Q_{II} behaviour can be understood due to the absence of a peak in region II (see Figure 48), which means that the dominant crystalline/amorphous lamellar structure observed in the as prepared PEG_{75}/SS_{25} sample is lost after recrystallization. Cheng et al. [48] have showed that PEG homopolymer in the 1 000 to 5 0000 g mol^{-1} M_w range (polydispersity revolves around 1.05) is prone to the formation of an almost completely crystalline material with multiple lamellar thicknesses. The latter occur due to the non-integral folding of the chains within the lamellae. It is noteworthy to mention that silsesquioxane cages attached to the polymer chain ends can favour PEG non-integral folding. As a result, it is possible that scattering curves could show one or multiple peaks, however at the end of region II q-range and possibly overlapping with the silsesquioxane broad peak in region III.

Finally, in order to thoroughly investigate the PCL_{39}-PEG_{39}/SS_{22} behaviour, it is interesting to separate the individual PCL and PEG contributions to the total degree of crystallinity, χ_{WAXS} (see Equation 24 and Figure 22), as shown in Figure 51 (middle). As already mentioned, during the melting of the as prepared samples, χ_{WAXS} and Q_{II} behaviours for both semicrystalline PCL and PEG structures within the ternary O-I hybrid is analogous to their behaviour in the binary O-I hybrids. Moreover, PCL and PEG melted simultaneously. Conversely, upon recrystallization, initially PCL crystallized and, therefore, χ_{WAXS} and Q_{II} grew until the contrast inversion, when Q_{II} started to decrease and χ_{WAXS} as well as χ_{PCL} reached a plateau[91]. Afterwards, when PCL crystallization was finished, PEG started to crystallize and χ_{WAXS} and Q_{II} grew again, until it reached a new contrast inversion point. From then on, χ_{WAXS} reached a new plateau in which χ_{PEG} reached maximum. From this point on Q_{II} decreases.

After recrystallization, Q_{II} value is also significantly smaller than Q_{II} for the as prepared ternary O-I hybrid in comparison with the binary semicrystalline O-I hybrids. However, χ_{WAXS} is significantly higher. χ_{WAXS} increase is due to the 3-fold increase in PEG degree of crystallinity (in comparison with the as prepared PCL_{39}-PEG_{39}/SS_{22} sample), since PCL degree of crystallinity remained unchanged. It is noteworthy to mention that in spite of the 3-fold increase, PEG degree of crystallinity is significantly smaller than χ_{WAXS} for the recrystallized PEG_{75}/SS_{25}. In block copolymers, the suppression of PEG crystallization is usually related with confinement effects, which in this case

could be due to phase separation [36]. In summary, the analysis performed in this section showed that even though PCL/SS and PEG/SS phases are segregated at the ternary O-I hybrid nanocomposite, they have a strong influence on each other's thermal and morphological behaviour.

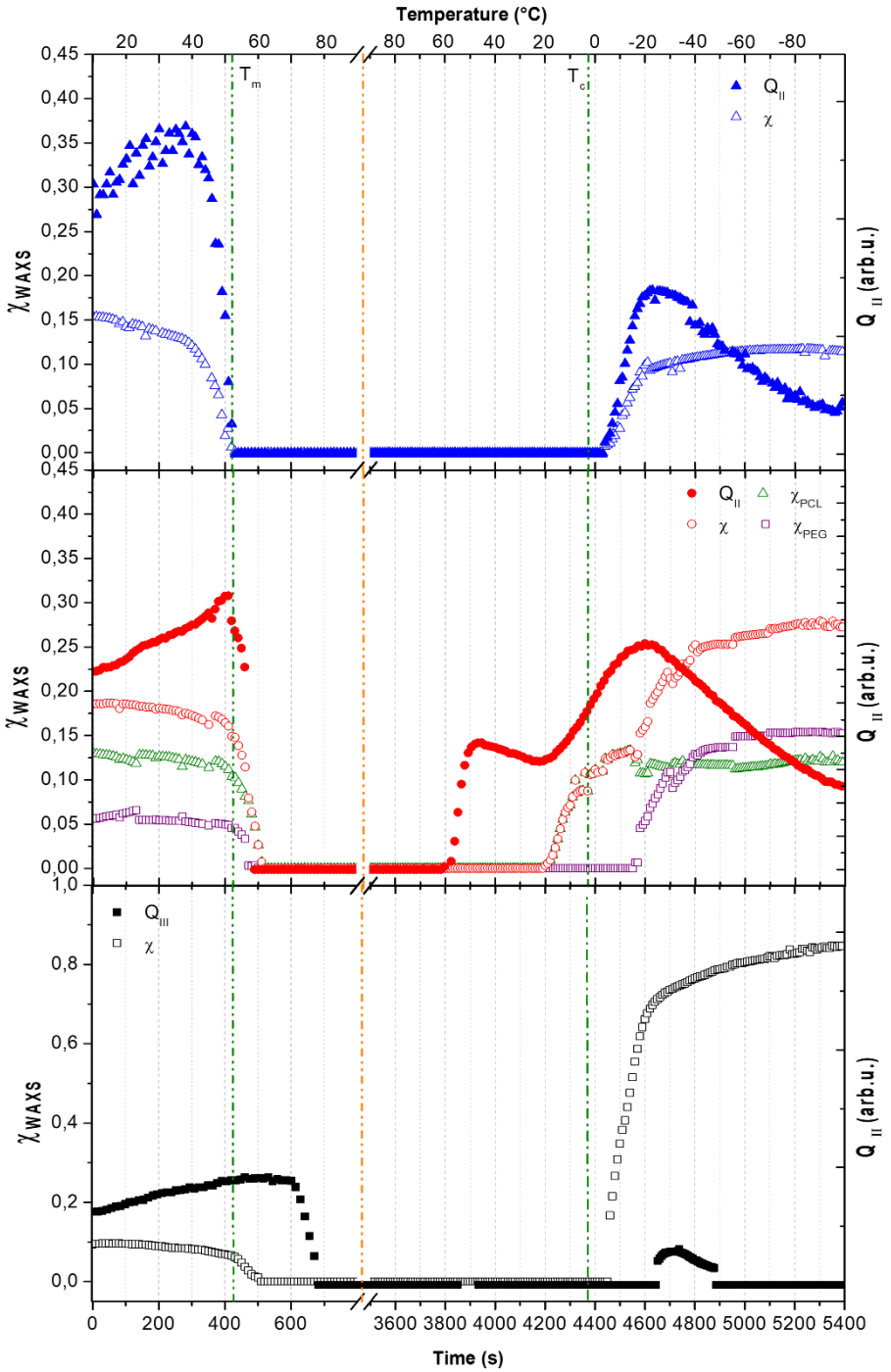

Figure 51 - Time dependence of the degree of crystallinity obtained by WAXS (χ_{WAXS}, left axis) and the region II invariant (Q_{II}, right axis) of the semicrystalline O-I hybrid nanocomposites. PCL_{80}/SS_{20}, PCL_{39}-PEG_{39}/SS_{22} and PEG_{75}/SS_{25} are shown on the top, middle and bottom, respectively. Green lines indicate the PCL_{80}/SS_{20} offset melting (T_m) and crystallization onset (T_c) temperatures while orange line shows the limit between heating and cooling runs.

Let us now turn the focus to the silsesquioxane structures and their dependency with thermal events. As already discussed in section 4.2.1, peak III can be assigned to the correlation distance, d_s, in between silsesquioxane cages, or else, to the folded chain length in between silsesquioxane nodes, (see Figure 44). Figure 52 shows the d_s evolution over time and temperature, while Figure 53 shows the dependency of the L_c parameter (size estimation of the gel-like domains, Equation 10). Average d_s and L_c values prior to melting in the as prepared samples and after recrystallization are also shown in Table 7.

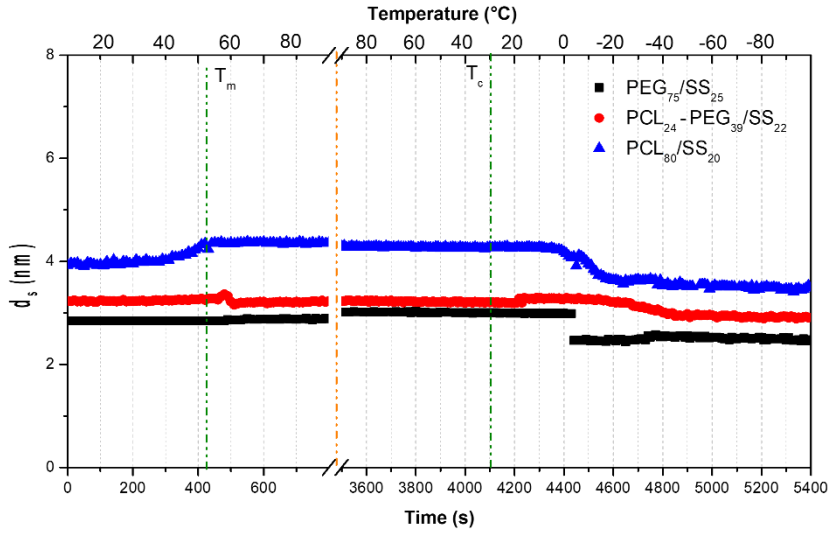

Figure 52 - Evolution of the correlation distance, d_s, as a function of time in the SAXS temperature-dependent experiments. Green lines indicate the PCL_{80}/SS_{20} offset melting (T_m) and crystallization onset (T_c) temperatures while orange line shows the limit between heating and cooling runs.

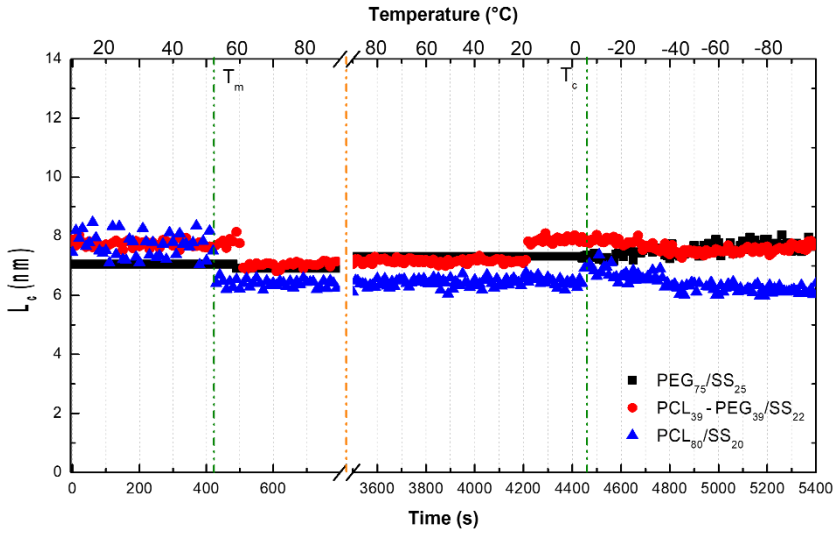

Figure 53 – Evolution of the length of coherence, L_c, as a function of time in the SAXS temperature-dependent experiments. Green lines indicate the PCL_{80}/SS_{20} offset melting (T_m) and crystallization onset (T_c) temperatures while orange line shows the limit between heating and cooling runs.

On average, PCL_{80}/SS_{20} d_s was 3.9 nm in the as prepared state, 4.4 nm at the amorphous state and 3.4 nm in the recrystallized state. Moreover, PCL_{80}/SS_{20} showed 7.7 nm gel-like grains that contracted to 6.5 nm in the recrystallized state. In contrast, PEG_{75}/SS_{25} d_s was found to be 2.8 nm during melting and at the amorphous state, while after recrystallization it was found to slightly decrease to 2.4 nm. PEG_{75}/SS_{25} showed gel-like grains of approximately 7.0 nm in diameter, irrespective of the presence of a crystalline phase. At last, PCL_{39}-PEG_{39}/SS_{22} d_s was found to be 3.2 nm in the as prepared and molten states and decreased up to 2.9 nm in the recrystallized state. Finally, the ternary PCL_{39}-PEG_{39}/SS_{22} sample initially showed 7.7 nm gel-like grains that contracted to 7.0 nm after recrystallization.

On the one hand, d_s results are in agreement with the amorphous O-I hybrids results (see section 4.2.1) since, irrespective of temperature, d_s increased as a function of PCL weight ratio within the O-I hybrid nanocomposites. As mentioned earlier, this is due to the increased M_w in between silsesquioxane nodes. The analysis of d_s values at both the amorphous and the semicrystalline O-I hybrids show that even though there is a linear relationship between d_s and the organic moiety composition, a non-linear relationship is observed between d_s and the organic prepolymer M_w, since a 4-fold increase in M_w only promoted a 50% d_s increment. This conclusion is valid for all three samples and could indicate that the linear relationship with PCL weight ratio was actually due to the overall hydrophobic character of the sample, rather than molecular weight.

On the other hand, the L_c results do not correlate with the amorphous O-I hybrids results. Amorphous O-I hybrids showed L_c values equivalent to 3 times the d_s values, while semicrystalline O-I hybrids, showed L_c values equivalent to approximately 2 times the d_s values. Moreover, the amorphous ternary O-I hybrids, L_c values were always smaller than the amorphous binary O-I hybrids L_c values, which is not true for the semicrystalline O-I hybrids. These results show that grain size does not seem to directly correlate with neither d_s nor the organic prepolymer M_w. Possibly, this could be due to the organic chain in between the silsesquioxane cages being expelled from the gel-like network structure to form the lamellar crystalline arrangement. Finally, it is noteworthy to mention that the crystalline phase had an influence on the gel-like grain size.

In the molten state, d_s and L_c do not change with temperature, which is in agreement with the amorphous O-I hybrids results. Let us now look at the invariant, Q, behaviour as a function of temperature. It is important to remember that the amorphous O-I hybrids showed a reversible temperature-dependent Q-value behaviour (see Figure 45) which could be of benefit to potential

biomedical applications. Figure 54 shows the evolution over time and temperature of Q_{III} (see Equation 29), which is analogous to Q^{exp} in section 4.2.1. As it may be observed, abrupt changes in peak Q_{III} occur when the number of phases changes, due to either the melting or the crystallization processes. This is a consequence of the distinct overall sample scattering power from the crystalline and the amorphous states. Nevertheless, it is noteworthy to mention that PEG_{75}/SS_{25} sample shows smoother scattering power variations, since Q_{III} discontinuity is not observed.

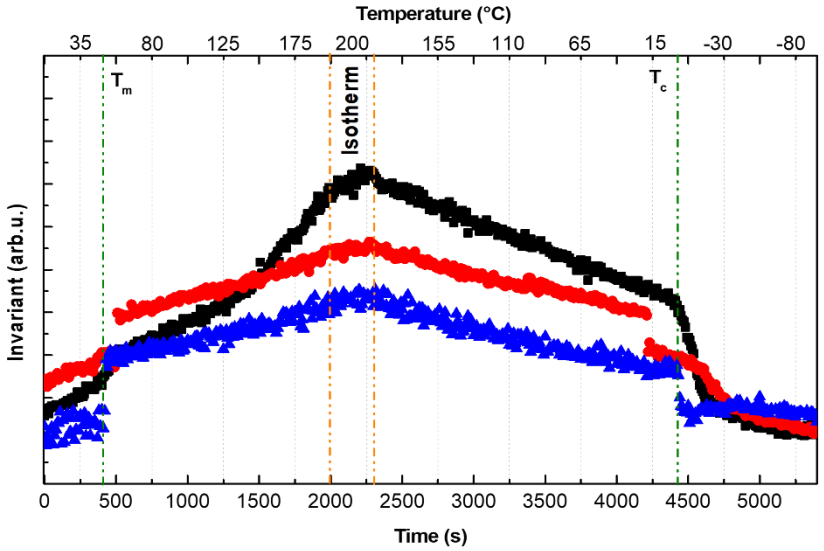

Figure 54 – Evolution of the peak III invariant (Q_{III}) as a function of time in the SAXS temperature-dependent experiments. Green lines indicate the PCL_{80}/SS_{20} offset melting (T_m) and crystallization onset (T_c) temperatures while orange line shows the limit between heating and cooling runs.

At the amorphous state, both PCL_{80}/SS_{20} and PCL_{39}-PEG_{39}/SS_{22} samples show linear Q_{III} variation upon both heating and cooling, while in the PEG_{75}/SS_{25} sample, linear behaviour is only observed upon cooling, even though Q_{III} is also temperature-dependent during heating. The reversible Q behaviour with temperature, generally observed for all samples might be either due to volumetric fraction variations or to contrast changes. Based on the fact that both d_s and L_c are unchanged upon heating and cooling of the amorphous samples, it is possible to assume that the volumetric fractions are constant. Therefore, Q temperature-dependency might only be due to contrast variations. Possibly, contrast variation is a result of increased Si-O-Si bond vibrations due to heating, which leads to variations in electronic densities.

The linear behaviour as a function of temperature shown for both PCL_{80}/SS_{20} and PCL_{39}-PEG_{39}/SS_{22} at the amorphous state is an evidence that silsesquioxane structures were stable and did not undergo further condensation. However, it is important to remember that PCL_{39}-PEG_{39}/SS_{22} sample is in fact, heterogeneous, since PCL/SS and PEG/SS phases are physically

separated (see Figure 34). Conversely, the non-linear PEG_{75}/SS_{25} behaviour upon heating is an indication that residual condensation might occur in this sample, though locally, since no changes in d_s or L_C are observed. To support this assumption, it is important to bring out the fact that PEG_{75}/SS_{25} showed an additional anomalous peak at the SAXS curves (see Figure 46) which is related to distinct chain folding lengths, that led to diverse PEG long periods and therefore to a heterogeneous microenvironment [28,48]. Heterogeneity results in unstable silsesquioxane structures which further condensate upon heating in order to reach their most thermodynamically stable conformation.

As a general result, in terms of morphology and nanostructure, it is possible to conclude that the semicrystalline O-I hybrids are governed by a semicrystalline lamellar morphology frequently observed in spherulitic arrangements, since the organic cross-linked polymer is the major volumetric fraction. Nevertheless, gel-like grains do, in fact, occur and might be located at the interlamellar amorphous regions as well as the extralamellar regions. High M_w silsesquioxane nanoparticles are mainly located at the interfibrillar and interspherulitic amorphous regions. A model to graphically represent semicrystalline O-I hybrids' structure is shown in Figure 55. Moreover, at the ternary O-I hybrid, even though phase separation occurs, PCL and PEG showed a strong influence on their mutual thermal and morphological properties which is unreported for similar blends, copolymers and cross-linked systems.

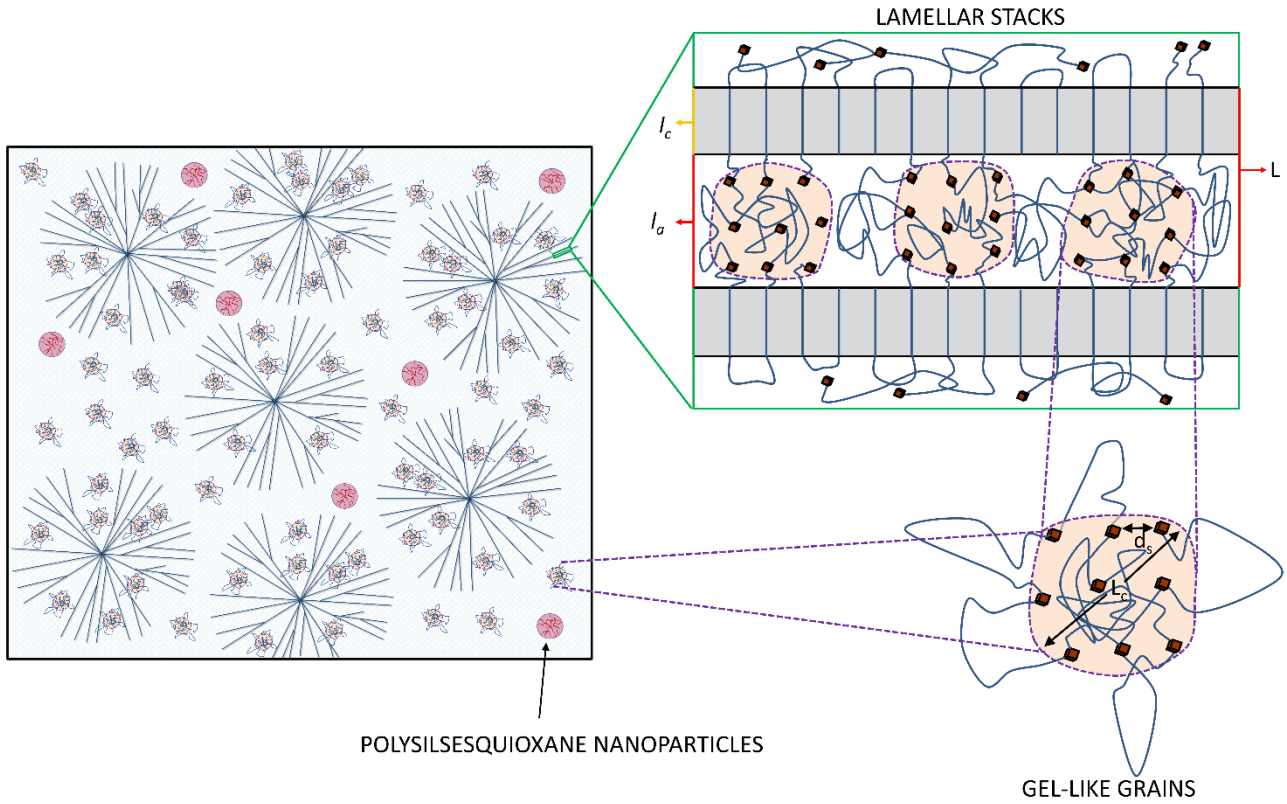

Figure 55 - Schematic representation of the morphology and nanostructure of the semicrystalline O-I hybrid nanocomposites. Gel-like grains made up of PCL and/or PEG chains cross-linked by silsesquioxane nodes are homogeneously distributed throughout the interlamellar, interspherulitic and interfibrillar amorphous regions of the semicrystalline matrix while polysilsesquioxane nanoparticles are placed outside the lamellar stack.

5

CONCLUSIONS

Laura Caetano Escobar da Silva
INSTITUTE OF CHEMISTRY

5. CONCLUDING REMARKS

The lack of a thorough morphological characterization of O-I hybrid nanocomposites is the major drawback in the development of these materials for biomedical applications. In this work, a solvent-free and atoxic route was used to develop novel ternary O-I hybrid nanocomposites made up of biocompatible components (PCL and PEG). Despite the straightforward solvent-free synthesis and irrespective of the organic prepolymers M_w and composition, the ternary nanocomposites showed a surprisingly high condensation yield and convenient macroscopic properties, such as transparency and water uptake. Moreover, results showed that the organic prepolymers M_w was a determining factor in the occurrence of crystallization.

A detailed morphological and nanostructural characterization, combining advanced structural characterization techniques, of the intrinsically amorphous materials revealed their complex multiphase gel-like morphology. TEM, as well as TGA and solid-state ^{29}Si NMR, showed the occurrence of two distinct silsesquioxane phases: the low M_w silsesquioxane cages, which were at the network nodes, and the high M_w random polysilsesquioxane, which was segregated into spherical nanoparticles observed by ESI-TEM. X-ray scattering showed the presence of gel-like grains, which collapse together to form the matrix. In terms of morphology, intrinsically amorphous O-I hybrids were uniform monoliths with uniformly distributed nanoparticles. Moreover, the results point to the conclusion that PCL and PEG were undistinguishable.

In terms of morphology, the semicrystalline O-I hybrids, which were made up of higher M_w organic prepolymers, resembled the spherulitic morphology of a semicrystalline polymer. Conversely, in terms of nanostructure, results indicated that the silsesquioxane structures followed the same trends as the amorphous O-I hybrids, however with the addition of crystalline phases(s). Possibly the gel-like grains (i.e. domains), containing the low M_w silsesquioxane cages, were mainly located in between the interlamellar amorphous spacing, while the high M_w random polysilsesquioxane nanoparticles were distributed throughout the interfibrillar and interspherulitic amorphous regions.

Simultaneous temperature- and time-dependent SAXS/WAXS experiments were carried out to reveal the crystallization effect over the cross-linked O-I hybrids' nanostructure and showed that the crystalline behaviour of the samples is strikingly distinct comparing the as prepared samples (straight from curing) to the recrystallized samples (after the controlled heating and cooling). This

was a result of the competition between crystallization and Si-O-Si bond formation during O-I hybrid formation. The latter is absent in recrystallization since at this point the silsesquioxane structures were fully formed.

PCL_{39}-PEG_{39}/SS_{22} ternary O-I hybrid nanocomposites showed microscopic phase separation, in which phases were unambiguously attributed to PCL/SS and PEG/SS by means of TEM, EELS and ESI-TEM. However, in spite of PCL and PEG crystalline phases being physically separated (on the microscopic scale), mutual effects on their crystallization behaviour were observed, since PCL suffered from interfacial nucleation and PEG suffered from confinement effects. As a result, PCL crystallization was anticipated by approximately 20 °C in the ternary O-I hybrid, while PEG crystallization was delayed by approximately 12 °C in comparison with the binary PCL_{80}/SS_{20} and PEG_{75}/SS_{25}, semicrystalline O-I hybrid nanocomposites. Finally, both the amorphous and semicrystalline O-I hybrid nanocomposites, irrespective of the organic moiety composition, showed a strong temperature-dependent and reversible scattering power variation, which is a consequence of Si-O-Si vibrations.

In conclusion, the results showed a novel complex nanostructure in which at least four distinct phases are observed. However, in spite of the elevated number of phases and the intricate nanostructure found, results showed that, macroscopically, devices are uniform at the macroscale. The understanding of this complex nanostructure as well as of the temperature and crystallization effects on the overall morphology provides a basis for the development of functional biomedical devices with useful properties, such as enhanced flexibility and transparency, improved cell adhesion, and tailored water uptake and degradation rates.

6

REFERENCES

Laura Caetano Escobar da Silva
INSTITUTE OF CHEMISTRY

6. REFERENCES

1. B. D. Ratner, A. S. Hoffman, F. J. Schoen & L.E. Lemons. *Biomaterials Science - An introduction to materials in medicine*. (Academic Press, 1990).
2. Hunt, J. A., Chen, R., van Veen, T. & Bryan, N. Hydrogels for tissue engineering and regenerative medicine. *J. Mater. Chem. B* **2,** 5319–5338 (2014).
3. Doppalapudi, S., Jain, A., Khan, W. & Domb, A. J. Biodegradable polymers - An overview. *Polym. Adv. Technol.* **25,** 427–435 (2014).
4. Jiao, Y.P. & Cui, F.Z. Surface modification of polyester biomaterials for tissue engineering. *Biomed. Mater.* **2,** R24–R37 (2007).
5. Sai, H. *et al.* Hierarchical porous polymer scaffolds from block copolymers. *Science.* **341,** 530–534 (2013).
6. Roach, P., Eglin, D., Rohde, K. & Perry, C. C. Modern biomaterials: A review - Bulk properties and implications of surface modifications. *J. Mater. Sci. Mater. Med.* **18,** 1263–1277 (2007).
7. Hua, C. & Dong, C.-M. Synthesis, characterization, effect of architecture on crystallization of biodegradable poly(ε-caprolactone)-b-poly(ethylene oxide) copolymers with different arms and nanoparticles thereof. *J. Biomed. Mater. Res. Part A* **82A,** 689–700 (2007).
8. Salim, N. V., Hanley, T. & Guo, Q. Microphase separation through competitive hydrogen bonding in double crystalline diblock copolymer/homopolymer blends. *Macromolecules* **43,** 7695–7704 (2010).
9. Liu, L. *et al.* Surface modification of polycaprolactone membrane via layer-by-layer deposition for promoting blood compatibility. *J. Biomed. Mater. Res. - Part B Appl. Biomater.* **87,** 244–250 (2008).
10. Guarino, V., Guaccio, A., Guarnieri, D., Netti, P. A. & Ambrosio, L. Binary system thermodynamics to control pore architecture of PCL scaffold via temperature-driven phase separation process. *J. Biomater. Appl.* **27,** 241–254 (2012).
11. Xu, H. *et al.* Synergistic anti-glioma effect of a coloaded nano-drug delivery system. *Int. J. Nanomedicine* **12,** 29–40 (2017).
12. Talal, J., Abutbul-Ionita, I., Schlachet, I., Danino, D. & Sosnik, A. Amphiphilic Nanoparticle-in-

Nanoparticle Drug Delivery Systems Exhibiting Cross-Linked Inorganic Rate-Controlling Domains. *Chem. Mater.* **29,** 873–885 (2017).

13. Kamata, H., Akagi, Y., Kayasuga-Kariya, Y., Chung, U. & Sakai, T. 'Nonswellable' hydrogel without mechanical hysteresis. *Science.* **343,** 873–875 (2014).

14. Molina, E. F., Pulcinelli, S. H., Briois, V. & Santilli, C. V. Fine-tuning of a nanostructure, swelling, and drug delivery profile by blending ureasil–PEO and ureasil–PPO hybrids. *Polym. Chem.* **5,** 1897–1904 (2014).

15. Labet, M. & Thielemans, W. Synthesis of polycaprolactone: a review. *Chem. Soc. Rev.* **38,** 3484–3504 (2009).

16. Darensbourg, D. J. & Karroonnirun, O. Ring-opening polymerization of l-lactide and ε-caprolactone utilizing biocompatible zinc catalysts. Random copolymerization of l-lactide and ε-caprolactone. *Macromolecules* **43,** 8880–8886 (2010).

17. Piao, L., Dai, Z., Deng, M., Chen, X. & Jing, X. Synthesis and characterization of PCL/PEG/PCL triblock copolymers by using calcium catalyst. *Polymer (Guildf).* **44,** 2025–2031 (2003).

18. Harris, J. M. Poly(ethylene glycol) chemistry Biotechnical and Biomedical Applications. *J. Chem. Inf. Model.* **53,** (1992).

19. Adamska, K., Voelkel, A. & Berliiska, A. The solubility parameter for biomedical polymers - Application of inverse gas chromatography. *J. Pharm. Biomed. Anal.* **127,** 202–206 (2016).

20. Koleske, J. V. & Lundberg, R. D. Lactone Polymers I. Glass transition temperature of poly(ε-caprolactone) by means of compatible polymer mixtures. *J. Polym. Sci. part A* **7,** 795–807 (1969).

21. Chuang, W. T., Shih, K. S. & Hong, P. Da. Kinetics of phase separation in poly(ε-caprolactone)/poly(ethylene glycol) blends. *J. Polym. Res.* **12,** 197–204 (2005).

22. Cheng, L., Lei, L. & Guo, S. In vitro and in vivo evaluation of praziquantel loaded implants based on PEG/PCL blends. *Int. J. Pharm.* **387,** 129–138 (2010).

23. Chuang, W.T., Jeng, U.S., Sheu, H.S. & Hong, P.D. Competition between phase separation and crystallization in a PCL/PEG polymer blend captured by synchronized SAXS, WAXS, and DSC. *Macromol. Res.* **14,** 45–51 (2006).

24. Fu, S. Z. *et al.* Preparation and properties of nano-hydroxyapatite/PCL-PEG-PCL composite membranes for tissue engineering applications. *J. Biomed. Mater. Res. - Part B Appl.*

Biomater. **97 B,** 74–83 (2011).

25. Park, S. A., Lee, S. H. & Kim, W. Fabrication of hydrogel scaffolds using rapid prototyping for soft tissue engineering. *Macromol. Res.* **19,** 694–698 (2011).

26. Ni, P. *et al.* Injectable thermosensitive PEG-PCL-PEG hydrogel/acellular bone matrix composite for bone regeneration in cranial defects. *Biomaterials* **35,** 236–248 (2014).

27. Dong, J., Yuan, T., Yu, X. T., Jia, L. Y. & Mei, Z. Melting and crystallization behaviors of electrostatic spinning polycaprolactone/polyethylene glycol blends. *High Perform. Polym.* **24,** 441–446 (2012).

28. Li, L. *et al.* Morphology of a highly asymmetric double crystallizable poly (ε-caprolactone- b -ethylene oxide) block copolymer. *J. Chem. Phys.* **126,** 024904 (2007).

29. An, J. H., Kim, H. S., Chung, D. J. & Lee, D. S. Thermal behaviour of poly(ε -caprolactone)-poly(ethylene glycol)-poly (ε -caprolactone) tri-block copolymers. **6,** 715–722 (2001).

30. Jiang, S. *et al.* Study of temperature dependence of crystallisation transitions of a symmetric PEO-PCL diblock copolymer using simultaneous SAXS and WAXS measurements with synchrotron radiation. *Eur. Phys. J. E* **27,** 357–364 (2008).

31. Giacomelli, C. & Borsali, R. Morphology of poly(ethylene oxide)-block-polycaprolatone block copolymer micelles controlled via the preparation method. *Macromol. Symp.* **245–246,** 147–153 (2006).

32. Wang, Y.-X., Robertson, J. L., Spillman, Jr., W. B. & Claus, R. O. Effects of the chemical structure and the surface properties of polymeric biomaterials on their biocompatibility. *Pharm. Res.* **21,** 1362–1373 (2004).

33. Nair, L. S. & Laurencin, C. T. Biodegradable polymers as biomaterials. *Prog. Polym. Sci.* **32,** 762–798 (2007).

34. Bat, E., Zhang, Z., Feijen, J., Grijpma, D. W. & Poot, A. a. Biodegradable elastomers for biomedical applications and regenerative medicine. *Regen. Med.* **9,** 385–98 (2014).

35. Mark, J. E. *Polymer Data Handbook*. (Oxford University Press, 1999). doi:10.1021/ja907879q

36. Zhang, C. *et al.* Preparation of alternating multilayered polyethylene oxide/poly(ε-caprolactone) and the confined crystallization of the composites. *RSC Adv.* **5,** 98999–99007 (2015).

37. Mirhosseini, M. M., Haddadi-Asl, V. & Zargarian, S. S. Fabrication and characterization of hydrophilic poly(ε-caprolactone)/pluronic P123 electrospun fibers. *J. Appl. Polym. Sci.* **133,** 43345 (2016).

38. Zehnder, T., Freund, T., Demir, M., Detsch, R. & Boccaccini, A. R. Fabrication of cell-loaded two-phase 3D constructs for tissue engineering. *Materials (Basel).* **9,** 887 (2016).

39. Hu, H. & Dorset, D. L. Crystal structure of poly(ε-caprolactone). *Macromolecules* **23,** 4604–4607 (1990).

40. Sun, J., Chen, X., He, C. & Jing, X. Morphology and Structure of Single Crystals of Poly(ethylene glycol)-Poly(ε-caprolactone) Diblock Copolymers. *Macromolecules* **39,** 3717–3719 (2006).

41. Qiu, Z., Ikehara, T. & Nishi, T. Miscibility and crystallization of poly(ethylene oxide) and poly (ε-caprolactone) blends. *Polymer (Guildf).* **44,** 3101–3106 (2003).

42. Palacios, J. K., Mugica, A., Zubitur, M. & Muller, A. J. Copolymers and Terpolymers with more than one crystallizable block. in *Crystallization in multiphase polymer systems* (eds. Thomas, S., P., M. A., Gowd, E. B. & Kalarikkal, N.) 123–177 (Elsevier, 2018).

43. Kumar, D. *et al.* Three-dimensional hypoxic culture of human mesenchymal stem cells encapsulated in a photocurable, biodegradable polymer hydrogel: A potential injectable cellular product for nucleus pulposus regeneration. *Acta Biomater.* **10,** 3463–3474 (2014).

44. He, C. *et al.* Formation of a unique crystal morphology for the poly(ethylene glycol)-poly(ε-caprolactone) diblock copolymer. *Biomacromolecules* **7,** 252–258 (2006).

45. Chiang, Y. W., Hu, Y. Y., Li, J. N., Huang, S. H. & Kuo, S. W. Trilayered Single Crystals with Epitaxial Growth in Poly(ethylene oxide)-block-poly(ε-caprolactone)-block-poly(l-lactide) Thin Films. *Macromolecules* **48,** 8526–8533 (2015).

46. Xue, F. F., Chen, X. S., An, L. J., Funari, S. S. & Jiang, S. C. Confined lamella formation in crystalline-crystalline poly(ethylene oxide)-b-poly(ε-caprolactone) diblock copolymers. *Chinese J. Polym. Sci. (English Ed.)* **31,** 1260–1270 (2013).

47. Kato, R., Nakagawa, S., Marubayashi, H. & Nojima, S. Isothermal crystallization kinetics of poly(ε-caprolactone) blocks confined in cylindrical microdomain structures as a function of confinement size and molecular weight. *Macromolecules* **49,** 5955–5962 (2016).

48. Cheng, S. Z. D. *et al.* Isothermal thickening and thinning processes in low molecular weight poly(ethylene oxide) fractions crystallized from the melt: 2. Crystals involving more than one

fold. *Polymer (Guildf).* **33,** 1140–1149 (1992).

49. Helminen, A., Korhonen, H. & Seppala, J. V. Biodegradable crosslinked polymers based on triethoxysilane terminated polylactide oligomers. *Polymer (Guildf).* **42,** 3345–3353 (2001).

50. Zhao, X. Y., Sun, L., Wang, M. Z., Sun, Z. Y. & Xie, J. Review of crosslinked and non-crosslinked copolyesters for tissue engineering and drug delivery. *Polym. Int.* **63,** 393–401 (2014).

51. Fonseca, L. P., Trinca, R. B. & Felisberti, M. I. Thermo-responsive polyurethane hydrogels based on poly(ethylene glycol) and poly(caprolactone): Physico-chemical and mechanical properties. *J. Appl. Polym. Sci.* **133,** 43573 (2016).

52. Hilborn, J. In vivo injectable gels for tissue repair. *Nanomed. and Nanobiotech.* **3,** 589–606 (2011).

53. Abraham, G. A., Marcos-Fernández, A. & San Román, J. Bioresorbable poly(ester-ether urethane)s from L-lysine diisocyanate and triblock copolymers with different hydrophilic character. *J. Biomed. Mater. Res. - Part A* **76,** 729–736 (2006).

54. Billiet, T., Vandenhaute, M., Schelfhout, J., Van Vlierberghe, S. & Dubruel, P. A review of trends and limitations in hydrogel-rapid prototyping for tissue engineering. *Biomaterials* **33,** 6020–6041 (2012).

55. Melchels, F. P. W., Dhert, W. J. a., Hutmacher, D. W. & Malda, J. Development and characterization of a new bioink for additive tissue manufacturing. *J. Mater. Chem. B* **2,** 2282–2289 (2014).

56. Khodaverdi, E. *et al.* Biodegradable in situ gel-forming controlled drug delivery system based on thermosensitive poly(ε-caprolactone)-poly(ethylene glycol)-poly(ε-caprolactone) hydrogel. *ISRN Pharm.* **2012,** 976879 (2012).

57. Gong, C. Y. *et al.* Biodegradable in situ gel-forming controlled drug delivery system based on thermosensitive PCL-PEG-PCL hydrogel: Part 1 - Synthesis, characterization and acute toxicity evaluation. *J. Pharm. Sci.* **98,** 4684–4694 (2009).

58. Fu, S. *et al.* Injectable biodegradable thermosensitive hydrogel composite for orthopedic tissue engineering . 1 . Preparation and characterization of nanohydroxyapatite / poly(ethylene glycol) - poly(ε -caprolactone) - Poly(ethylene glycol) hydrogel nanocomposite. *J. Phys. Chem. B* **113,** 16518–16525 (2009).

59. Zhang, Y., Wang, M., Ye, J. & Lang, M. Pendant groups fine-tuning thermal gelation of poly(ε

-caprolactone)-b -poly(ethylene glycol)- b -poly(ε-caprolactone) aqueous solution. *J. Polym. Sci. Part A Polym. Chem.* **54,** 2571–2581 (2016).

60. Brinker, C. F. & Scherer, G. W. Sol-gel science: The physics and chemsitry of sol-gel processing. (1990).

61. Myers, D. & Myers, D. *Surfaces, interfaces, and colloids*. *Books - Mater.* **4,** (1999).

62. Kumar, A. *et al.* Sol-Gel Derived Nanomaterials and It ' s Applications : A Review. *Res. J. Chem. Sci.* **5,** 98–105 (2015).

63. Zarzycki, J. Past and present of sol-gel science and technology. *J. Sol-Gel Sci. Technol.* **8,** 17 (1997).

64. Henstock, J. R., Canham, L. T. & Anderson, S. I. Silicon: The evolution of its use in biomaterials. *Acta Biomater.* **11,** 17–26 (2015).

65. Fernandes, M. *et al.* Highly photostable luminescent poly(ε-caprolactone)siloxane biohybrids doped with europium complexes. *Chem. Mater.* **19,** 3892–3901 (2007).

66. Cai, L., Foster, C. J., Liu, X. & Wang, S. Enhanced bone cell functions on poly(ε-caprolactone) triacrylate networks grafted with polyhedral oligomeric silsesquioxane nanocages. *Polymer (Guildf).* **55,** 3836–3845 (2014).

67. Apeloig,Y., Karni, M. *The chemistry of organic silicon compounds*. (John Wiley & sons, 1989).

68. Barry, A. J., Daudt, W. H., Domicone, J. J. & Gilkey, J. W. Crystalline Organosilsesquioxanes. *J. Am. Chem. Soc.* **77,** 4248–4252 (1955).

69. Borovin, E., Callone, E., Ribot, F. & Diré, S. Mechanism and kinetics of oligosilsesquioxane growth in the in situ water production sol-gel route: Dependence on water availability. *Eur. J. Inorg. Chem.* 2166–2174 (2016).

70. Loy, D. A. & Shea, K. J. Bridged polysilsequioxanes : highly porous hybrid organic-inorganic materials. *Chem. Rev.* **95,** 1431–1442 (1995).

71. Brandão, L. R., Yoshida, I. V. P., Felisberti, M. I. & Gonçalves, M. do C. Preparation and characterization of cellulose acetate/polysiloxane composites. *Cellulose* **20,** 2791–2802 (2013).

72. Dirè, S., Borovin, E. & Ribot, F. Arquitecture of Silvesquioxanes. in *Handbook of Sol-Gel Science and Technology* 1–34 (2017).

73. Loy, D. A., Baugher, B. M., Baugher, C. R., Schneider, D. A. & Rahimian, K. Substituent effects on the sol-gel chemistry of organotrialkoxysilanes. *Chem. Mater.* **12,** 3624–3632 (2000).

74. Matějka, L., Dukh, O., Hlavatá, D., Meissner, B. & Brus, J. Cyclization and self-organization in polymerization of trialkoxysilanes. *Macromolecules* **34,** 6904–6914 (2001).

75. Mackenzie, J. D. Hybrid organic-inorganic materials. in *Hybrid Organic-Inorganic Composites* **4756,** 226–236 (1995).

76. Tsuru, K., Hayakawa, S. & Osaka, A. Medical applications of hybrid materials. in *Hybrid Materials. Synthesis, Characterization, and Applications* 301–337 (2007).

77. Kickelbick, G. Introduction to hybrid materials. in *Hybrid Materials. Synthesis, Characterization, and Applications* 1–48 (2007).

78. Wu, J., Hou, S., Ren, D. & Mather, P. T. Antimicrobial properties of nanostructured hydrogel webs containing silver. *Biomacromolecules* **10,** 2686–2693 (2009).

79. Ni, Y. & Zheng, S. Melting and Crystallization Behavior of Polyhedral Oligomeric silsesquioxane-capped Poly(ε-caprolactone). *J. Polym. Sci. Part B Polym. Phys.* **45,** 2201–2214 (2007).

80. Knight, P. T., Lee, K. M., Qin, H. & Mather, P. T. Polyhedral oligosilsesquioxane. *Biomacromolecules* **9,** 2458–2467 (2008).

81. Guo, Q., Knight, P. T. & Mather, P. T. Tailored drug release from biodegradable stent coatings based on hybrid polyurethanes. *J. Control. Release* **137,** 224–233 (2009).

82. Guo, Q., Knight, P. T., Wu, J. & Mather, P. T. Blends of paclitaxel with POSS-based biodegradable polyurethanes: Morphology, miscibility, and specific interactions. *Macromolecules* **43,** 4991–4999 (2010).

83. Williams, D. B. & Carter, C. B. *Transmission Electron Microscopy - A textbook for Materials Science*. **506,** (Springer, 2011).

84. Goodhew, P. J., Humphreys, J. & Beanland, R. *Electron Microscopy and Analysis*. (Taylor & Francis, 2001).

85. Bell, D.C., Erdman, N. *Low voltage electron microscopy: principles and applications*. (John Wiley & sons, 2013).

86. Radiation damage of organic materials in the transmission electron microscope (a personal

view derived from experience with synthetic polymers. *Ultramicroscopy* **12,** 279–280 (1984).

87. Egerton, R. F. *Electron Energy-Loss Spectroscopy in the Electron Microscope*. **72,** (Springer, 2011).

88. Schnablegger, H., Singh, Y. The SAXS Guide - Getting acquainted with the principles. (Anton Paar, 2013).

89. http://hyperphysics.phy-astr.gsu.edu/hbase/Particles/synchrotron.html.

90. Glatter, O. & Kratky, O. *Small Angle X-ray Scattering*. (Acta Materialia Inc., 1982).

91. Bras, W. *et al.* Recent experiments on a combined small- angle / wide-angle X-ray scattering beam line at the ESRF. *J. Appl. Crystallogr.* **36,** 791–794 (2003).

92. Plivelic, T. S., Cassu, S. N., Gonçalves, M. D. C. & Torriani, I. L. Experiências simultâneas de espalhamento de raios X e calorimetria diferencial de varredura (SAXS/WAXD/DSC) com resolução temporal utilizando radiação síncrotron. *Polímeros* **15,** 199–206 (2005).

93. Ryan, A. J., Stanford, J. L., Bras, W. & Nye, T. M. W. A synchrotron X-ray study of melting and recrystallization in isotactic polypropylene. *Polymer (Guildf).* **38,** 759–768 (1997).

94. Feigin & Svergun, D. I. Structure Analysis by Small-Angle X-Ray and Neutron Scattering. *Acta Polymerica* **40,** 224–224 (1989).

95. Dahmouche, K., Santilli, C. V., Pulcinelli, S. H. & Craievich, A. F. Small-angle X-ray scattering study of sol-gel-derived siloxane-PEG and siloxane-PPG hybrid materials. *J. Phys. Chem. B* **103,** 4937–4942 (1999).

96. Judeinstein, P., Titman, J., Stamm, M. & Schmidt, H. Investigation of ion-conducting ormolytes : Structure-property relationships. *Chem. Mater.* 127–134 (1994).

97. Mullin, J. W. *Crystallization*. (Butterworth Heinemann, 2001).

98. Rabiej, S. & Rabiej, M. Determination of the parameters of lamellar structure of semicrystalline polymers using a computer program SAXSDAT. *Polimery* **56,** 662–670 (2011).

99. Roe, R. J. *Methods of X-ray and neutron scattering in polymer science*. *Topics in Polymer Science* **3,** (2000).

100. Guinier, A., Fournet, G., Walker, C. B. & Vineyard, G. H. *Small-Angle Scattering of X-Rays*. *Phys. Today* **9,** 38–39 (1956).

101. Strobl, G. R. & Schneider, M. Direct evaluation of the electron density correlation function of

partially crystalline polymers. *J. Polym. Sci. Polym. Phys.* **18,** 1343–1359 (1980).

102. Goderis, B., Reynaers, H., Koch, M. H. J. & Mathot, V. B. F. Use of SAXS and linear correlation functions for the determination of the crystallinity and morphology of semi-crystalline polymers: Application to linear polyethylene. *Polymer (Guildf).* **1,** 1715–1738 (1999).

103. Thuresson, A., Segad, M., Plivelic, T. S. & Skepö, M. Flocculated laponite-PEG/PEO dispersions with multivalent salt: A SAXS, cryo-TEM, and computer simulation study. *J. Phys. Chem. C* **121,** 7387–7396 (2017).

104. Sperling, L. H. *Introduction to physical polymer science*. (Wiley, 1992).

105. Palacios, J. K. *et al.* Sequential crystallization and morphology of triple crystalline biodegradable PEO-b-PCL-b-PLLA triblock terpolymers. *RSC Adv.* **6,** 4739–4750 (2016).

106. Alp, B. & Cesur, S. Isothermal crystallization kinetics and mechanical properties of polycaprolactone composites with zinc oxide, oleic acid, and glycerol monooleate. *J. Appl. Polym. Sci.* **130,** 1259–1275 (2013).

107. La, Y. H. *et al.* Enhancing water permeability of fouling-resistant POSS-PEGM hydrogels using 'addition-extraction' of sacrificial additives. *J. Memb. Sci.* **401–402,** 306–312 (2012).

108. http://www.esrf.eu/computing/scientific/FIT2D/.

109. http://www.lnls.cnpem.br/grupos/saxs1/.

110. Dyadkin, V., Pattison, P., Dmitriev, V. & Chernyshov, D. A new multipurpose diffractometer PILATUS@SNBL. *J. Synchrotron Radiat.* **23,** 825–829 (2016).

111. Silva, L. C. E., Germiniani, L. G. L., Plivelic, S. & Gonçalves, M. C. Solvent-free and biocompatible multiphased organic-inorganic hybrid nanocomposites. *Soft Matter* **14,** 1709–1718 (2018).

112. Orel, B., Ješe, R., Vilčnik, A. & Štangar, U. L. Hydrolysis and solvolysis of methyltriethoxysilane catalyzed with HCl or trifluoroacetic acid: IR spectroscopic and surface energy studies. *J. Sol-Gel Sci. Technol.* **34,** 251–265 (2005).

113. Park, E. S., Ro, H. W., Nguyen, C. V, Jaffe, R. L. & Yoon, D. Y. Infrared spectroscopy study of microstructures of poly(silsesquioxane)s. *Chem. Mater.* **20,** 1548–1554 (2008).

114. Loy, D. A. Sol–gel processing of hybrid organic–inorganic materials based on polysilsesquioxanes. in *Hybrid Materials: Synthesis, Characterization, and Applications* 225–

254 (2007).

115. Salon, M. C. B., Bayle, P.-A., Abdelmouleh, M., Boufi, S. & Belgacem, M. N. Kinetics of hydrolysis and self condensation reactions of silanes by NMR spectroscopy. *Colloids Surfaces A Physicochem. Eng. Asp.* **312,** 83–91 (2008).

116. da Silva, L. C. E., Bertran, C. A. & Gonçalves, M. C. Water vapor-induced formation of poly(ε-caprolactone) membranes for guided bone regeneration. *J. Mater. Sci.* **50,** 4122–4131 (2015).

117. Mei-Hui Tsai & Wha-Tzong Whang. Low dielectric polyimide/poly(silsesquioxane)-like nanocomposite material. *Polymer (Guildf).* **42,** 4197–4207 (2001).

118. Magonov, S. N., Elings, V. & Whangbo, M.-H. Phase imaging and stiffness in tapping-mode atomic force microscopy. *Surf. Sci.* **375,** L385–L391 (1997).

119. Kimoto, K., Sekiguchi, T. & Aoyama, T. Chemical shift mapping of Si L and K edges using spatially resolved EELS and energy-filtering TEM. *J. Electron Microsc. (Tokyo).* **46,** 369–374 (1997).

120. Paoli, M. De. *Degradação e Estabilização de Polímeros*. (Chemkeys, 2008).

121. Li, G. Z., Wang, L., Toghiani, H., Daulton, T. L. & Jr, C. U. P. Viscoelastic and mechanical properties of vinyl ester (VE)/ multifunctional polyhedral oligomeric silsesquioxane (POSS) nanocomposites and multifunctional POSS - styrene copolymers. *Polymer (Guildf).* **43,** 4167–4176 (2002).

122. Laine, R. M. Nanobuilding blocks based on the [$OSiO_{1.5}$]x (x= 6, 8, 10) octasilsesquioxanes. *J. Mater. Chem.* **15,** 3725 (2005).

123. Saika-Voivod, I., King, H. M., Tartaglia, P., Sciortino, F. & Zaccarelli, E. Silica through the eyes of colloidal models—when glass is a gel. *J. Phys. Condens. Matter* **23,** 285101 (2011).

124. https://octave.sourceforge.io/octave/function/fminunc.html.

125. Bourgeat-lami, E. Hybrid organic/inorganic particles. in *Hybrid Materials. Sythesis, Characterization, and Applications* 87–149 (2007).

126. Chiavacci, L. A. *et al.* Effect of presence of an acid catalyst on structure and properties of iron-doped siloxane-polyoxyethylene nanocomposites prepared by sol - Gel. *J. Non. Cryst. Solids* **345–346,** 585–590 (2004).

127. He, C., Sun, J., Ma, J., Chen, X. & Jing, X. Composition dependence of the crystallization

behavior and morphology of the poly(ethylene oxide)-poly(ε-caprolactone) diblock copolymer. *Biomacromolecules* **7,** 3482–3489 (2006).

128. Castillo, R. V. & Müller, A. J. Crystallization and morphology of biodegradable or biostable single and double crystalline block copolymers. *Prog. Polym. Sci.* **34,** 516–560 (2009).

129. Bittiger, H., Marchessault, R. H. & Niegisch, W. D. Crystal structure of poly(ε-caprolactone). *Acta Crystallogr. B* **26,** 1923–1927 (1970).

130. Jiang, S., He, C., An, L., Chen, X. & Jiang, B. Crystallization and ring-banded spherulite morphology of poly(ethylene oxide)-block-poly(ε-caprolactone) diblock copolymer. *Macromol. Chem. Phys.* **205,** 2229–2234 (2004).

131. Svoboda, P., Svobodova, D., Chiba, T. & Inoue, T. Competition of phase dissolution and crystallization in poly(ε-caprolactone)/poly(styrene-co-acrylonitrile) blend. *Eur. Polym. J.* **44,** 329–341 (2008).

132. Ma, Y., Zha, L., Hu, W., Reiter, G. & Han, C. C. Crystal nucleation enhanced at the diffuse interface of immiscible polymer blends. *Phys. Rev. E - Stat. Nonlinear, Soft Matter Phys.* **77,** 1–5 (2008).